

**INFLUENCE OF NANO-STRUCTURED CHEMICALS ON THE
MICROSTRUCTURES AND MECHANICAL RELIABILITY OF
LEAD-FREE TIN-BASED SOLDERS**

BY

DEEP CHOUDHURI

A DISSERTATION

**Submitted to
Michigan State University
In the partial fulfillment of the requirements
for the degree of**

DOCTOR OF PHILOSOPHY

Materials Science and Engineering

2009

ABSTRACT

INFLUENCE OF NANO-STRUCTURED CHEMICALS ON THE MICROSTRUCTURES AND MECHANICAL RELIABILITY OF PB-FREE SN-BASED SOLDERS

BY

DEEP CHOUDHURI

Nanostructured chemicals utilized in this study are polyhedral oligomeric silsesquioxanes (POSS) trisilanol. The crucial chemical entity of POSS trisilanols are the silanol (Si-OH) groups, which can form thermodynamically feasible bonds with metals (e.g Sn, Cu). This study capitalizes on such bonding ability of POSS trisilanols by incorporating them in Pb-free Sn-based solder alloys (e.g. eutectic Sn-Ag, near eutectic Sn-Ag-Cu). These solder alloys are used for fabricating solder joints used in microelectronic interconnects. During service solder joints are subjected to thermal excursions due to which they experience thermomechanical fatigue (TMF). As a result, mechanical reliability of solder joints undergoes deterioration. This study investigated the influence of POSS trisilanol addition on the mechanical reliability of Pb-free Sn-based single shear-lap solder joints subjected to TMF between -55°C to 125°C. Effect of TMF was evaluated through observation of surface damage evolution and measurement of residual mechanical shear strength as a function of number of TMF cycles. It was found that POSS trisilanol addition improved the mechanical reliability of Pb-free Sn-based solder joints by enhancing interfacial bonding, and the ability of the solder matrix to accommodate strains generated during TMF. To further evaluate the influence of nanostructured chemical addition separate set of

studies were performed on POSS trisilanol containing bulk and single shear-lap solder joint specimens. Effect of POSS trisilanol on bulk specimens were investigated through observation of as-solidified microstructure and thermal analysis. On the other hand studies involving single shear-lap solder joints were conducted by isothermally aging them at different temperatures. Results from the studies on bulk and joint specimens indicate that POSS trisilanols are present at the Sn-Sn grain boundaries and between interfacial regions of different phases.

Acknowledgements

First of all I would like to express my sincere gratitude to my advisor Dr. Andre Lee for providing intellectual guidance and helping me to see the broader picture in research and life in general. I am extremely grateful to my co-advisor Dr. K.N. Subramanian for providing insightful suggests during the course of PhD work. I have gained a lot from my discussions with him, individually and during group meetings (which I occasionally missed). I would also especially like to thank Dr. Chen En Ho for mentoring me in experimental and metallographic techniques.

I also want to convey my appreciation to my committee member Dr Melissa Baumann and Dr Timothy Hogan for very insightful and constructive criticisms.

I would like to thank my friends Devesh, Tithi, Shishir, Ke-bin Low, Ajay, DeepB, Madhusudhan, Madhu, Surabhi, Raylene, Shahana, Sumit, Sachin, Naveen, Sutti, Varun, Kashi, Kavita, Bhushan, Shreya , and many more for helping both academically and philosophically. Life here at MSU would have been dull without them. Finally, I would like to Ma and Baba, and family members Mithu didi ,Babuda, and Boromama for their steady advice and support during my journey.

Table of contents

List of Tables	viii
List of Figures	x
Chapter 1 Introduction	1
1.1 Sn-based Pb-free solders.....	1
1.2. Influences of service conditions on Sn-based solder joints.....	3
1.2.1 Influence of high Sn content and intermetallic compound phases on the service reliability of Sn-based alloys	4
1.2.2 Influence of service parameters on the reliability of solder joints	8
1.3 Development of Pb-free Sn-based solders	12
1.3.1 Alloying approach	13
1.3.2 Composite approach.....	16
1.3.3 Development of nano-composite solders using nano-structured chemicals.....	19
1.4 Research strategy	24
Chapter 2 Experimental Procedure and methods	26
2.1 Materials and processing.....	26
2.2 Preparation of Solder Joints	27
2.3 Preparation of bulk alloy specimen.....	27
2.4 Procedure for polishing joint and bulk specimens.....	32
2.5 Setup for TMF experiments.....	33
2.6 Mechanical and microstructural characterization.....	36
Chapter 3 Effect of temperature regimes on the thermomechanical fatigue behavior of eutectic Sn-Ag joints	39
3.1. Background	40
3.2. Experimental details	42
3.3 Results and discussion.....	43
3.3.1 Microstructural Evaluation of Damages resulting from Low Temperature Regime TMF	43
3.3.2 Effect of temperature regime of TMF on surface damage accumulation	52
3.3.3 Influence of temperature regime of TMF on the residual mechanical properties.....	57
3.4 Conclusions.....	61

Chapter 4 Low temperature regime thermomechanical fatigue behavior of nano-structured polyhedral oligomeric silsesquioxanes reinforced Sn-based solder joints	63
4.1. Background	64
4.2. Experimental details	65
4.3 Results and discussion	67
4.3.1 Influence of POSS reinforcements on the residual mechanical behavior of Sn-based solder joints	67
4.3.2 Microstructural features contributing to the low temperature behavior of POSS reinforced solder joints	73
4.4. Conclusions	86
Chapter 5 Influence of polyhedral oligomeric silsesquioxane additions on Sn-Ag-Cu bulk specimens	87
5.1. Background	88
5.2. Experimental details	90
5.3. Results and discussions	95
5.3.2 Influence of POSS additions on the microstructure of Sn-3.0wt%Ag-0.5wt%Cu	95
6.3.3 Thermal analysis	109
5.4. Summary	113
Chapter 6 Influence of polyhedral oligomeric silsesquioxane additives on the coarsening kinetics of Ag₃Sn intermetallic compound in Sn-Ag-Cu solder joints	119
6.1. Background	120
6.2. Experimental details	122
6.3 Results and discussion	123
6.3.1 Coarsening theories	123
6.3.2 Influence of POSS addition on Ag ₃ Sn particle size evolution	127
6.3.3 Growth kinetics	138
6.4 Conclusions	140
Chapter 7 Summary and recommendations	150
7.1 Summary	150
7.2 Recommendations	151

Appendix A Influence of polyhedral oligomeric silsesquioxanes trisilanol chemistry on the low temperature regime thermomechanical fatigue behavior of nanocomposite Sn-based solder joints154

A1 Experimental details.....	156
A2 Results and discussion	156
A2.1 Effect of phenyl trisilanol POSS on the residual mechanical behavior of Sn-based solder joints	157
A2.2. Influence of phenyl trisilanol POSS reinforcements on microstructural damages	163
A3. Conclusions	170

Appendix B Strain assisted allotropic transformation of β -Sn172

B1. Introduction	173
B2. Experimental details.....	175
B2.1 Mechanical Pre-Straining.....	175
B2.2 Characterization and measurements.....	175
B3. Results and discussion	176
B3.1 Effect of mechanical pre-straining on the allotropic transformation of β -Sn	176
B3.2 Microstructural and mechanical characterization.....	181
B3.3 Effect of stress on the growth kinetics of α -Sn.....	188
B4. Summary.....	193

References.....194

List of Tables

Table 1.1 Listing of single crystal elastic modulus “E” and CTE “ α ” of Sn as a function of five different crystallographic orientations. [25].....	6
Table 1.2 Bond energy values at 25° C [61].	22
Table 4.1 Statistical analysis of residual mechanical behavior of SA, and SA2iB solder joints (Figure 4.3.1 (a)). Single tail t-test is used for this purpose. Analysis is carried out on the basis of p values. This is evaluated by comparing residual mechanical strength data of two chosen cycles. If there is a difference in the residual strength at the chosen number of cycles, then the p value is less than 0.05, otherwise the two chosen data sets are not statistically different. In this analysis, residual strength data for 100 cycles is compared with 400 and 500 cycles.....	71
Table 4.2 Statistical analysis of residual mechanical behavior of SAC305, and SAC2iB solder joints (Figure 4.3.1). Methodology for analysis is exactly the same as described in Tables 4.1. In this analysis, residual strength data after 100 cycles is compared with 400 and 500 cycles for both the types of specimens and additional 1000 cycles for SAC2iB..	72
Table 5.3.1 $\lambda \Delta T$ values for all specimens	99
Table 5.3.2 Effects of trisilanol POSS additions on the heat of fusion of SAC305	110
Table 5.3.3 R^2 from linear least square fit and activation energy of melting resulting from Kissinger’s analysis (Figure 5.3.10 (b))	112
Table 6.1 list of activation energies of diffusion of Ag and Cu along “a” and “c” axes of Sn.....	121
Table 6.2 Summary of mechanisms controlling coarsening of secondary phase particles and the respective phase size exponents.....	126

Table 6.3 Statistical analysis for determining phase size constant “n” in $\langle D \rangle^n - \langle D_0 \rangle^n = Kt$ through non-linear regression.....142

Table 6.4 Linear regression analysis to determine “K” in $\langle D \rangle^n - \langle D_0 \rangle^n = Kt$ for the data presented in Figures 7146

Table 6.5 Influence of POSS trisilanols on the activation energies of diffusion 149

Table AI Comparison of single tail p-values obtained from t-test. Here residual strength data after 1 and 100 cycles are compared with 100, 400, and 500 cycles for SA2phe and 100, 400, and 1000 cycles for SAC2phe. P-values <0.05 would indicate that the compared data sets are statistically different.....162

Table BI Hardness values of β -Sn at different locations and distances from the β/α Sn interface.....186

Table BII Values showing the growth rate for a given strain state of the specimens and the corresponding correlation coefficients for linear least square fits.....192

List of Figures

- Figure 1.2.1** Schematic showing the body-centered-tetragonal crystal structure of Sn.6
- Figure 1.2.2** Schematic showing (a) different service parameters present during thermal excursions, and (b) High and low temperature regimes experienced during thermal excursions. Adapted from Subramanian [18].11
- Figure 1.3.1** Schematic showing two different types POSS anatomies (a) Trisilanol POSS with three Si-OH groups, (b) Octa POSS without any Si-OH groups.21
- Figure 1.3.2** SEM images showing microstructural damages after 1000 cycles of TMF in (a) eutectic Sn-3.5wt%Ag (adapted from Lee et.al. [21]), and (b) eutectic Sn-3.5wt%Ag reinforced with 2wt% (10 vol%) POSS with Si-OH groups (adapted from Lee et.al. [55]).22
- Figure 2.2.1** Apparatus used for fabricating solder joints (a) aluminum fixture used for positioning the half dog bone copper strips, (b) schematic of a solder joint with dimensions shown. (Adapted from J G Lee thesis [1]).29
- Figure 2.2.1 (c)** Temperature profile used for fabricating solder joints . (Adapted from J G Lee thesis [1]).30
- Figure 2.3.1** Schematic showing the experimental set-up used for the preparation of bulk specimens.31
- Figure 2.4.1** Schematic showing the jig used for holding solder joints during polishing. The wider ends of the joint are backed up with Cu strips of similar thickness as that of the half dog-bone pieces. This prevents bending or twisting of the joint (at the center) during polishing.31
- Figure 2.5.1** Image showing the environmental chamber used for conducting TMF experiments34
- Figure 2.5.2** Image showing the custom built stage used for placing solder specimens inside the environmental chamber.34
- Figure 2.5.3** Temperature profiles used for thermally cycling the solder joints...35
- Figure 2.6.1** Set-up used for mechanical characterization (a) RSA III used, and (b) location of the solder joint inside the specimen holder of RSA III .38

- Figure 3.3.1** Schematic of the regions on the solder joint observed for microstructural evolution. Region-1 is at the center, region-2 is ~100µm below region-1 and region-3 is at the IMC / Solder interface.45
- Figure 3.3.2** SEM images of region 1 showing the evolution of surface damage within the solder and near the IMC layer and at the Cu₆Sn₅ IMC / solder interface after (a) 0, (b) 50, (c) 100, (d) 200, (e) 300, (f) 400, (g) 500 cycles of TMF. Scale bar indicates 50µm.48
- Figure 3.3.3** SEM images of region 2 showing the evolution of surface damage near the Cu₆Sn₅ IMC layer and at the Cu₆Sn₅ IMC /solder interface after (a) 0, (b) 50, (c) 100, (d) 200, (e) 300, (f) 400, (g) 500 cycles of TMF. Scale bar indicates 50µm.49
- Figure 3.3.4** SEM images of region 3 showing the evolution of surface damage at the IMC/solder interface after (a) 0, (b) 50, (c) 100, (d) 200, (e) 300, (f) 400, (g) 500 cycles of TMF.....50
- Figure 3.3.5** High magnification images showing debonding at the Cu₆Sn₅ IMC layer / solder interface at two different regions after 500 cycles (a) Location near region 1 and (b) is the corresponding BE image. SEM image of region 3 is shown in (c) and its corresponding BE image in (d).51
- Figure 3.3.6** SEM images showing surface damage on Sn-3.5wt%Ag Solder joints after 1000 cycles of high temperature regime TMF with long dwell at (a) high temperature extreme, and (b) low temperature extreme. Adopted from Subramanian et.al. [21, 42].....55
- Figure 3.3.7** SEM images showing the effect of high temperature regime TMF on surface damage features near the IMC layer / solder interface, (a) Sn-Sn grain decohesion and (b) grain boundary sliding / relief and shear banding. Adopted from Choi et.al.[19].....56
- Figure 3.3.8** Plot showing the variation of residual shear stress of Sn-3.5wt%Ag solder joints as a function of TMF cycles. Error bars represent 95% confidence intervals.58
- Figure 3.3.9** (a) Cross sectional view of a mechanically failed Sn-3.5wt%Ag solder joint;(b) Enlarged view on the of the region inside the dotted rectangle in (a). This joint had undergone 500 cycles of TMF prior to mechanical testing.59
- Figure 3.3.10** Plot comparing the effect of high and low temperature regime TMF on average shear strength of Sn-3.5wt%Ag single shear-lap solder joints after 500 cycles of TMF. Residual strength data used for comparison was obtained from [18, 21, 42].60

- Figure 4.3.1 (a)** Comparison of residual shear strengths of (a) SA and SA2iB solder joints. Error bars show 95% confidence intervals. Second order exponential non-linear least square fits have also been shown69
- Figure 4.3.1 (b)** Comparison of residual shear strengths of SAC305 and SAC2iB solder joints. Error bars show 95% confidence intervals. Second order exponential non-linear least square fits have also been shown.....70
- Figure 4.3.2** SEM images showing surface damage evolution in eutectic Sn-3.5Ag (SA) solder joint due to low temperature regime TMF between -55°C to 125°C. Surface damages after 100 cycles of TMF has been indicated with arrows.74
- Figure 4.3.3** SEM images showing surface damage evolution in SA + 2wt% Iso-Butyl trisilanol (SA2iB) solder joint due to low temperature regime TMF between -55°C to 125°C. Surface damages after 100 cycles of TMF has been indicate with arrows.....75
- Figure 4.3.4** SEM images showing surface damage evolution in Sn-3.0wt%Ag-0.5wt%Cu (SAC305) solder joint due to low temperature regime TMF between -55°C to 125°C. Surface damages after 100 cycles of TMF has been indicate with arrows.76
- Figure 4.3.5** SEM images showing surface damage evolution in SAC305+2wt% Iso-Butyl trisilanol (SAC2iB) solder joint due to low temperature regime TMF between -55°C to 125°C. Surface damages after 100 cycles of TMF has been indicate with arrows.77
- Figure 4.3.6** High magnification SEM images comparing the effects of low temperature regime TMF on surfaces damages within the solder region after 500 cycles. Nano-composite (SA2iB and SAC2iB) solder joints show significant damages within the solder region as compared to Sn-based solder (SA and SAC305) joints.80
- Figure 4.3.7** High magnification SEM images comparing the effects of low temperature regime TMF on the Cu_6Sn_5 layer – solder interfacial regions in Sn-based and nano-composite solder joints. Cu_6Sn_5 layer –solder decohesion is evident in both SA and SAC305, while damage is primarily located within the solder region in SA2iB and SAC2iB. Scale bar indicates 10 μm83
- Figure 4.3.8** High magnification SEM images comparing Cu_6Sn_5 particle – solder interfaces in SA and nano-composite SA2iB after 500 cycles of low temperature regime TMF. Interfacial decohesion is evident in SA while shear bands within the solder matrix near the Cu_6Sn_5 – solder interface is observed in SA2iB.84

Figure 4.3.9 BE image of SAC2iB showing shear bands within the solder region near the Cu_6Sn_5 – solder interface.....	85
Figure 5.2.1 Schematic showing two different types POSS anatomies (a) Iso-Butyl Trisilanol POSS with three Si-OH groups, (b) Iso-Butyl Octa POSS without any Si-OH groups. Chemical formula for organic Iso-Butyl(R) group has also been shown.	92
Figure 5.2.2 Comparison of cooling rates utilized for solidifying molten bulk solder specimens. Solid line indicates the faster cooling rate at $53^\circ\text{C}/\text{min}$, while the dashed line indicates slower cooling at a rate of $16^\circ\text{C}/\text{min}$	93
Figure 5.2.3 Left hand side showing the 3D views of the “button” shaped as-solidified bulk specimens. The right hand side shows the regions observed for microstructural characterization. The square boxes at the center of each view i.e. planar and cross-sectional, are the locations from where images for analysis were acquired.....	94
Figure 5.3.1 Optical micrographs showing the effects of 2wt% trisilanol POSS and Octa POSS additions on the as-solidified microstructures of SAC305. All the specimens have been cooled at $53^\circ\text{C}/\text{sec}$	100
Figure 5.3.2 Plot showing the quantitative microstructural analysis of the secondary dendrite arm spacing.	101
Figures 5.3.3 Optical micrographs of showing the effects of 2wt% Trisilanol POSS additions to SAC305 specimens cooled at (a)-(b) $16^\circ\text{C}/\text{sec}$ (slower cooling rate), and (c)-(d) $53^\circ\text{C}/\text{sec}$ (faster cooling rate).	102
Figure 5.3.4 Schematic showing the dendritic morphologies of (a) SAC, and (b) after trisilanol POSS additions.	103
Figure 5.3.5 (a) Plots showing measured cooling curves of SAC305, SAC305 + 2wt% Iso-Butyl trisilanol POSS, and SAC305 + 2wt% Iso-Butyl Octa POSS.....	104
Figure 5.3.5 (a) Plots showing effects of trisilanol POSS and Octa POSS additions on undercooling. All the specimens were cooled at $53^\circ\text{C}/\text{sec}$	105
Figure 5.3.6 High magnification BEI showing sizes and morphology of Cu_6Sn_5 and Ag_3Sn IMCs in the ternary eutectic regions in (a) SAC305, and (b) SAC305 + 2wt% Iso-Butyl trisilanol POSS s.....	1087

Figure 5.3.7 (a) Initial as-solidified microstructure of SAC305 + 2wt% Iso-Butyl trisilanol bulk specimen, (b) microstructure of the same specimen after isothermally aging at 100°C for 5 months. 108

Figure 5.3.8 Typical DSC thermogram observed during melting. Area within the peak (minima) provides the heat of fusion. The negative y-axis represents endothermic heat input..... 114

Figure 5.3.9 Typical DSC thermograms showing the increase in peak temperature T_p with increase in heating rate during melting. The negative y-axis represents endothermic heat input..... 115

Figure 5.3.10 (a) Plots showing the effects of 2wt% trisilanol POSS additions on peak temperature vs. heating rate. Slopes in (a) were obtained by fitting a straight line. 116

Figure 5.3.10 (b) Plots showing the effects of 2wt% trisilanol POSS additions on Arrhenius plot for melting. 117

Figure 5.3.11 BEI comparing microstructures of (a) SAC305 and (b) SAC305 + 2wt% iso-Buty trisilanol POSS. POSS containing specimen show considerably more Sn grain boundaries than SAC305. Furthermore, size of Sn grains in (b) is less than 20 μ m. 118

Figure 6.3.1 Backscattered electron images (BEI) showing the initial microstructures of (a) Sn-3.0wt%Ag-0.5%Cu (SAC305), and (b) SAC305 + 2wt% Iso-Butyl trisilanol POSS (SAC2iB). Different microconstituents within the microstructure have been indicated. High magnification SEM images showing the size and morphology of Ag₃Sn IMC particles in (c) SAC305, and (d) SAC2iB. 129

Figure 6.3.2 Distribution of Ag₃Sn particle sizes in SAC305 and SAC2iB specimens. Two-tailed p value equals 0.54, suggesting that there is no statistical difference between the Ag₃Sn particle diameters in SAC305 and SAC2iB specimens. This analysis was carried out using six specimens for each type of solder joint. 130

Figure 6.3.3 BEI showing the influence of isothermal aging at 107°C, 150°C, and 180°C on (a)-(c) SAC305 and (d)-(f) SAC2iB specimens. 131

Figure 6.3.4 (a) $\langle D \rangle$ v.s. t plots comparing Ag₃Sn particle sizes in SAC305 and SAC2iB specimens isothermally aged at 80°C. 132

Figure 6.3.4 (b) $\langle D \rangle$ v.s. t plots comparing Ag₃Sn particle sizes in SAC305 and SAC2iB specimens isothermally aged at 90°C. 133

Figure 6.3.4 (c) $\langle D \rangle$ v.s. t plots comparing Ag₃Sn particle sizes in SAC305 and SAC2iB specimens isothermally aged at 107°C. 134

Figure 6.3.4 (d) $\langle D \rangle$ v.s. t plots comparing Ag_3Sn particle sizes in SAC305 and SAC2iB specimens isothermally aged at 120°C.	135
Figure 6.3.4 (e) $\langle D \rangle$ v.s. t plots comparing Ag_3Sn particle sizes in SAC305 and SAC2iB specimens isothermally aged at 150°C.	136
Figure 6.3.4 (f) $\langle D \rangle$ v.s. t plots comparing Ag_3Sn particle sizes in SAC305 and SAC2iB specimens isothermally aged at 180°C.	137
Figure 6.3.5 (a) Plot of $\langle D \rangle^4 - \langle D_0 \rangle^4$ v.s t for determining the “K” for SAC305 specimens isothermally aged at 80°C, 90°C, and 107°C.....	143
Figure 6.3.5 (b) Plot of $\langle D \rangle^3 - \langle D_0 \rangle^3$ v.s t for determining the “K” for SAC305 specimens isothermally aged at 120°C, 150°C, and 180°C.....	144
Figure 6.3.5 (c) Plot of $\langle D \rangle^5 - \langle D_0 \rangle^5$ v.s t . for determining the “K” for SAC2iB specimens isothermally aged at 80°C, 90°C, 107°C, and 120°C.....	145
Figure 6.3.6 (b) Arrhenius plots for calculating activation energies for SAC2iB.	148
Figure A1 Schematic showing the anatomy of POSS trisilanol. Chemical formula of the organic phenyl (R) group is also shown.	159
Figure A2 (b) Plots comparing influence of pheTriPOSS on the residual mechanical behavior of SAC305.....	161
Figure A3 SEM images showing microstructural evolution in SA2phe solder joints after (a) 0, (b) 100, and (c) 500 cycles.....	165
Figure A3 SEM images showing microstructural evolution in SAC2phe solder joints after (a) 0, (b) 100, and (c) 500 cycles.....	166
Figure A5 High magnification SEM images comparing surface damage within solder region after 500 cycles of TMF in (a) SA2phe and (b) SAC2phe specimens.....	167
Figure A6 SEM images comparing the interfacial damage after 500 cycles in (a) SA2phe and (b) SAC2phe. Cu_6Sn_5 / Sn decohesion in SAC2phe have been indicated by black arrows.....	168
Figure A7 Compares microstructural evolution of the Cu_6Sn_5 layer / solder interfacial region for (a)-(b) SA2phe and (c)-(d) SAC2phe after 100 and 500 cycles. These images show phenyl trisilanol reduces the intensity of interfacial damage.	169
Figure B1 Stereo-optical images showing the location of α -Sn on the (a) tensile side of the non-uniformly bent specimen with 6% outer fiber strain, (b)	

compressive side of the uniformly bent specimen with 7.7% outer fiber strain (shown as Region-1 and Region-2).....	178
Figure B2 XRD of the α -Sn detached from the non-uniformly bent specimen..	179
Figure B3 SEM images showing the microstructural evolution of α -Sn on the non-uniformly bent specimen aged at -15°C (a) as observed after 2.1 months, (b) after 2.6 months	182
Figure B4 SEM images showing the microstructural evolution of α -Sn on the uniformly bent specimen aged at -15°C (a) after 3.5 months in Region-1 (b) after 4 months in Region-1, (c) after 3.5 months in Region-2 (d) after 4 months in Region-2.....	183
Figure B5 SEM micrographs showing the inter-granular and trans-granular cracks within α -Sn region on (a) non-uniformly bent, and (b) uniformly bent specimens.....	184
Figure B6 SEM micrographs showing surface relief features with in β -Sn region adjacent to α -Sn (a) non-uniformly bent, and (b) uniformly bent specimens.....	185
Figure B7 (a) Schematic showing the location of the indents on the broad side of the non-uniformly bent specimen (b) SEM image showing the location and size of the indents. A load of 1 Kg was applied to the broad side of the specimen for 10 seconds.	187
Figure B8 (a) Stereo-optical image showing the location of the α -Sn wart (inside the white circle) on the tensile side of the non-uniformly bent specimen used for measuring growth kinetics.....	190
Figure B8 (b) plot showing the change in measured area of the same α -Sn wart with number of days.....	190
Figure B9 Plot showing the change in the measured area of Region-1 as a function of days. Region-1 was located on the compressive side of the uniformly bent specimen.	191

Chapter 1

Introduction

1.1 Sn-based Pb-free solders

Eutectic Sn-37wt%Pb solder alloys have been used as interconnects in electronic packaging, automotive, and aircraft industries for a long time [1]. However, the presence of Pb in solders has raised serious environmental and health concerns. This has led to concerted efforts by industries all over the world to find a viable substitute for Pb [1]. It was also realized that a replacement Pb-free solder should have reasonable wetting behavior, ease of availability, and low cost [1]. Additionally, replacement solders should be able to withstand increasingly demanding service conditions, while simultaneously retaining mechanical reliability of an electronic package. This necessitated solder materials with both high strength and ductility [2-4].

On the basis of above mentioned criterion, binary Sn-based Pb-free solder alloys have been identified as possible substitutes. Among several candidates, (e.g. Sn-Ag, Sn-Cu, Sn-Sb, Sn-Zn, Sn-Bi etc.), eutectic Sn-3.5wt%Ag solder was recognized as a viable replacement through extensive research [1, 4-6]. Sn-3.5wt%Ag offered the best combination of high strength and ductility [4, 7]. Melting point of Sn-3.5wt%Ag (221°C) is higher than Sn-37wt%Pb (183°C). Consequently, Sn-3.5wt%Ag is suitable to automobile under-the-hood application, where solder joints regularly experience high service temperatures. However, mechanical behavior of Sn-3.5wt%Ag is comparable to Sn-37wt%Pb, but compares less favorably in terms of solderability. As a result, elements like Cu,

Bi, In, Zn etc. have been added to the base Sn-Ag to improve solderability and depress melting point [7]. Elemental additions were also observed to influence the mechanical behavior of the resulting Sn-based ternary alloys systems [7-10]. Cu, Bi, In and Zn additions improved the tensile strength of base Sn-Ag alloy [7-10]. However, Sn-Ag-Cu (resulting from Cu additions) exhibited comparatively better ductility and mechanical fatigue behavior. Furthermore, mechanical properties of Sn-Ag-Cu solders were found comparable to that of Sn-3.5wt%Ag [7, 9, 10]. Consequently, improved mechanical properties along with ease of availability, low cost, and good wetting behavior has made Sn-Ag-Cu a popular choice for study and application [8, 11-15].

Although majority of these studies were carried out on bulk Sn-based Pb-free solders specimens, but in real applications solders are used in joint configuration. These joints are found in surface mount devices such as small outline package, quad flat package, and ball grid array package [1]. These surface mounts involve joining integrated chip (IC) packages on a printed circuit board (PCB) [1]. Consequently, joints form not only the electrical connections, but also mechanical connection between the substrates and the components (IC package). Since Sn-based Pb-free solder alloys are mechanically softer than other components (e.g. Cu substrate, lead frames) [1], strength of soldered joints form the weakest link in terms of mechanical reliability of the electronic package. As a consequence it is necessary to design Sn-based solders that can withstand harsh service conditions without compromising their mechanical reliability. These service conditions require solder joints to experience thermal excursions

resulting in thermomechanical fatigue (TMF) of those joints. Additionally, solder joints are also subjected to external mechanical stresses during service e.g. mechanical vibrations and impact loading [1, 7, 10, 16-18].

In view of the above mentioned requirements and issues literature review presented in this chapter serves the following purpose:

1. Identify service conditions related reliability issues with Sn-based Pb-free (hence forth "Sn-based") solder joints and,
2. Present progress made in the development of Sn-based solder materials for combating reliability issues, and problems associated with such solder materials.

1.2. Influences of service conditions on Sn-based solder joints

As mentioned in the previous section, solder joints experience TMF during service. TMF occurs during thermal excursions encountered by joints in automotive under-the-hood and power cycling type applications[1, 14, 18-24]. Temperature difference arising from thermal excursions results in cyclic displacements between materials with dissimilar coefficient of thermal expansion (CTE). Such CTE mismatches arise between the constituents present within the solder joint (i.e. solder region, the interfacial intermetallic compound (IMC) layer, and the substrate)[1, 14, 18-26]. Stresses arising from such CTE mismatches result in TMF of joints. Additionally, creep / stress relaxation may also occur within solder joints during thermal excursions [3, 23, 27-30]. So the combination of stresses (generated by CTE mismatch), and creep / stress relaxation result in temperature dependant deformation within the solder joints. The resulting

deformation causes microstructural damages within the solder region, leading to deterioration in the mechanical reliability. However, the extent of such damages would also depend on the material used for fabricating those joints, in addition to service temperatures.

Sn-based alloys contain over 95wt% β -Sn. Consequently, properties of Sn will significantly influence the mechanical reliability of Sn-based solder joints. So it is necessary to identify the contribution of high β -Sn content in Sn-based solder joints subjected to TMF.

Material independent service parameters may also influence the mechanical reliability of soldered joints. For example, during thermal excursions different stress level would result from dissimilar “temperature difference”. Such differences in service conditions would lead to different creep / stress relaxation response in Sn-based solder joints. Consequently, different service parameters will elicit different material response. Such coupling of service parameter and the solder material used may eventually determine joint service life.

1.2.1 Influence of high Sn content and intermetallic compound phases on the service reliability of Sn-based alloys

At room temperature β -Sn exists as white tin which has a Body-Centered-Tetragonal (BCT) crystal structure (Figure 1.2.1) [25, 26]. Henceforth Sn would refer to β -Sn unless stated otherwise. Lattice parameters of the BCT crystal are $c = 2.18\text{\AA}$, and $a = b = 5.83\text{\AA}$ [25, 26]. Differences in the lattice parameters result in different mechanical and thermal properties along different crystallographic directions. Table 1.1 lists elastic modulus and CTE of Sn single crystal as a

function of crystallographic direction. These values indicate the high anisotropic nature of Sn grains. Anisotropy in mechanical and thermal properties becomes particularly important during thermal excursions. Under such service conditions, stresses are generated at Sn-grain boundaries due to anisotropic CTE mismatches between adjoining grains [25, 26]. This causes different stress levels depending on the relative orientations of anisotropic Sn grains with respect to each other. Consequently, thermal excursions lead to inhomogeneous stress states within the solder region of a joint [23, 24, 26].

Additionally, Sn-based solders, due to their low melting, experience high homologous temperature during service. Temperature extremes encountered during thermal excursions range between $0.5T_m$, and $0.8T_m$. Under those conditions, solder joints would experience temperatures higher than the equicohesive temperature of grain boundaries [39]. At equicohesive temperature grain boundaries become weaker than the grain interiors. As a result, Sn-Sn grain boundary sliding occurs upon imposition of stresses resulting from CTE mismatches between Sn grains [1]. The occurrence of grain boundary sliding during TMF also indicates that joints experience creep / stress relaxation like conditions during thermal excursions [1, 21, 23, 24, 26]. Moreover, several studies have shown that decohesion / cracking also occurs at Sn grain boundaries during TMF of Sn-based solder joints [1, 21, 23, 24, 26]. Decohesion at such grain boundaries have been attributed to the presence large stresses at those boundaries during thermal excursions [25, 26].

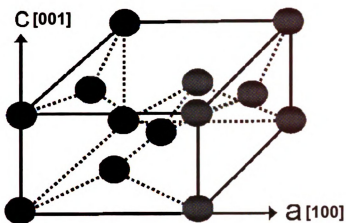


Figure 1.2.1 Schematic showing the body-centered-tetragonal crystal structure of Sn.

Table 1.1 Listing of single crystal elastic modulus "E" and CTE " α " of Sn as a function of five different crystallographic orientations. [25]

Crystallographic orientation	E (GPa)	α (10^{-6}) K^{-1}
[100]	54.1	15.4
[001]	84.7	30.5
[110]	26.3	15.4
[101]	48.1	18.9
[111]	25.5	20.5

Microstructural damage resulting from such grain boundary events (sliding /decohesion) deteriorates mechanical reliability of Sn-based solder joints [1, 21, 24-26]. In essence, Sn-based solder joints accumulate additional microstructural damage with the solder region due anisotropic CTE mismatches between Sn grains.

Moreover, presence of fewer and larger Sn grains could further exacerbate such damages, since TMF behavior of joints will be dependent on the relative orientation of Sn grains [31]. During TMF, large stresses between unfavorably oriented Sn grains will damage grain boundaries and might cause early failure of joints [31]. The possibility of large grains in Sn-based solders arises due the fact that Sn requires a large undercooling ($\sim 40^{\circ}\text{C}$) prior to solidification [8, 31]. This means as-solidified Sn –based solder may contain large grains. Puttlitz et.al. showed that damage between large Sn grains in Sn-Ag-Cu solder joints significantly reduces their TMF resistance [14].

Additionally, microstructures of Sn-based solders also have intermetallic compound (IMC) phases. Chemical composition of the IMCs depends on the minor element in Sn-based alloys. For example Ag_3Sn is present in Sn-Ag alloys, while Sn-Ag-Cu contains Ag_3Sn , and Cu_6Sn_5 IMCs. Role of these IMCs is to strengthen the solder matrix through different means. Cu_6Sn_5 have been shown to pin Sn-grains boundaries [32], while micron sized Ag_3Sn in solder joints act as obstacles to dislocation motion [33]. However, during service both Cu_6Sn_5 [21]

and Ag_3Sn [34-36] have been reported to coarsen. It should be mentioned that coarsening of Cu_6Sn_5 is a bigger issue than that of Ag_3Sn . This is so because Cu diffusion through Sn is considerably faster than that of Ag [37, 38]. Consequently, coarsening of Cu_6Sn_5 would result in fewer pinning sites at the Sn-Sn grain boundaries. Whereas larger Ag_3Sn IMC size would lead to ineffective blockage of dislocations [39]. Therefore, coarsening of IMCs during service has the capacity to compromise mechanical reliability of Sn-based solder joints.

Service conditions may also require Sn-based Pb-free solder joints to operate at sub-zero temperatures for long durations. These conditions may arise for solder joints used in devices for space and aircraft applications. At subzero temperatures Sn undergoes allotropic transformation from a ductile to a brittle phase (α -Sn). This phenomenon is called tin pest. Such a transformation occurs below 13°C. At present tin-pest has not been reported to occur during service, but is only observed under laboratory settings [24, 40, 41].

1.2.2 Influence of service parameters on the reliability of solder joints

To determine the influence of service parameters, it is important to identify the type of temperature profile appropriate for an application. This study focuses on thermal excursions prevalent in automobile under-the-hood situations and during power cycling. Figure 1.2.2 (a) shows model temperature profile experienced by solder joints under previously mentioned circumstances [1].

Service parameters associated with such thermal excursion (Figure 1.2.2), such as heating / cooling rates, dwell times at temperature extremes, and

temperature differences (ΔT), have been reported to significantly influence the reliability of Sn-based solder joints [21, 22, 42]. Furthermore, reliability of solder joints is directly related with their service life time. Based on such parameters, a simple parametric formulation was proposed by Subramanian [22]:

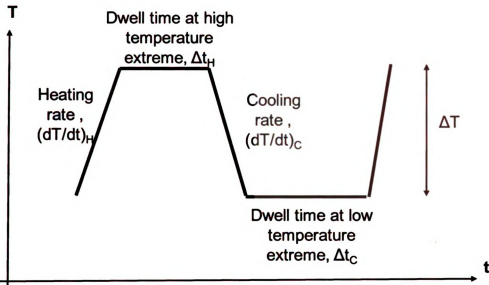
$$lifetime \sim [\Delta T]^{-m} [f]^{-n} [(dT/dt)_H]^{-p} [(dT/dt)_C]^{-q} [\Delta t_H/\Delta t_C]^{-r} [\Delta M]^s, \quad (1)$$

where, the service parameters ΔT , f , $(dT/dt)_H$, $(dT/dt)_C$, $\Delta t_H/\Delta t_C$, and ΔM are temperature difference between two extremes, frequency of TMF cycles, heating rate, cooling rate, ratio of dwell times at high and low temperature extremes, and microstructural changes during TMF respectively, while m , n , p , q , r , s are material dependant parameters. However, this model does not take into account the effect of individual temperature extremes but their difference, i.e ΔT .

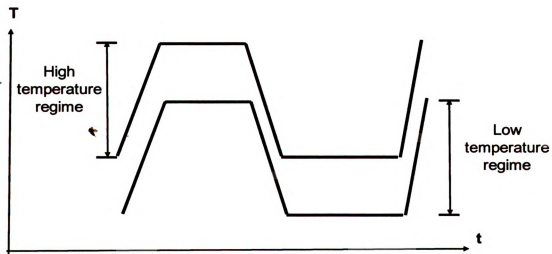
Rhee et.al. demonstrated through isothermal monotonic testing that deformation modes in eutectic Sn-3.5wt%Ag solder joints are highly temperature sensitivity [6]. That study revealed that deformation mode changes from Sn grain boundary sliding to shear banding in the neighborhood of 125°C. Similar observations were reported by Choi et.al. through creep studies on Sn-3.5wt%Ag solder joints [43]. These studies strongly suggest that deformation modes of Sn-rich (<90wt%) solders are highly susceptible to temperature extremes encountered during service. Further, microstructural damages caused by TMF, depends on deformation modes. This suggests that reliability of solder joints,

experiencing TMF, will not only depend on the mentioned service parameters but also on the temperature regimes in which ΔT is imposed (Figure 1.2.2(b)).

In essence the proposed parametric model does not include the effects of temperature regime on the TMF service life of Sn-based solder joints.



(a)



(b)

Figure 1.2.2 Schematic showing (a) different service parameters present during thermal excursions, and (b) High and low temperature regimes experienced during thermal excursions. Adapted from Subramanian [18].

1.3 Development of Pb-free Sn-based solders

Sn-based solder joints experience thermal excursions during service. Thermal excursions occur during automotive under-the-hood applications and device turn on-off type situations (power cycling) [1]. As a result of those thermal excursions solder joints experience TMF. Additionally, accidental dropping of devices result in impact loading of soldered joints [44-47]. Microstructure of an effectively designed solder should be able to handle such service conditions. Normally a fine grained microstructure provides a material with enough strength to withstand fatigue due to mechanical vibrations [2, 17]. However, solder alloys, due to their low melting points, inevitably encounter high homologous temperatures during service. At high homologous temperatures grain boundary sliding occurs in fine grained microstructure during TMF or mechanical vibrations [2]. Additionally, solder joints experience creep/stress relaxation during TMF resulting in a requirement for a stronger solder matrix. However, the solder matrix should be compliant enough to withstand stresses generated due to imposed ΔT . This presents a demand for a solder material that has both high strength and ductility.

Furthermore, high temperature aging causes coarsening of IMCs (e.g. Ag_3Sn and Cu_6Sn_5) present in the microstructure. These IMCs are known to provide strength to the solder matrix. Microstructural instability resulting from coarsening of IMCs would further lead to weakening of the solder matrix. Consequently, development of Sn-based solder must balance the need for strength and compliance, while simultaneously retarding service induced microstructural

changes. Additionally, implementation of such solders should require minimal changes in the established industrial processes. To summarize, a well designed Sn-based Pb-free solder must perform the following roles:

1. Engineer microstructure: A fine grained microstructure while simultaneously retarding grain boundary sliding.
2. Accommodate imposed stress/strain without losing strength. In other words potential Sn-based solder candidates must have both ductility and strength.
3. Stabilize microstructure: Retard IMC coarsening.
4. Amenable to ease of processing and implementation

1.3.1 Alloying approach

As mentioned in section 1.1, Sn-Ag and Sn-Ag-Cu family of solder alloys are seen as possible replacements for Sn-Pb alloys. Recently, Sn-Ag-Cu alloys are experiencing more commercial use and subsequently being studied extensively [8, 11-13, 48]. In particular near eutectic Sn-3.9wt%-0.6wt%Cu and Sn-3.0wt%-0.5wt%Cu have been recommended by National Electronics Manufacturing Initiative (NEMI) and Japan Electronics Information Technology Industries Association (JEITA) respectively [49, 50]. However, reflowed microstructure of those Sn-Ag-Cu alloys contains either large Sn primary dendritic structure or large IMC particles [8, 11-13, 48]. Such a coarse microstructure results due to the large undercooling experienced by Sn rich matrix during solidification [31]. Consequently, there is a need for refining Sn-Ag-Cu microstructure.

One of the approaches taken was to change the compositions of Ag or Cu in Sn-Ag-Cu [8]. This approach was based on the assumption that Cu_6Sn_5 IMC particles promote heterogeneous nucleation of primary Sn. Studies carried out by varying the concentrations of both Cu and Ag, Anderson et.al. found that Sn-3.6wt%Ag-1.0wt%Cu had the most refined microstructure [8, 11, 48]. It was also shown that Sn-3.6wt%Ag-1.0wt%Cu had a higher shear and yield strength than eutectic Sn-Ag. However, Sn-3.6wt%Ag-1.0wt%Cu had a lower ductility than eutectic Sn-3.5wt%Ag as compared to other Sn-Ag-Cu alloys studied. To simultaneously refine the microstructure and retain ductility (as compared to eutectic Sn-Ag) minor concentrations of Co and Fe were added to Sn-Ag-Cu alloys resulting in quaternary Sn-Ag-Cu-X (X=Co, Fe) alloys. It was found that both additions refined the microstructure, but microstructure of Sn-Ag-Cu-Co was comparatively more refined. The resulting refinement was attributed to the presence of Co-Sn and Co-Sn-Cu IMCs. It was suggested that during solidification those IMCs promoted the heterogeneous nucleation of Cu_6Sn_5 , which in turn assisted in the nucleation of Sn. Furthermore, Co and Fe additions resulted in similar ductility and strength as that of eutectic Sn-Ag [8, 11, 12, 48]. Although Co and Fe additions resulted in desired improvements, presence of Cu_6Sn_5 IMC within the microstructure is a source of concern. Cu_6Sn_5 in Sn-Ag-Cu solder joints has been known to coarsen during TMF [21]. Such coarsening contributed to the deterioration in the mechanical reliability of Sn-Ag-Cu solder joints subjected to TMF [21]. Similar coarsening of IMCs during TMF was also

observed in quaternary Sn-Ag-Cu-Bi and Sn-Ag-Cu-In alloys, even though Bi and In additions improved the fatigue life of solder joints [51].

Later Subramanian et.al developed Sn-Ag-Cu-Ni quaternary alloy systems that reduced Cu_6Sn_5 IMC coarsening during TMF. The improved microstructural stability was due to the presence of $(\text{CuNi})_6\text{Sn}_5$ IMC in those alloys, which prevented diffusion of Cu through Sn [1, 2, 52]. Furthermore, $(\text{CuNi})_6\text{Sn}_5$ IMC pinned Sn grain boundaries thereby retarding Sn-Sn grain boundary sliding and improving TMF reliability. However, those studies were more focused on the improving the TMF reliability of Sn-Ag-Cu-Ni solder joints, rather than determining influence of Ni additions on solidification behavior of Sn-Ag-Cu. Later, Anderson et.al. showed that Ni additions to Sn-Ag-Cu results in microstructural refinement very similar to Co and Fe additions [13]. Consequently, it seems that minor additions to Sn-Ag-Cu do have the potential to improve the service life of solder joints. However, implementation quaternary Sn-Ag-Cu-X (X = Co, Fe, Bi, In Ni) solders may depend on the flexibility of the existing processes in the industry.

Another alloying approach that has received much attention is the addition of rare earth (RE) elements to existing Sn-based alloys. Typical RE used lie within the lanthanide series of the periodic table. Among those La and Ce are most commonly used elements [2, 53]. Such RE additions are found to improve both ductility and strength [53]. Furthermore, RE additions also result in a refinement of Sn dendrites and IMC particles [53]. In Sn-Ag-Cu alloys RE

additions decrease the size of both Cu_6Sn_5 and Ag_3Sn IMCs [53]. Furthermore, refined Sn dendritic structure observed in Sn-Ag-Cu-RE alloys also suggests that RE elements act as nucleating agents for Sn [53]. Wu et.al. suggested that such refinement is caused by the presence of RE at different interfaces (namely IMC/Sn , Sn-Sn grain boundaries etc.) [53]. This was further confirmed through isothermal aging studies by Pei et.al. They showed that coarsening of Ag_3Sn IMC is retarded by La additions [54]. Clearly alloying with RE improves mechanical properties and microstructural stability of the base alloy. However, cost and availability of RE might be an issue in their implementation.

1.3.2 Composite approach

Composite solder is another technique which is being vigorously pursued by our group and other researchers [2]. The prime motivation for this approach is to engineer microstructure of commonly used solder alloys so as to improve creep properties and TMF resistance [2]. This approach involves incorporation of reinforcements in the solder matrix without increasing the melting point of the material [2]. Additionally, such reinforcements have the potential to pin grain boundaries and consequently improve the TMF resistance of Sn-based solder joints.

Presently, there exists a variety of techniques which fulfill the aforementioned requirements. One such technique involves incorporation of compatible IMC, e.g Cu_6Sn_5 , FeSn / FeSn_2 , and Ni_3Sn_4 , reinforcements by *in-situ* or mechanical mixing methods [2, 3, 52]. Isothermal aging studies carried to

evaluate microstructural stability of such IMCs showed that FeSn / FeSn₂, and Ni₃Sn are relatively more stable than Cu₆Sn₅ [2, 3, 52]. Nonetheless, IMC reinforcements have the tendency to coarsen, which would be detrimental to the mechanical reliability of solder joints. On the other hand, Cu₆Sn₅ reinforcement improved creep resistance of Sn-3.5wt%Ag solder joints as compared to FeSn / FeSn₂, and Ni₃Sn₄. [2, 3]. Even though Cu₆Sn₅ improves creep resistance, its applicability as a potential reinforcement was limited by the fact that it coarsens during TMF [2, 3, 21].

These studies on IMC reinforcements (Cu₆Sn₅, FeSn / FeSn₂, and Ni₃Sn₄) showed that microstructural stability is a problem, since the reinforcements tend to coarsen rapidly during isothermal aging. Consequently, other types of inert, and non-coarsening reinforcements have been utilized. Fe and ceramic (Al₂O₃, TiO₂) reinforcements fall in such a category. These reinforcements improved the strength and creep resistances of solders [2, 55]. However, viability of such an approach is limited by the fact that those reinforcements do not bond with the Sn-rich matrix, and tend to agglomerate during the reflow process [2, 55]. In an attempt to reduce agglomeration, reinforced solders were rolled to crush and disperse the particulates. In addition to adding an extra processing step, this approach resulted in interfacial cracking between the reinforcement and the matrix [55].

Another approach proposed by Subramanian et.al. was the incorporation of micro-sized Ag, Cu and Ni metallic particles to Sn-Ag based solders [2, 3, 55]. Ag, Cu, and Ni reinforcements bonds with Sn-rich matrix through the formation of interfacial IMCs Ag_3Sn , Cu-Sn (Cu_3Sn , and Cu_6Sn_5), and $(\text{CuNi})_6\text{Sn}_5$, respectively. In terms of microstructural stability Ag reinforcements proved to be better than Cu and Ni [2]. However, Ni reinforced Sn-3.5wt%Ag solder joints demonstrated improved creep resistance as compared to Cu and Ag reinforcements [2, 3]. Although Ni particles improves the creep resistance but it is difficult to control their size and distribution during the reflow process [55]. This could be a source of concern for microelectronics industry which is increasingly driven towards miniaturization [55]. Consequently, a requirement for sub-micron size reinforcements arises.

Based on the literature review, it is found that a potential reinforcement should satisfy the following minimum requirements:

1. Does not coarsen during service,
2. Bonds with the Sn-rich solder matrix
3. Pin grain boundaries
4. Provide ease of processing without introducing additional costly steps, and
5. Sub-micron sized and have relatively uniform distribution throughout the matrix

1.3.3 Development of nano-composite solders using nano-structured chemicals

Polyhedral oligomeric silsesquioxanes (POSS) are nano-structured chemicals with an average diameter of 1.5nm [55]. These chemicals are cage like structure with repeated monomer units of $\text{SiO}_{1.5}$ with a hydrocarbon (R) group, eg. Iso-butyl, phenyl etc., attached to the Si atoms [55]. Examples of POSS have been shown in Figures 1.3.1. These figures show that POSS can be either a complete cage (Figure 1.3.1 (a)) or an incomplete cage with silanol (Si-OH) bonds replacing a Si atom at the corner (Figure 1.3.1 (b)). Schematic shown in Figures 1.3.1(b) are among of the several structural variations of POSS [56, 57]. Utilizing appropriate chemical synthesis routes one can tailor the number of Si-OH bonds and Si atoms attached to the $\text{SiO}_{1.5}$ cage [58]. However, for this review and the studies presented in the following sections (and chapters), role Si-OH bonds are of consequence.

POSS with silanol groups are known to form thermodynamically feasible bonds with Sn (Si-O-Sn) [55]. Essentially, these bonds are formed between oxygen and metal atoms following breakage of O-H bonds, while Si-O bond remains intact. This is evident from Table 1.2, which compares different oxygen-metal bond energies with that of Si-O and O-H bonds present within POSS. Consequently, POSS *with surface active Si-OH* presents itself as a viable alternative reinforcement, since it can form bonds with Sn-rich solder matrix. Furthermore, bonded POSS cages will not coarsen during service since that

would involve breaking very strong bonds. This suggests that bonded POSS cages are inert during service. Additionally, POSS with silanol groups are thermally stable till 300°C [55, 59, 60]. This temperature is considerably higher than the melting points of most Sn-based solder alloys and processing temperatures used for fabricating soldered joints with such alloys. As a result degradation of the POSS structure is unlikely during processing.

Effect of POSS reinforcements on the thermo-mechanical behavior and TMF service mechanical reliability of Sn-3.5wt%Ag solder joints has been investigated by Lee et.al [55]. Their experiments strongly suggested that POSS with surface active Si-OH bonds with the solder matrix, and does not agglomerate during the reflow process indicating ease of processing.

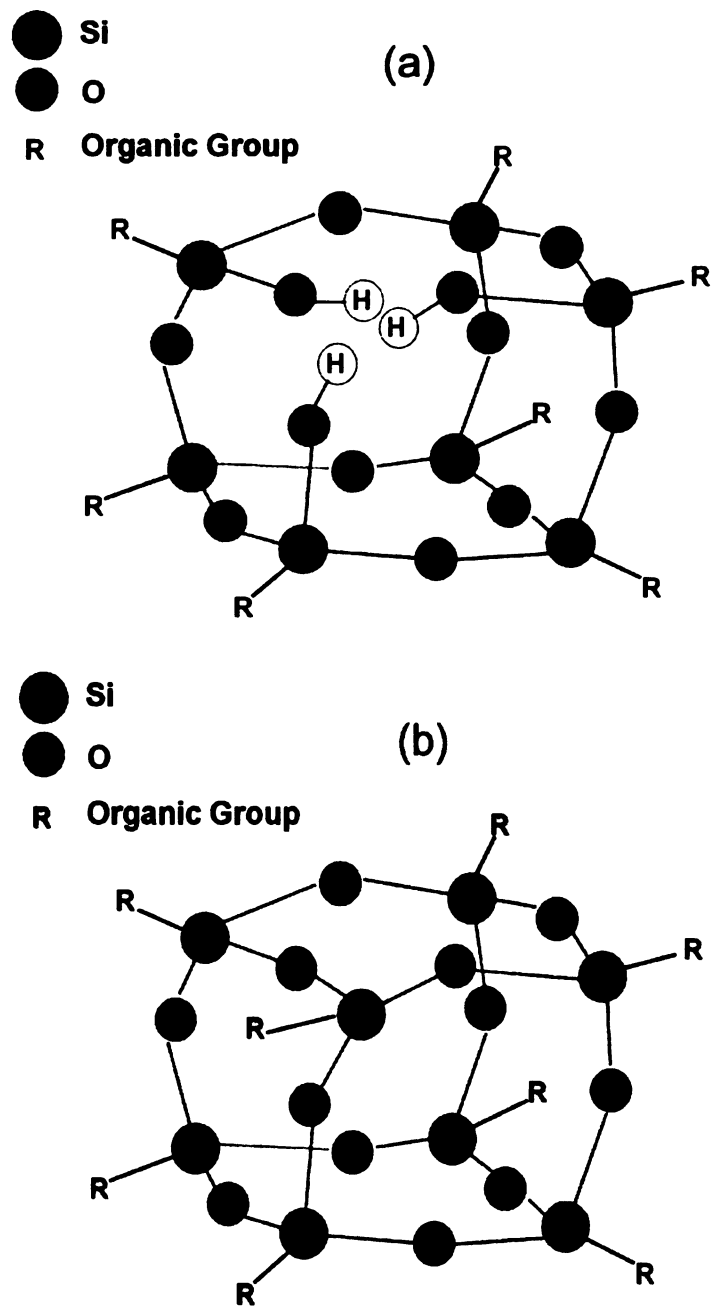


Figure 1.3.1 Schematic showing two different types POSS anatomies (a) Trisilanol POSS with three Si-OH groups, (b) Octa POSS without any Si-OH groups.

Table 1.2 Bond energy values at 25°C [61].

Bond types	Bond energies(KJ/mol)
Si-O	799.6
Si-C	447.0
Sn-O	528.0
Cu-O	287.4
Ag-O	221.0
O-H	248.8

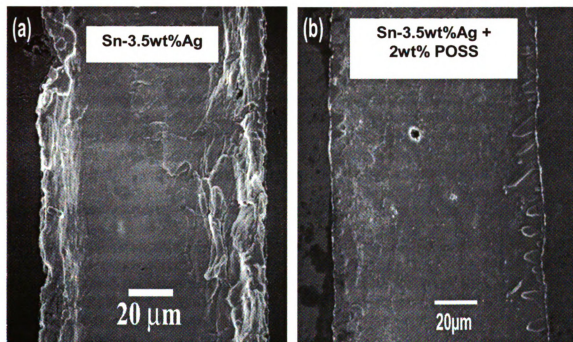


Figure 1.3.2 SEM images showing microstructural damages after 1000 cycles of TMF in (a) eutectic Sn-3.5wt%Ag (adapted from Lee et.al. [21]), and (b) eutectic

Sn-3.5wt%Ag reinforced with 2wt% (10 vol%) POSS with Si-OH groups (adapted from Lee et.al. [55]).

Monotonic shear testing revealed that POSS reinforced solder joints were relatively insensitive to strain rates, suggesting that the reinforced matrix is able to accommodate imposed stress/strain. Finally, TMF studies showed that, POSS pins Sn grain boundaries from sliding or debonding [55]. Figures 1.3.2 compares the microstructures of solder joints with and without POSS reinforcements after 1000 cycles of TMF. Figure 1.3.2(a) shows surface damage manifestation in form of grain boundary sliding in Sn-3.5wt%Ag, while reinforcing with POSS results in lack of such damages (Figure 1.3.2(b)).

Evidently, incorporation of POSS reinforcements within solder matrix presents an attractive potential option for implementing composite solder. To establish the viability of POSS as reinforcement, the following studies on Sn-based Pb-free solders are warranted:

1. *Effect of POSS additions on the TMF behavior of solder joints*
2. *Influence of POSS additions on the microstructural features and its stability during service.*

1.4 Research strategy

Based on this literature review it was noted that temperature regime, within which solder joints experience thermal excursion, might influence the mechanical reliability of Sn-based solder joints. To validate this hypothesis, Sn-based solder joints have been subjected to a lower temperature regime as compared to previous studies [1, 20, 21, 32, 42]. For this purpose, model Sn-3.5wt%Ag solder was utilized. Effect of low temperature regime TMF was evaluated through

microstructural and mechanical characterization techniques. Results of this investigation and the corresponding discussion are presented in chapter 3. These results would serve as a baseline for evaluating the effects of POSS reinforcements on mechanical reliability of Sn-based solders.

Chapter 4 presents the study on the effects of POSS additions on the TMF behavior of Sn-based solder alloys. However, only the effect of low temperature TMF is studied, since Lee et.al. has already investigated the effect of high temperature regime TMF on POSS reinforced Sn-3.5wt%Ag solders [55]. The methodology for characterization in this chapter is similar to the ones in chapter 3.

As pointed out earlier, any additions (alloying elements or reinforcements) that can bond with the metal matrix can influence the microstructure of the base alloy. Consequently, chapter 5 assesses the effects of POSS additions on the microstructure of bulk specimens.

Microstructural stability during service is one of the requirements in the development of Sn-based solder. This aspect is investigated in chapter 6 by observing the effects of POSS on the coarsening behavior of Ag_3Sn IMC.

Chapter 2

Experimental Procedure and methods

2.1 Materials and processing

Eutectic Sn-3.5wt%Ag (SA) and Sn-3.0wt%Ag-0.5wt%Cu (SAC305) solder pastes (Kester [®]) were used in this study. Each variety of paste contained of ~89 wt % alloy while the rest was water soluble flux. Commercial brand of the solder pastes was R520A. Nanostructured chemical used were (i) Iso-Butyl trisilanol POSS, and (ii) Iso-Butyl Octa trisilanol POSS. These chemicals were obtained from Hybrid Plastics[®]. All the pastes and chemicals were kept in a refrigerator when not used.

Nanostructured POSS was added into the solder pastes through mechanical mixing at room temperature (~25[°]C). Glass petri dish and stainless steel spatula were utilized for mixing, and were thoroughly cleaned with isopropyl alcohol prior to usage. The mixing procedure involved two steps. First, ~10 grams of solder paste was weighed in a petri dish using a precision microbalance. This was followed by addition of ~0.2 grams of a particular type of nanostructured POSS chemical (usually white colored powder) to the paste. This quantity of POSS was 2% of the total weight of the solder paste used. Finally, the solder paste and the chemical were thoroughly mixed in the glass petri dish for ~20 minutes with a stainless steel spatula till the whitish powder is not visible. The methodology adopted for adding POSS to solder pastes offers both ease of

processing and economically viability. Following preparation all the solder pastes were stored in a refrigerator.

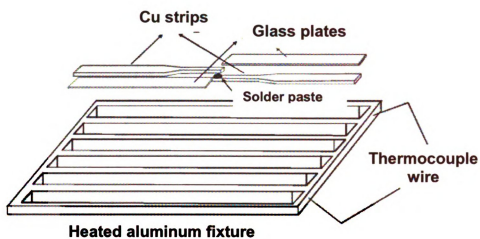
2.2 Preparation of Solder Joints

Copper dog-bone halves (500 μ m thick) were initially washed with 30% volume HNO₃ to remove surface oxide. This was followed by rinsing them in distilled water and finally isopropyl-alcohol. Two “cleaned” Cu dog-bone halves were placed in an aluminum fixture (Figure 2.2.1(a)) with the narrower ends overlapping an area of $\sim 1\text{mm}^2$ with solder paste between them and spaced vertically by $\sim 100\mu\text{m}$ by 600 μm glass spacers (Figure 2.2.1 (a)). Geometry and dimensions of the fabricated solder joint have been shown in Figure 2.2.1 (b). The final assembly had appropriate amount of solder paste sandwiched between the overlapping Cu dog-bones. The whole assembly was then heated up to 250 °C on a hot plate which was preheated to 500 °C. Heating / cooling profile used for this purpose are shown in Figure 2.2.1(c). After preparation all the specimens were stored in a commercially available refrigerator.

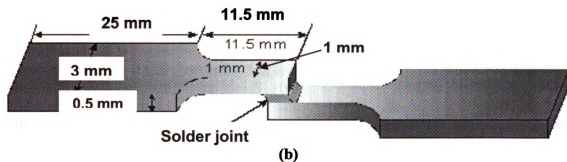
2.3 Preparation of bulk alloy specimen

Bulk specimens were prepared by placing solder paste in an aluminum cup of fixed diameter then heating the whole setup at 280 °C. Temperature in all the experiments was controlled with a commercially available digital temperature controller. Figure 2.3.1 shows the experimental setup used for melting the bulk solder. Specimens were kept on the hot plate for approximately 15 minutes to ensure the all the flux has evaporated, leaving behind just the molten alloy inside

the cup. In order to solidify the molten alloy, the cup was quickly removed from the hot plate and placed on a surface which was maintained at a constant temperature. Details of the temperatures used would be provided in Chapter 5. After solidification bulk specimens were washed with water and isopropyl alcohol to remove the excess flux from the specimen surface. The solidified specimens were then stored in a commercially available refrigerator.

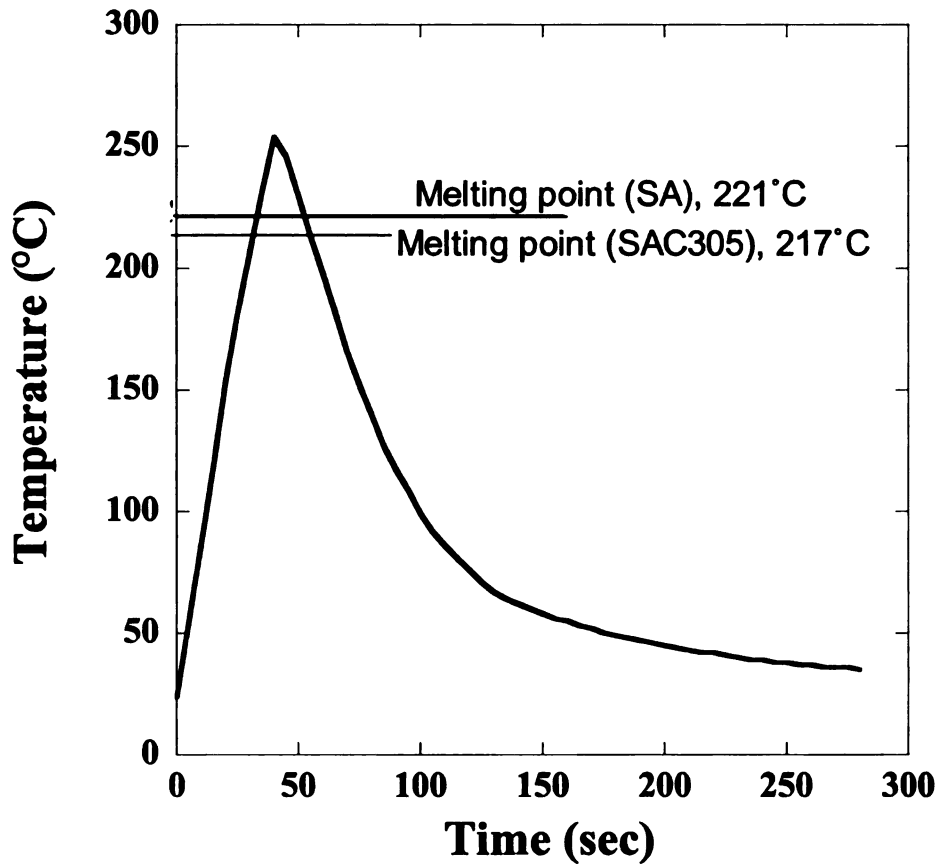


(a)



(b)

Figure 2.2.1 Apparatus used for fabricating solder joints (a) aluminum fixture used for positioning the half dog bone copper strips, (b) schematic of a solder joint with dimensions shown. (Adapted from J G Lee thesis [1]).



(c)

Figure 2.2.1 (c) Temperature profile used for fabricating solder joints . (Adapted from J G Lee thesis [1]).

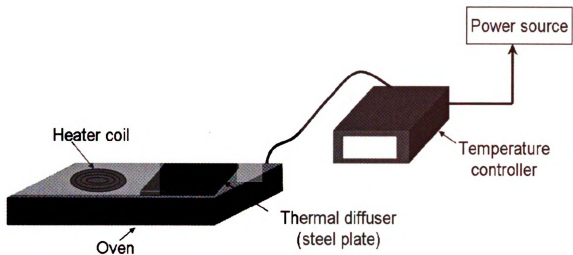


Figure 2.3.1 Schematic showing the experimental set-up used for the preparation of bulk specimens.

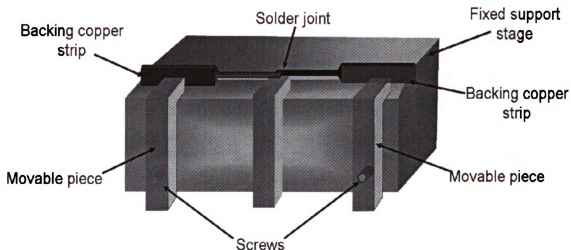


Figure 2.4.1 Schematic showing the jig used for holding solder joints during polishing. The wider ends of the joint are backed up with Cu strips of similar thickness as that of the half dog-bone pieces. This prevents bending or twisting of the joint (at the center) during polishing.

2.4 Procedure for polishing joint and bulk specimens

Prior to polishing as-fabricated solder joints were placed on a custom built jig (Figure 2.4.1) so as to keep it steady during the polishing procedure. All joints were polished sequentially with 800-2400 grit papers, followed by 0.3 μm Al_2O_3 and 0.05 μm colloidal- SiO_2 solutions.

However, bulk specimens were polished sequentially with 200, 800-2400 grit papers, followed by 0.3 μm Al_2O_3 solution. Polishing of bulk specimens with 0.3 μm Al_2O_3 solution was carried out in two stages. The first stage involved polishing the specimen vigorously to remove SiC particles embedded on the surface from the previous polishing step. This additional step decreases the time required for the polishing process, but leaves surface scratches. Consequently, in the next step, the polishing cloth was again cleaned and then the specimen was polished in a slow and gentle manner with 0.3 μm Al_2O_3 solution. This step ensured a mirror like finish to the specimen surface. Final polishing step was carried out with 0.05 μm colloidal SiO_2 solution, where the specimen was polished as gently as possible so as to avoid any scratches.

To avoid debris from the previous polishing steps, specimens (joint or bulk specimens) were ultrasonically cleaned after each step of polishing. After polishing all the specimens were stored in a commercially available refrigerator maintained at 4°C.

2.5 Setup for TMF experiments

Solder joint specimens were thermally cycled inside a microclimate environmental chamber (Cincinnati Sub-zero®) (Figure 2.5.1). This chamber has an inbuilt air circulatory system, which maintains uniform temperature throughout the chamber. Prior to thermal cycling, solder joints were placed on grooves of a custom built stage (Figure 2.5.2). This set-up prevented the joints from displacing under the influence of the circulating air inside the chamber. Finally a programmed temperature profile was executed to thermally cycle the specimens between -55°C and 125°C . Figure 2.5.3 shows the comparison between the programmed and the actual temperature profile. Each cycle had an average heating rate of $3.9^{\circ}\text{C}/\text{min}$ with a dwell time of ~ 10 min at 125°C ; along with an average cooling rate was $2.4^{\circ}\text{C}/\text{min}$ and the dwell time was ~ 45 min at -55°C . Consequently each thermal cycle would take ~ 3 hours. To characterize the effects of TMF on solder joints due to such thermal cycling a chosen number of specimens were taken out the chamber after 1, 25, 50, 100, 200, 300, 400, 500,



Figure 2.5.1 Image showing the environmental chamber used for conducting
TMF experiments

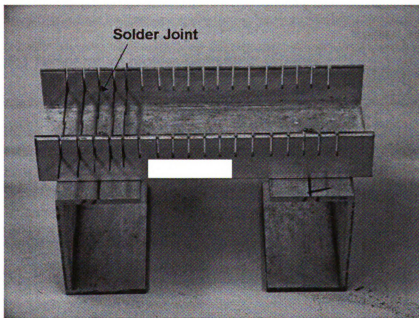


Figure 2.5.2 Image showing the custom built stage used for placing solder
specimens inside the environmental chamber.

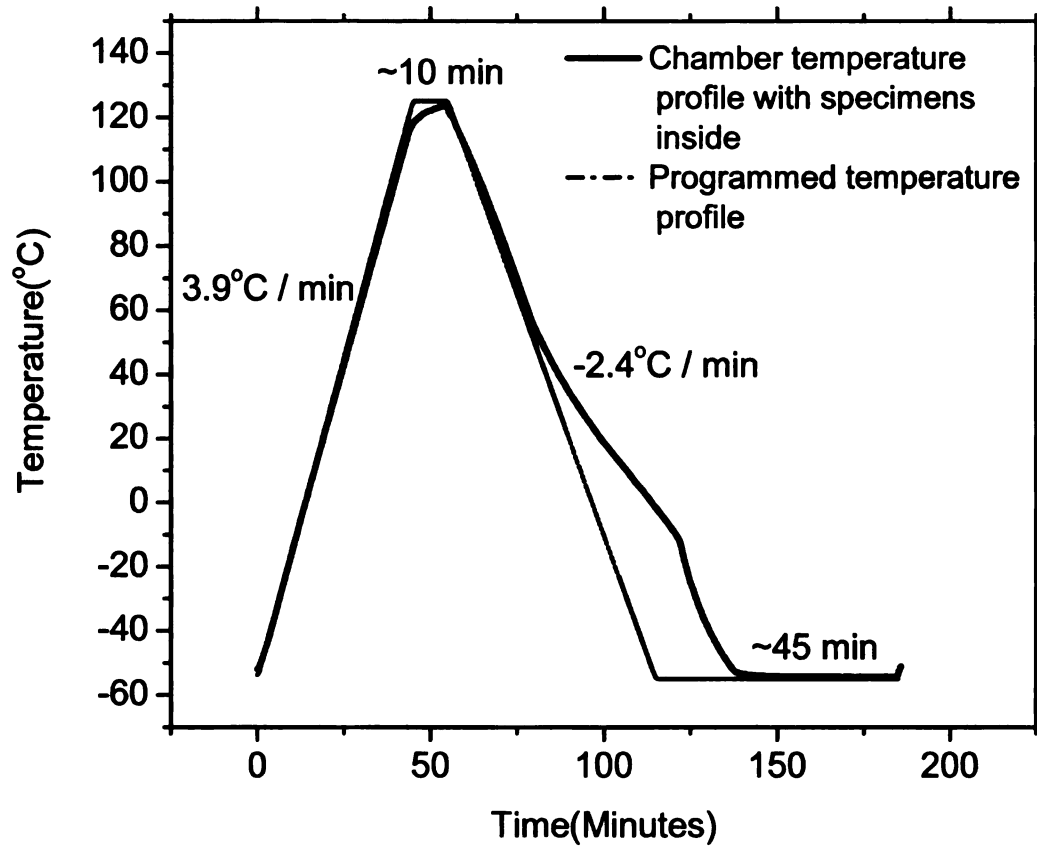


Figure 2.5.3 Temperature profiles used for thermally cycling the solder joints.

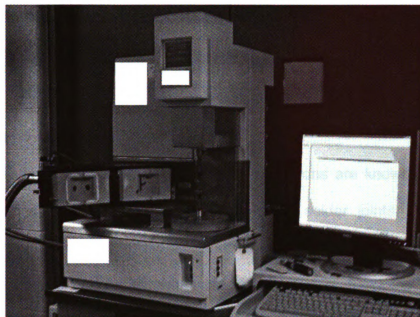
and 1000 cycles. These specimens were temporarily stored within a commercial refrigerator at 4 °C prior to characterization.

2.6 Mechanical and microstructural characterization

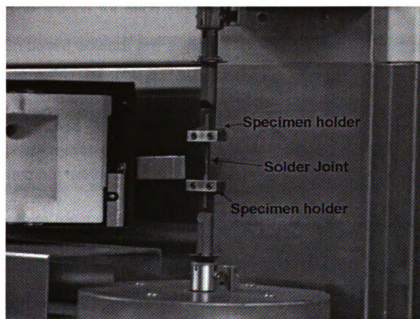
Mechanical characterization of solder joints were carried out using Rheometric Solids Analyzer (RSA-III) which is a highly force sensitive tensile testing type machine. Figure 2.6.1 shows the set-up used for mechanical testing. Batches of solder joints, which were thermally cycled for 1, 10, 25, 50, 100, 200, 300, 400, and 500 TMF cycles, were strained to failure for this mechanical characterization at 25 °C with a simple shear strain rate of 10^{-3} s^{-1} . This provided the peak force (in Newtons) required for breaking the solder joints. Optical microscope was used to measure the surface area of the fracture surface. This was necessary because there are voids present in the as-fabricated solder joints, whose area had to be subtracted from the total joint surface area. Measurements of areas were carried out by processing of digitally acquired optical images with ImageJ® software. The resultant area of the fracture surface (excluding void) was used to calculate the peak stress.

Microstructural characterization was carried out with a JOEL 6400 Scanning Electron Microscope (SEM). For this purpose, representative solder joints were metallurgically polished (c.f. section 2.4) on one side, prior to placing them in the environmental chamber. These specimens were taken out of the chamber at periodic intervals and the resultant surface damage was documented

using SEM. Microstructures of bulk specimens were characterized with both SEM and Optical Microscope (OM).



(a)



(b)

Figure 2.6.1 Set-up used for mechanical characterization (a) RSA III used, and
(b) location of the solder joint inside the specimen holder of RSA III

Chapter 3

Effect of temperature regimes on the thermomechanical fatigue behavior of eutectic Sn-Ag joints

Rationale and objectives

Service parameters associated with thermal excursions are known to influence the thermomechanical fatigue (TMF) behavior of solder joints. Parameters related to thermal excursions, like temperature difference, heating / cooling rates, dwell times at temperature extremes etc. are known to affect the mechanical reliability of Sn-based solder joints. However, temperature regimes, between which solder joints experience TMF, may also influence their residual mechanical behavior. The reason for such influences is due to the fact that deformation modes of Sn-based solders are a strong function of the ambient temperature. Consequently, the present study investigates the influence of *low temperature regime* TMF between -55°C and 125°C on eutectic Sn-3.5Ag solder joints. This study is carried out using identical specimen geometry as those used for studying *high temperature regime* TMF between -15°C to 150°C . This chapter presents microstructural evolution with number of TMF cycles, and mechanical characterization of residual strength realized under *low temperature regime* TMF, and compares them with those observed under *high temperature regime* TMF.

3.1. Background

Mechanical reliability of Sn-based solder joints is known to deteriorate due to thermal excursions experienced during service [23]. This deterioration of properties is referred as thermomechanical fatigue (TMF). The degree and manner of property degradation attributed to TMF are influenced by thermal service environmental parameters such as temperature difference between extremes, dwell time at temperature extremes, heating and cooling rates, etc [21, 42]. The roles of each of these service parameters on different Pb-free Sn-based alloys have been investigated using joints of same geometry, and varying a single service parameter while holding all other parameters fixed [22]. The extent of degradation of these individual parameters are evaluated by comparing residual properties, such as strength and electrical conductivity after exposing these joints to varying number of TMF cycles [22]. The manner of degradation is evaluated by monitoring surface damages accumulation of a single specimen after exposing it to different number of TMF cycle [19-21, 42]. In addition to these service parameters, the mechanical testing conditions used to evaluate residual properties can also influence the findings since the mechanical responses of Sn-based alloys are temperature and strain-rate sensitive [6]. This temperature and strain-rate sensitivity influences on deformation of Sn-based alloys suggest that the TMF behavior of these alloys may be affected by the temperature regimes and extreme temperatures encountered during thermal cycling.

There are reported studies on effect of thermal cycling of various solder alloys at temperature regimes of -40°C to 125°C , and -15°C to 150°C [24, 51,

62]. Although the imposed temperature difference in both these studies was the same, specimen geometry, type of solders and substrates used, dwell time at temperature extremes and heating/cooling rates, etc. were different from each other [24, 51, 62]. Therefore, it is difficult to use these results to assess the solder joint reliability due to TMF as affected by the temperature regimes. In the past several years, systematic studies using identical single shear-lap solder joint geometry have been carried out in the temperature regime of -15°C to 150°C to evaluate the effects of heating rate and dwell times on the TMF behavior of several Sn-based solders including eutectic Sn-3.5wt%Ag solder [3, 18-24, 42]. The present study investigates the responses of the same eutectic Sn-3.5wt%Ag solder joints subjected to thermal cycling at temperature regime of -55°C and 125°C , while using the same joint geometry with similar dwell time at temperature extremes and ramp rates used in prior studies, so that effects of temperature regime can be compared. The temperature difference used here is slightly different from prior studies due to the following reasons. It is known that the deformation behavior of Sn changes in the temperature range of 100°C to 125°C [7]. So it is essential to keep the upper temperature extreme at least at 125°C to avoid unnecessary complications from different deformation modes. In addition, thermal cycling between -55°C and 125°C is currently used as the most severe thermal testing standard established by the Joint Group on Pollution

Prevention for Pb-free solder alloys. Hence the lower temperature extreme of -55°C was chosen for this study.

3.2. Experimental details

Single shear-lap solder joints were prepared using commercially available Sn-3.5wt%Ag solder paste purchased from a commercial source. Machined spacers used during fabrication of joints helped to maintain a relatively constant joint thickness of about $100 \pm 5\mu\text{m}$. The exact thickness of joints was measured with an optical microscope for determining the displacement rates and shear strains needed for mechanical characterization. Fabrication details of these solder joint specimen are described in chapter 2. All solder joints were thermally cycled from -55°C to 125°C using a bench top model of MicroClimate[®] test chambers by Cincinnati Sub-Zero with a programmable controller. Test specimens were placed in the environmental chamber that was initially at -55°C . It is then heated with an average rate of 3.9°C per minute to 125°C , and held at this temperature for 10 minutes. Following this high temperature dwell specimens were cooled to -55°C with an average cooling rate of about 2.4°C per minute. The dwell time at -55°C was set for 45 minutes. This thermal profile was cycled during TMF testing. Programmed and the actually measured temperature profiles experienced by specimens have been described in chapter 2.

Microstructural characterization was carried out using a Scanning Electron Microscope (SEM). For this purpose, representative Sn-3.5wt%Ag solder joints were metallographically polished on one side, prior to placing them in the environmental chamber. These specimens were taken out of the chamber at periodic intervals and the resultant surface damage was documented using SEM. Mechanical characterization was carried out using a mechanical solids analyzer (RSA-III) by TA Instruments. Batches of Sn-3.5wt%Ag solder joints, which were thermally cycled for 1, 10, 25, 50, 100, 200, 300, 400, and 500 TMF cycles, were strained to failure for this mechanical characterization at 25 °C with a simple shear strain rate of 10^{-3} s^{-1} . Eight to ten specimens were used to study each condition so that the results obtained provide realistic trends. Fractured surfaces of the mechanically tested specimens were examined to identify the failure path, and to obtain the actual joint area that contributed to the strength of the joint. This methodology is well documented in prior publications [19, 20]

3.3 Results and discussion

3.3.1 Microstructural Evaluation of Damages resulting from Low Temperature Regime TMF

To assess the evolution of surface damage, three regions were chosen on the polished side of the representative solder joint. Schematic provided in Figure 3.3.1 indicate the locations of these regions, which, hereafter will be referred to as regions 1, 2 and 3. Microstructural evolution in these regions with increased

number of TMF cycles is presented in Figures 3.2, 3.3 and 3.4. All these images reveal that damage accumulates from very early stages of TMF, i.e. within the

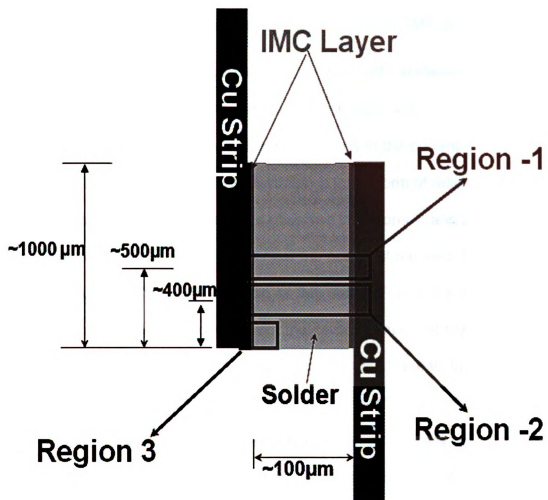


Figure 3.3.1 Schematic of the regions on the solder joint observed for microstructural evolution. Region-1 is at the center, region-2 is $\sim 100\mu\text{m}$ below region-1 and region-3 is at the IMC / Solder interface.

first 50 cycles, unlike in specimens subjected to TMF in -15°C to 150°C range [21, 42]. In that *high temperature regime* TMF, surface manifestation of damage was first noted only after about 250 cycles [21, 42].

The surface manifestation of damage noted in the current study occurs in two ways. First type of surface manifestation is in the form of relief features within the solder region. Such features were observed in regions 1, and 2 (Figures 3.3.2 and 3.3.3). In region 3, which is very near the corner of the joint, this feature was absent throughout the entire duration of this study (Figure 3.3.4). In region 1, such damage appears to proceed from the center of the joint towards the IMC / solder interface at an angle of approximately 30° with the IMC layer, whereas in region 2, damage runs almost parallel to the IMC/solder interface. These observations suggest that surface relief features within the solder matrix may be due to thermal stresses arising from the anisotropy of Sn during TMF. Furthermore, the localized nature of surface damage is due to the inability to dissipate these stresses by plastically deforming the Sn grains. Hence grains move relative to each other by mode-II or mode-III types of fracture.

The second type of surface manifestation noted is the debonding between the Cu_6Sn_5 IMC and Sn grains. Such debonding occurs both at the solder matrix and the Cu_6Sn_5 IMC layer it forms with the substrate, as well as within the solder matrix and the Cu_6Sn_5 particles embedded in it. This type of surface

manifestation is observed prominently after 100 cycles in all three regions of the joint.

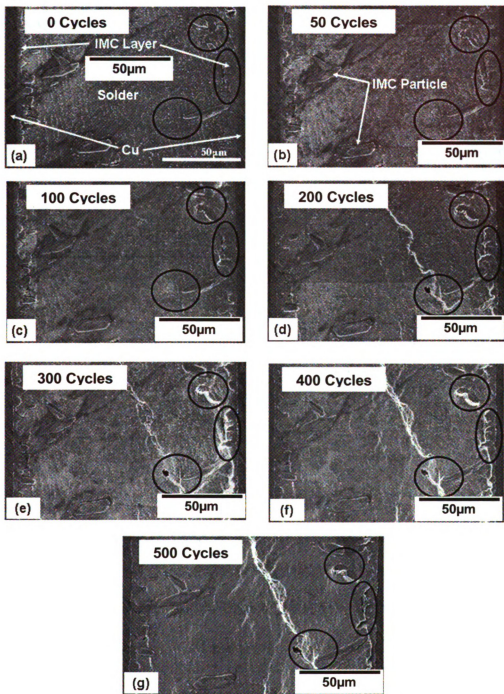


Figure 3.3.2 SEM images of region 1 showing the evolution of surface damage within the solder and near the IMC layer and at the Cu_6Sn_5 IMC / solder interface after (a) 0, (b) 50, (c) 100, (d) 200, (e) 300, (f) 400, (g) 500 cycles of TMF. Scale bar indicates 50µm.

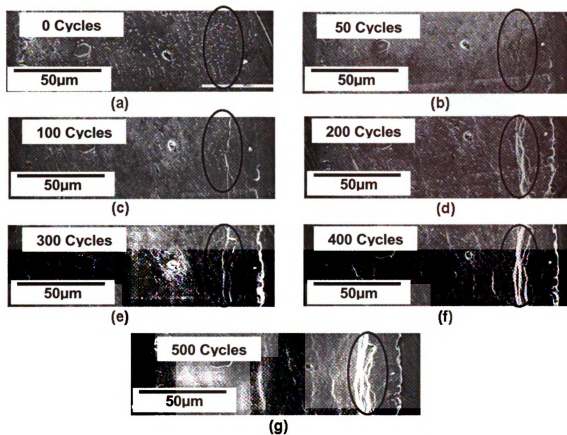


Figure 3.3.3 SEM images of region 2 showing the evolution of surface damage near the Cu_6Sn_5 IMC layer and at the Cu_6Sn_5 IMC /solder interface after (a) 0, (b) 50, (c) 100, (d) 200, (e) 300, (f) 400, (g) 500 cycles of TMF. Scale bar indicates 50µm.

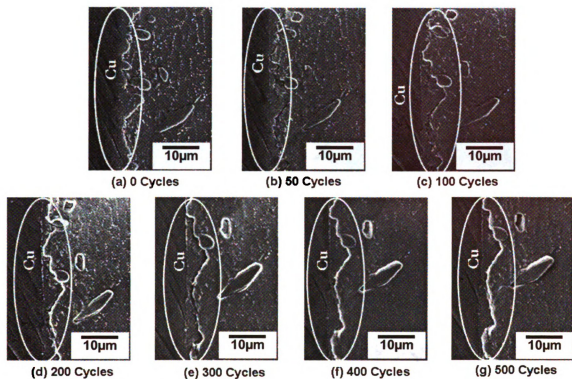


Figure 3.3.4 SEM images of region 3 showing the evolution of surface damage at the IMC/solder interface after (a) 0, (b) 50, (c) 100, (d) 200, (e) 300, (f) 400, (g) 500 cycles of TMF. Scale bar 10µm.

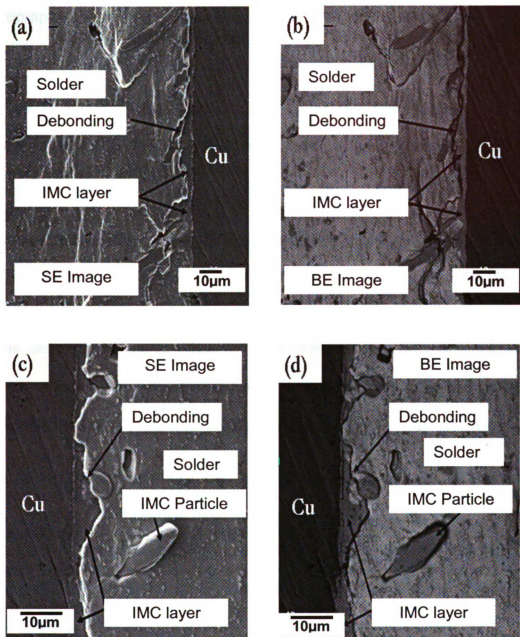


Figure 3.3.5 High magnification images showing debonding at the Cu_6Sn_5 IMC layer / solder interface at two different regions after 500 cycles (a) Location near region 1 and (b) is the corresponding BE image. SEM image of region 3 is shown in (c) and its corresponding BE image in (d).

Micrographs shown in Figures 3.3.2, 3.3.3 and 3.3.4, depict the progression of interfacial debonding between Cu_6Sn_5 IMCs and Sn matrix with increased number of thermal cycles. High magnification SEM micrographs of these interfaces after 500 TMF cycles suggest that fractures occur in two different modes. In one case, Sn grains protrude over the surface of Cu_6Sn_5 IMCs by mode-II or mode-III type of fracture at their interface, while in other case cracks form in between solder and IMCs by mode-I type fracture and open up. It is important to note that there are no indications of plastic deformation in the Sn grains adjacent to these IMCs. These features can be observed in the micrographs presented in Figures 3.3.5. Such observations are indicative that the thermal stresses generated between the Cu_6Sn_5 IMC and the adjoining Sn grains could not be accommodated by deformation within the Sn grains prior to crack formation, unlike in *high temperature regime* TMF [19, 21, 42].

3.3.2 Effect of temperature regime of TMF on surface damage accumulation

In order to compare the effects of temperature regimes on the TMF behavior Sn-3.5wt%Ag solder joints, SEM images from published literature have been utilized in this section.

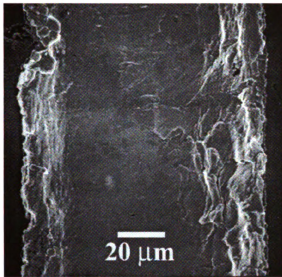
High temperature regime TMF between -15°C and 150°C , irrespective of whether the long dwell was at the high or low temperature extreme, causes intense microstructural damage within the solder region near the Cu_6Sn_5 layer present at the solder/substrate interface as shown in Figure 3.3.6. This type of

microstructural damage within the solder is completely absent in specimens subjected to the *low temperature regime* TMF between -55°C and 125°C .

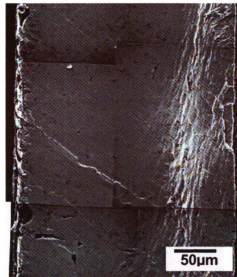
Surface damage features resulting from *high temperature regime* TMF are similar, irrespective of whether it was from TMF with long dwell at low temperature extreme (-15°C) or with long dwell at high temperature extreme (150°C). Under such conditions, microstructural damage is localized within the Sn matrix present at a region closer to the solder/substrate interface IMC layer (Figures 3.3.6 (a) and 3.3.6 (b)). Such damages resulting from *high temperature regime* TMF consists of surface manifestations of grain boundary sliding and/or relief, and grain-boundary decohesion, all of which associated with significant extents of plastic deformation within the Sn grains. Illustrations of these manifestations are presented in Figures 3.3.7. In Figure 3.3.7 (a), Sn grain boundary decohesion is observed at approximately one grain diameter away from the IMC layer and solder interface, while Figure 3.3.7 (b) presents surface damage due to grain boundary sliding and/or relief.

On the other hand, microstructural damage due to *low temperature regime* TMF is marked by the lack of observable plastic deformation within Sn grains. This is consistent with the observation reported by Rhee et.al. that mode of deformation and hence microstructural damage in Sn is strongly dependent on temperature [7]. As a consequence, at the low temperatures encountered in the present study absence of significant plastic deformation within the Sn grains plays an important role. The thermal stresses arising from TMF are basically

causing grain boundary debonding within Sn, and interfacial debonding between IMCs and Sn grains.



(a)



(b)

Figure 3.3.6 SEM images showing surface damage on Sn-3.5wt%Ag Solder joints after 1000 cycles of high temperature regime TMF with long dwell at (a) high temperature extreme, and (b) low temperature extreme. Adopted from Subramanian et.al. [21, 42].

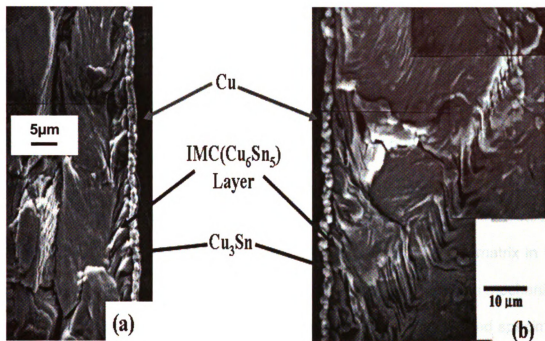


Figure 3.3.7 SEM images showing the effect of high temperature regime TMF on surface damage features near the IMC layer / solder interface, (a) Sn-Sn grain decohesion and (b) grain boundary sliding / relief and shear banding. Adopted from Choi et.al.[19].

3.3.3 Influence of temperature regime of TMF on the residual mechanical properties

Effect of *low temperature regime* TMF on the residual mechanical strength is shown in Figure 3.3.8. Residual shear strength of joints was found to drop rapidly by ~35% within first 100 cycles, and ~ 50% after 500 cycles, as compared to the initial shear strength.

This drastic decrease in the residual shear strength can be attributed to the appearance of cracks at the interface of IMC layer and solder matrix in the very early stages of TMF. Evidence of such interfacial debonding on mechanical properties comes from the fracture features in a mechanically sheared specimen as shown in Figures 3.3.9. The fracture path of this Sn-3.5wt%Ag solder joint, subjected to 500 cycles of TMF in the *low temperature regime*, seems to have initiated along the IMC layer and solder interface near the corner (region 3), and proceeds predominantly along the interface. Sn-Sn grain boundary decohesion observed in region 1 may cause some deviations of the crack path. This finding suggests that these interfacial cracks developed at interfaces during TMF cycles, had caused the failure to take place at those locations during mechanical testing. Since the imposition of thermal stresses arising from this *low temperature regime* TMF are not accommodated by plastic deformation, to a greater degree as compared to *high temperature regime* TMF, within Sn grains, relaxation of thermal stresses that one normally expects during dwell times [29, 30] at extreme temperatures may not be a contributing factor .

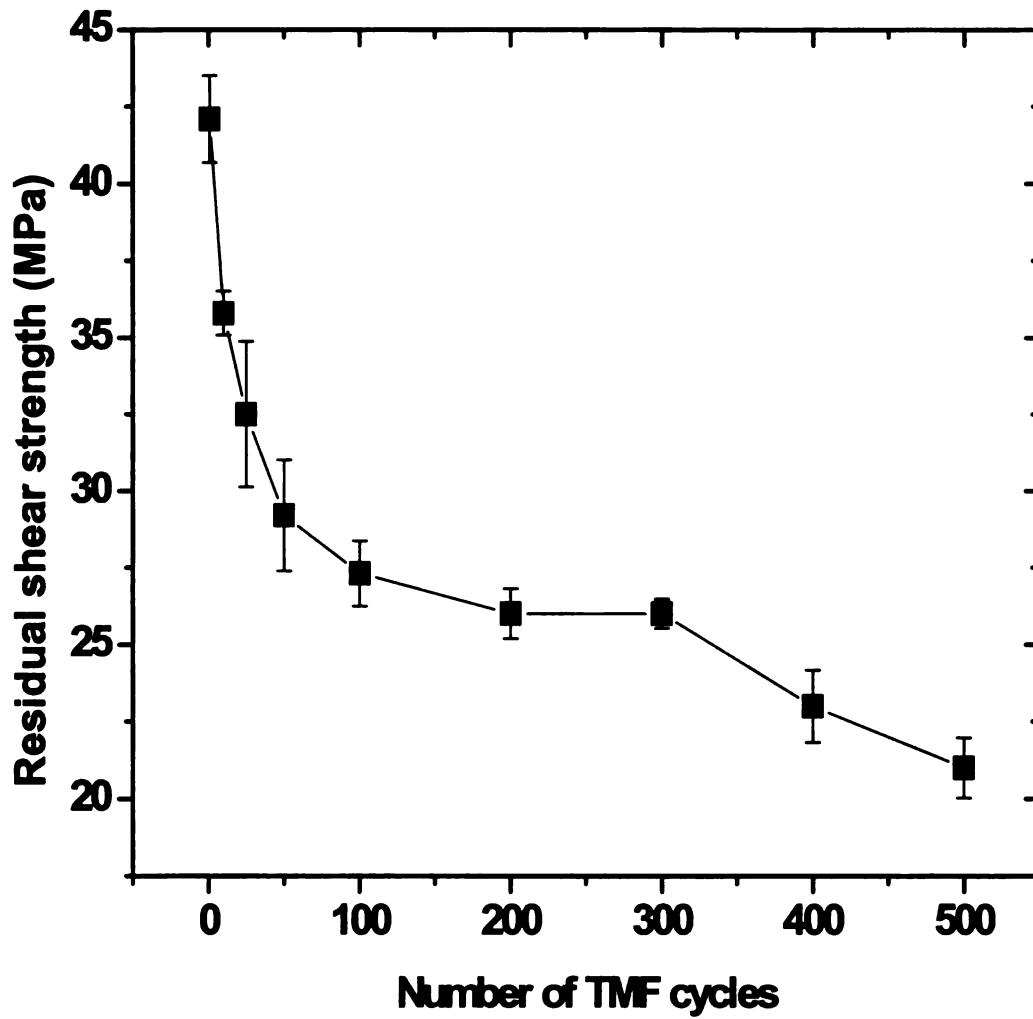


Figure 3.3.8 Plot showing the variation of residual shear stress of Sn-3.5wt%Ag solder joints as a function of TMF cycles. Error bars represent 95% confidence intervals.

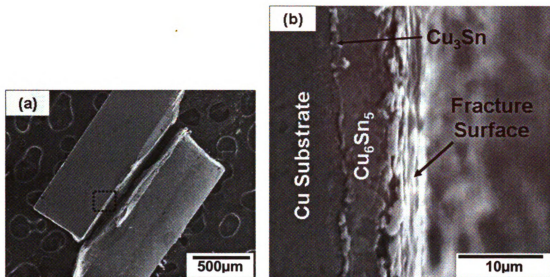


Figure 3.3.9 (a) Cross sectional view of a mechanically failed Sn-3.5wt%Ag solder joint;(b) Enlarged view on the of the region inside the dotted rectangle in (a). This joint had undergone 500 cycles of TMF prior to mechanical testing.

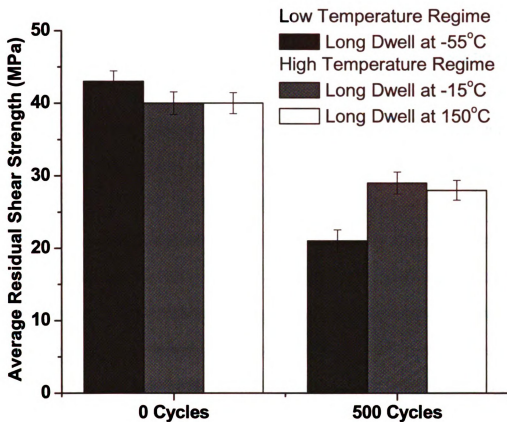


Figure 3.3.10 Plot comparing the effect of high and low temperature regime TMF on average shear strength of Sn-3.5wt%Ag single shear-lap solder joints after 500 cycles of TMF. Residual strength data used for comparison was obtained from [18, 21, 42].

Figure 3.3.10 compares effect of *low* and *high temperature regime* TMF on the residual strength of Sn-3.5wt%Ag solder joints after 500 cycles. This plot also shows the influence of other service parameters such as dwell times and heating rate on residual strength of solder joints subjected to *high temperature regime* TMF. Evidently, *low temperature regime* TMF has a more detrimental effect on the residual mechanical properties of solder joints as compared to *high temperature regime* TMF. These results, in conjunction with microstructural observations, suggest that interfacial and grain boundary fractures, with lack of significant observable plastic deformation (causing localized surface damage) within the Sn grains during low temperature TMF, may be the major contributing factors for the significant drop in strength under such conditions. Under these circumstances cracks continue to form and propagate with each successive cycle of TMF. Hence, residual strength does not seem to stabilize even after 500 cycles of low temperature TMF. This is in contrast with findings of *high temperature regime* TMF studies, whereas residual mechanical properties seem to stabilize after 250 TMF cycles [21, 42].

3.4 Conclusions

The following summarizes the effect of *low temperature regime* (-55°C and 125°C) TMF on eutectic Sn-3.5wt%Ag solder joints.

1. Surface damage is mainly in the form of debonding between Cu_6Sn_5 IMCs and solder, and with some Sn grain boundary fractures, without any

observable plastic deformation within the Sn grains. Such minimal plastic deformation results in localized surface damage within the solder matrix. These observations are completely different from those noted due to *high temperature regime* (-15 °C and 150 °C) TMF. Such conditions result in grain boundary events with extensive plastic deformation within Sn grains at regions close C₆Sn₅ IMC layer.

2. Residual mechanical properties continued to drop drastically during the early stages of *low temperature regime* TMF, without stabilizing even after 500 cycles, whereas in *high temperature regime* TMF residual shear strength of solder joints stabilize after 250 cycles. In addition, magnitude of the loss in mechanical shear strength is much greater for low temperature TMF.

Chapter 4

Low temperature regime thermomechanical fatigue behavior of nano-structured polyhedral oligomeric silsesquioxanes reinforced Sn-based solder joints

Rationale and objectives

Thermomechanical fatigue (TMF) experienced by Sn-based solder joints during service adversely affects their mechanical reliability. Deterioration in the mechanical strength of such joints occurs primarily due to interfacial damage. However, the mode of interfacial damage depends on the temperature regimes within which solder joints are subjected to TMF. *High temperature regime* TMF causes Sn-Sn grain boundary (GB) events such as GB sliding / decohesion, while intermetallic compound – solder interfacial decohesion results during *low temperature regime* TMF. Consequently, to improve the mechanical reliability of Sn-based joints, enhanced bonding of the aforementioned boundaries / interfaces must be realized. The nanostructured chemical polyhedral oligomeric silsesquioxanes (POSS) with surface active silanol (Si-OH) groups are known to form thermodynamically feasible bonds with the solder matrix. As a result, POSS presents a viable solution towards improving the mechanical reliability of Sn-based solder joints experiencing TMF. This study explores such a possibility by subjecting trisilanol POSS reinforced solder joints to low temperature regime TMF, followed by mechanical and microstructural characterizations of such joints.

4.1. Background

In microelectronic applications solder joints are required to experience cycling between temperature extremes [20, 21, 42, 55]. In Sn-based solder joints, thermal cycling causes anisotropic strains between the micro-constituents (Sn grains, intermetallic compounds (IMC) and substrate) resulting in thermomechanical fatigue (TMF) of those joints [18, 20, 21, 23, 42, 55]. Damage occurring as a consequence of TMF deteriorates the mechanical reliability of solder joints [20, 21, 42, 55]. This has motivated the development of several strategies to improve material properties for enhancing solder service performance. For that purpose the commonly used approaches are composite solders and alloying. The former involves incorporation of reinforcements into the solder matrix, while the later requires minor element additions to base Sn-Ag or Sn-Ag-Cu alloys. In the present state, both the techniques result in the formation of IMCs within the solder matrix, which tend to coarsen during service (section 1.3). Additionally, depending on the type and availability of the reinforcements / elemental additions there could be either processing or economic implications.

The latest methodology for improving service reliability of Sn-based solders involve incorporation of nano-structured, surface active and non-coarsening reinforcement polyhedral oligomeric silsesquioxanes (POSS) to the solder matrix [55]. POSS consists of a thermally stable inorganic core made up of Si and O framework ($\text{SiO}_{1.5}$) [55]. Study carried out by Lee et.al. have shown that POSS with surface active silanol (Si-OH)) groups have the ability to bond

with the Sn matrix and does not agglomerate during the reflow process [55]. TMF studies between -15°C and 150°C revealed that surface damage has been greatly reduced upon addition of POSS to eutectic Sn-3.5wt%Ag solder joints. This suggested that Sn grain boundary events, responsible for deteriorating mechanical reliability, was diminished upon POSS reinforcement [2, 18, 55]. However, the influence of POSS reinforcement on the lower temperature regime TMF behavior of Sn-based solder joints is yet to be ascertained. Studies presented in chapter 3 have indicated that Cu_6Sn_5 layer-solder decohesion resulting from *lower temperature regime* TMF between -55°C and 125°C . That kind of damage had a more detrimental effect on solder joint mechanical reliability than *higher temperature regime* TMF (-15°C and 150°C). Consequently, this study investigates the influence of POSS reinforcements to Sn-based solder joints subjected to *lower temperature regime* TMF between -55°C and 125°C

4.2. Experimental details

Materials used in this study were commercially available eutectic Sn-3.5Ag (SA) and Sn-3.0wt%Ag-0.5wt%Cu (SAC305) solder pastes, and nano-structured chemical Iso-Butyl POSS trisilanol POSS was obtained from Hybrid Plastics®. 2wt% of Iso-Butyl trisilanol POSS was then mechanically mixed with SA and SAC305 solder paste to prepare two additional pastes of composition SA

+ Iso-Butyl trisilanol (SA2iB), and SAC305 +2wt% Iso-Butyl trisilanol (SAC2iB). Finally, single shear lap solder joints (Figure 2.2.1 (b)) were prepared using the four solder pastes, i.e. SA, SA2iB, SAC305, and SAC2iB. Details of specimen preparation have been provided in chapter 2.

To conduct TMF studies solder joints were thermally cycled from -55°C to 125°C using a bench top model of MicroClimate[®] test chambers by Cincinnati Sub-Zero with a programmable controller. Test specimens were placed in the environmental chamber that was initially at -55°C . It is then heated with an average rate of 3.9°C per minute to 125°C , and held at this temperature for 10 minutes. Following this high temperature dwell, specimens were cooled to -55°C with an average cooling rate of about 2.4°C per minute. The dwell time at -55°C was set for 45 minutes. This thermal profile was cycled during TMF testing. The programmed and the actually measured temperature profiles experienced by specimens have been presented in chapters 2 and 3.

Microstructural characterization was carried out using a Scanning Electron Microscope (SEM). For this purpose, representative solder joints were metallographically polished on one side, prior to placing them in the environmental chamber. These specimens were taken out of the chamber at periodic intervals and the resultant surface damage was documented using SEM. Mechanical characterization was carried out using a mechanical solids analyzer

(RSA-III) by TA Instruments[®]. Batches of solder joints prepared with types of pastes, which were thermally cycled for 1, 10, 100, 200, 300, 400, and 500 TMF cycles, were strained to failure for this mechanical characterization at 25 °C with a simple shear strain rate of 10^{-3} s^{-1} at 25 °C. Eight to ten specimens were used to study each condition so that the results obtained provide realistic trends. Fractured surfaces of the mechanically tested specimens were examined to obtain the actual joint area that contributed to the strength of the joint. This methodology has been described in chapter 2.

4.3 Results and discussion

4.3.1 Influence of POSS reinforcements on the residual mechanical behavior of Sn-based solder joints

Figures 4.3.1 plots the residual mechanical strength as a function of number of TMF cycles imposed on Sn-based solder joints with and without POSS reinforcement. Figures 4.3.1(a), and 4.3.1(b) show the effects of such reinforcement on residual mechanical behavior eutectic SA, and SAC305 solder joints respectively.

Regardless of the composition, all solder joints experience drop in their residual strength within 100 cycles of TMF. However, reinforced solder joints experiences a lesser drop than their corresponding control SA and SAC305 solder joints. After 100 cycles, effects of POSS reinforcement on the residual mechanical behavior of solder joints become markedly prominent. Nano-composite (SA2iB and SAC2iB) solder joints retain higher residual strength after

100 cycles as compared to their controls. Moreover, the residual strength of nano-composite solder joints stabilizes after 100 cycles of TMF, while that of SA and SAC305 drops significantly after 500 cycles. Statistical analysis supporting this observation has been provided in Table 4.1-4.2. Trends comparing the effects of POSS reinforcement on the average residual shear strengths of SA and SAC305 solder joints have been presented in Figures 4.3.1(c) and 4.3.1(d) respectively. These trends were determined through second-order non-linear least square analysis. Equation used for this purpose is of the form,

$$y(N) = y_n + \sum_{i=1}^2 A_i \exp\left(-\frac{N}{t_i}\right) \quad (1)$$

where, $y(N)$ is the residual strength after N cycles of TMF, " y_n " corresponds to residual strength after 1000cycles, while " t_i " and " A_i " are fitting constants. Exponential fit was chosen because residual strength shows an initial drop followed by stabilization with progression of TMF cycles. Such a behavior is indicative of specimens undergoing fatigue [39].

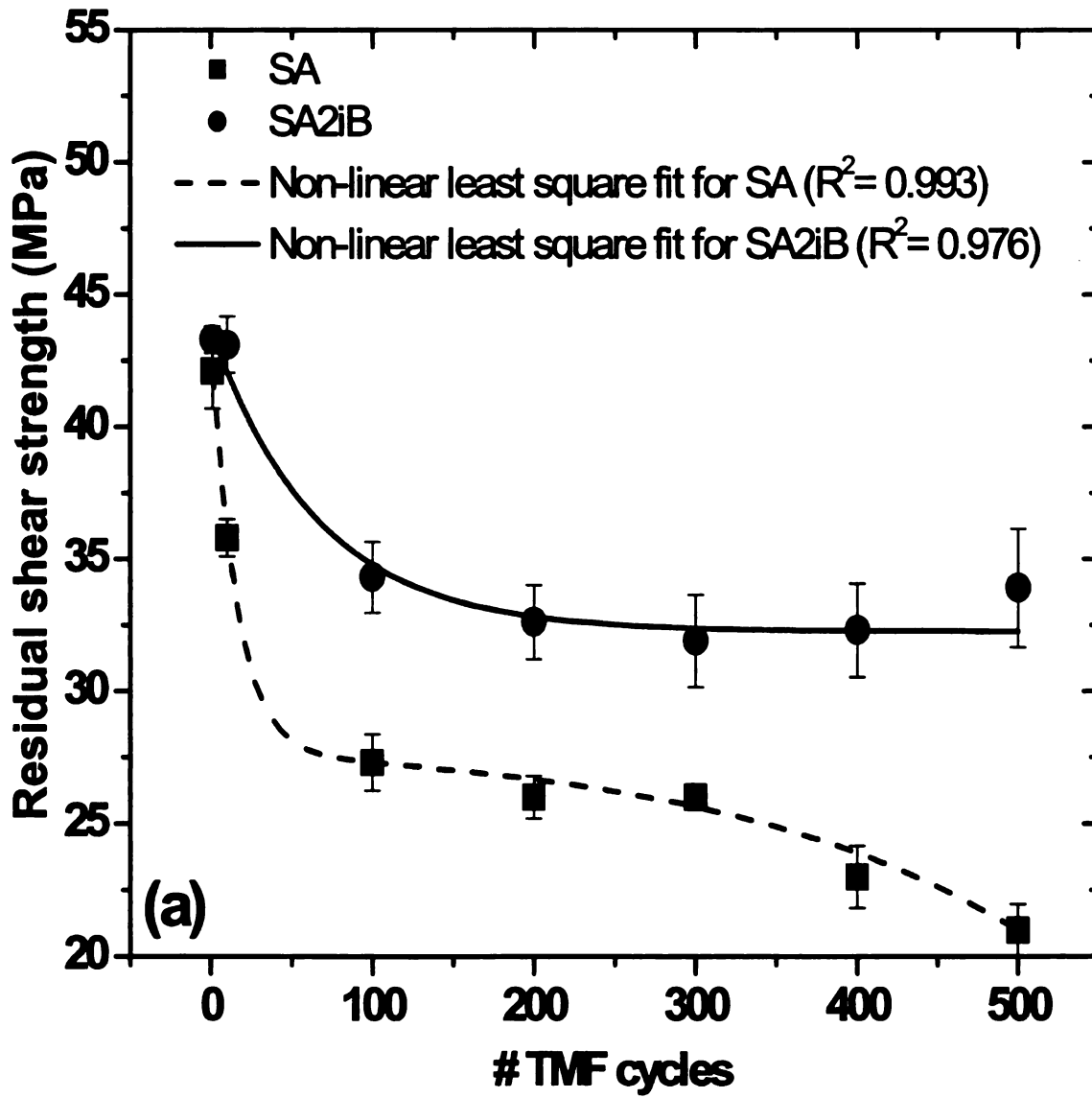


Figure 4.3.1 (a) Comparison of residual shear strengths of (a) SA and SA2iB
 Error bars show 95% confidence intervals. Second order exponential non-linear
 least square fits have also been shown

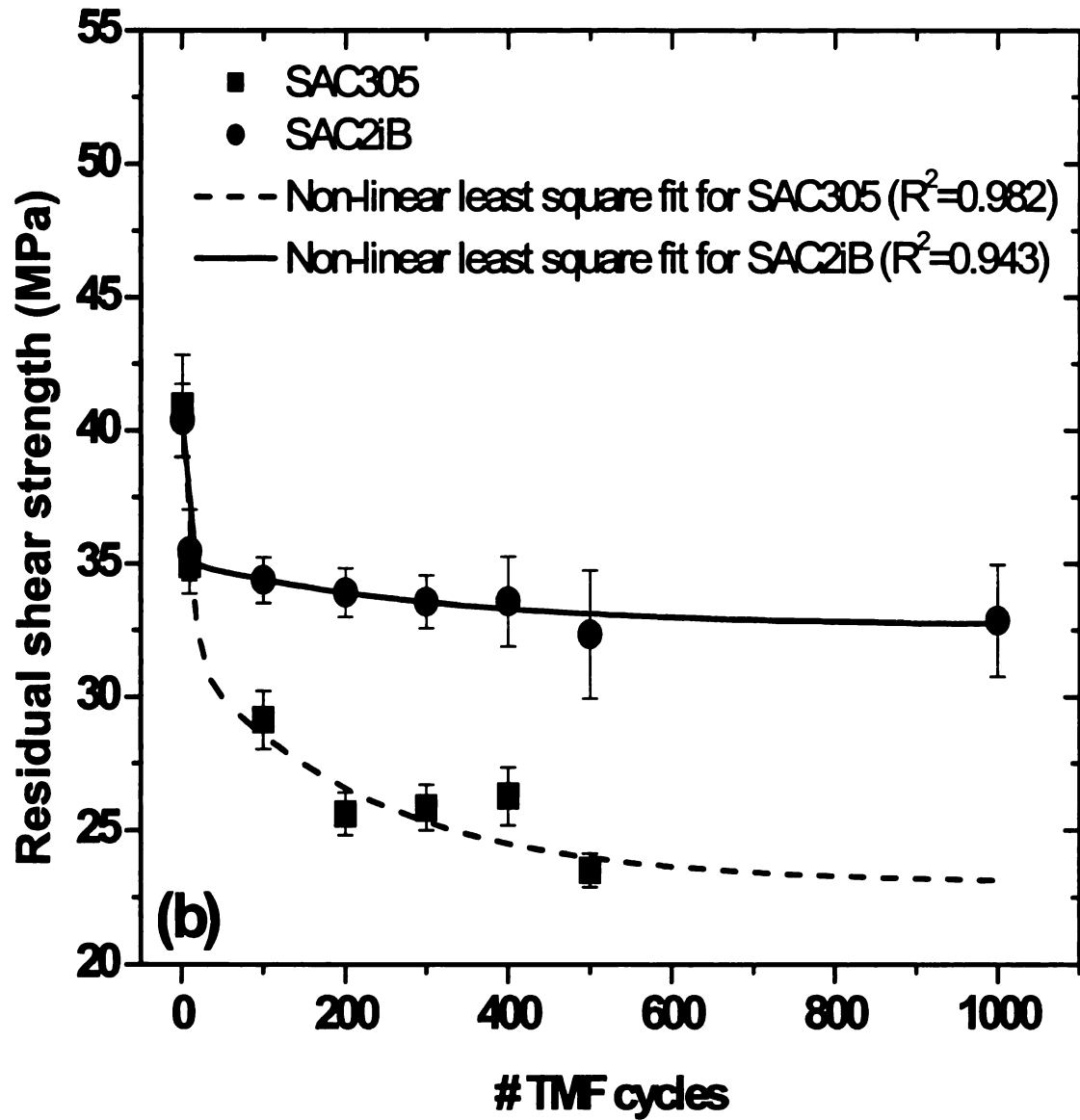


Figure 4.3.1 (b) Comparison of residual shear strengths of SAC305 and SAC2iB solder joints. Error bars show 95% confidence intervals. Second order exponential non-linear least square fits have also been shown.

Table 4.1 Statistical analysis of residual mechanical behavior of SA, and SA2iB solder joints (Figure 4.3.1 (a)). Single tail t-test is used for this purpose. Analysis is carried out on the basis of p values. This is evaluated by comparing residual mechanical strength data of two chosen cycles. If there is a difference in the residual strength at the chosen number of cycles, then the p value is less than 0.05, otherwise the two chosen data sets are not statistically different. In this analysis, residual strength data for 100 cycles is compared with 400 and 500 cycles.

Number of TMF cycles	p values	
	SA	SA2iB
400	0.1554	0.3337
500	6.4786×10^{-4}	0.8766

The analysis shows that in case of SA2iB there is no statistically significant difference between residual strength measured after 100 and 500 cycles. However, residual strength for SA drops after 500 cycles TMF as compared to 100 cycles.

Table 4.2 Statistical analysis of residual mechanical behavior of SAC305, and SAC2iB solder joints (Figure 4.3.1). Methodology for analysis is exactly the same as described in Tables 4.1. In this analysis, residual strength data after 100 cycles is compared with 400 and 500 cycles for both the types of specimens and additional 1000 cycles for SAC2iB..

Number of TMF cycles	p values	
	SAC305	SAC2iB
400	0.1213	0.6313
500	0.002	0.123
1000	-	0.223

The analysis shows that in case of SAC2iB there is no statistically significant difference between residual strength measured after 100, 500 and 1000 cycles. However, residual strength for SAC305 drops after 500 cycles TMF as compared to 100 cycles.

Results from mechanical characterization demonstrate that POSS trisilanol reinforcement improves the residual mechanical behavior of both SA and SAC305 solder joints within the number of TMF cycles chosen for this study. Such an improvement indicates that POSS reinforcements retard the microstructural damages responsible for the deterioration in the mechanical strength of control joints. Studies characterizing the effects of POSS reinforcement on the microstructural damage due to low temperature regime TMF have been presented in the following section.

4.3.2 Microstructural features contributing to the low temperature behavior of POSS reinforced solder joints

This section compares the effects low temperature regime TMF on the microstructural damage in both nano-composite and unreinforced solder joints. Based on this comparison, microstructure - residual mechanical strength relationship is established.

SEM images presented in Figures 4.3.2(a)-(c), Figures 4.3.3(a)-(c), Figures 4.3.4(a)-(c), and Figures 4.3.5(a)-(c) shows the surface damage evolution after 0, 100 , and 500 cycles in SA, SA2iB, SAC305, and SAC2iB representative solder joints respectively. After 100 TMF cycles, surface damage is evident in all the specimens. This corresponds to the observed drop in the mechanical strength after 100 cycles in both nano-composite and control solder joints (Figures 4.3.1). However, as noted earlier, after 100 TMF cycles nano-composite solder joints have a higher residual strength, and that subsequent thermal cycling does not have any effect on their residual strength.

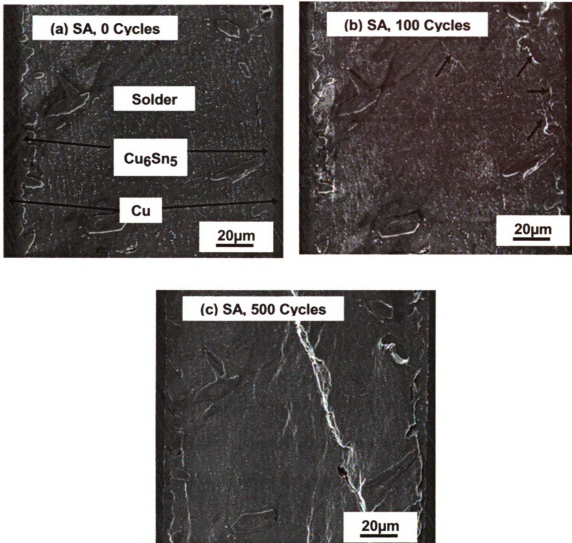


Figure 4.3.2 SEM images showing surface damage evolution in eutectic Sn-3.5Ag (SA) solder joint due to low temperature regime TMF between $-55^{\circ}C$ to $125^{\circ}C$. Surface damages after 100 cycles of TMF has been indicated with arrows.



Figure 4.3.3 SEM images showing surface damage evolution in SA + 2wt% Iso-Butyl trisilanol (SA2iB) solder joint due to low temperature regime TMF between -55°C to 125°C . Surface damages after 100 cycles of TMF has been indicate with arrows.

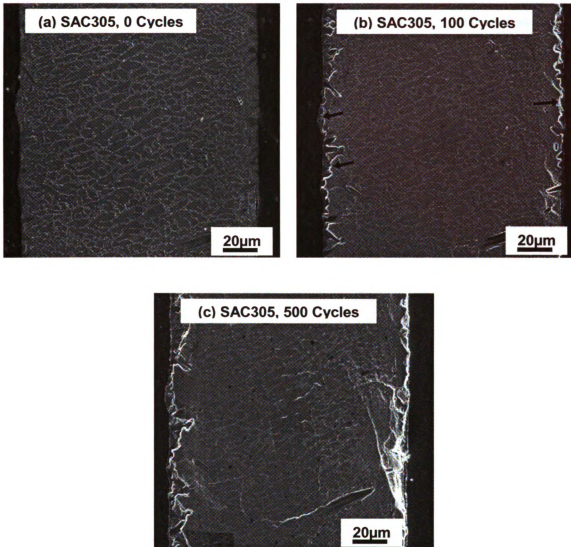


Figure 4.3.4 SEM images showing surface damage evolution in Sn-3.0wt%Ag-0.5wt%Cu (SAC305) solder joint due to low temperature regime TMF between -55°C to 125°C . Surface damages after 100 cycles of TMF has been indicate with arrows.

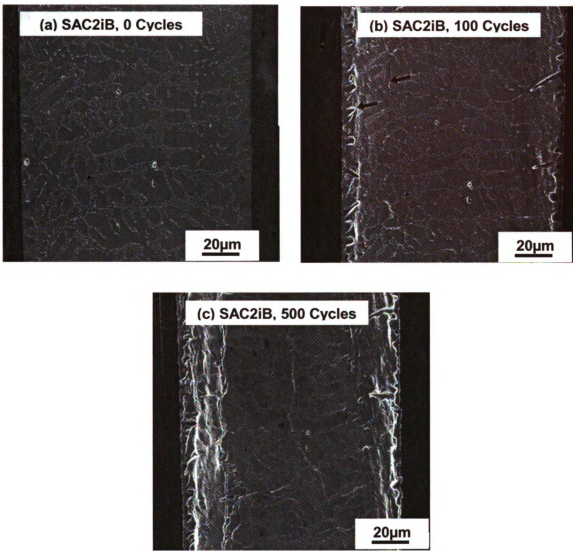


Figure 4.3.5 SEM images showing surface damage evolution in SAC305+2wt% Iso-Butyl trisilanol (SAC2iB) solder joint due to low temperature regime TMF between -55°C to 125°C . Surface damages after 100 cycles of TMF has been indicate with arrows.

This suggests that POSS reinforcements alter the damage mechanisms operative during low temperature regime TMF.

Figures 4.3.2 and 4.3.4 show that damages within the solder region of control specimens appear to be localized in nature, suggesting the inability of the solder matrix to accommodate anisotropic strains generated during TMF through plastic deformation of the solder matrix. In comparison, POSS reinforced joints appear to experience significantly more damage in the solder region (Figure 4.3.3, and 4.3.5). To further elucidate the effects of POSS reinforcements, high magnification SEM images of the solder region after 500 cycles of TMF have been presented in Figures 4.3.6. It is apparent from the SEM images that nano-composite solder joints have accumulated significantly more damage than the control joints. Such extensive damage within the solder region suggests that POSS reinforcements effectively disperse damage over a larger volume. In other words, solder matrix in nano-composite solder joints can effectively accommodate such anisotropic strains through plastic deformation of the solder matrix. Thereby, diminishing the detrimental effects of TMF cycles on the mechanical strength of nano-composite solder joints, and possibly contributing to the stabilizing of residual mechanical strength after 100 cycles.

The second type of surface manifestation observed in control joints are that of Cu_6Sn_5 layer / Sn interfacial decohesion. SEM images of SA (Figure 4.3.2(c)) and SAC305 (Figure 4.3.4(c)) after 500 TMF cycles show such interfacial damage. As mentioned earlier, low temperature regime TMF studies on SA joints (chapter 3) have shown that Cu_6Sn_5 layer / Sn interfacial damage

significantly contributes to the deterioration in the residual mechanical strength of such joints. Consequently, it becomes important to assess the influence of POSS reinforcement on the Cu_6Sn_5 layer / solder interface during low temperature regime TMF. SEM images (Figure 4.3.3(b)-(c), and Figures 4.3.5(b)-(c)) of POSS reinforced solder joints incur damage mainly within the solder region near the Cu_6Sn_5 IMC layer / solder interface. However, such images do not show the finer microstructural details required for comparison. Consequently high magnification SEM images of the Cu_6Sn_5 / solder interfacial region have been presented in Figures 4.3.7. Figures 4.3.7(a)-(b) show the effects of low temperature regime TMF on Cu_6Sn_5 layer / solder interface SA and SAC305 solder joints respectively after 500 cycles. Cu_6Sn_5 layer – solder interfacial decohesion is apparent in both types of joints, indicating the vulnerability of such interfaces during low temperature regime TMF. However, a very different damage feature results upon reinforcing with POSS. High magnification images presented in Figures 4.3.7(c)-(d) reveal cracks running parallel to the Cu_6Sn_5 IMC layer, with significant surface damages (unlike control specimens) within the solder region of both SA2iB (Figure 4.3.7(c)), and SAC2iB (Figure 4.3.7(d)). Additionally, there seems to be minimal cracking at the Cu_6Sn_5 layer – solder interface.

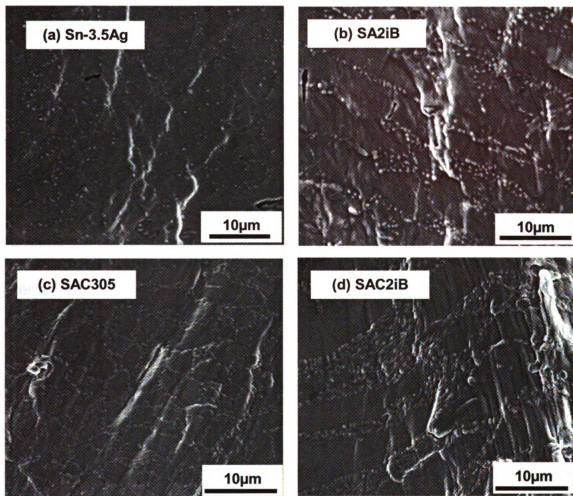


Figure 4.3.6 High magnification SEM images comparing the effects of low temperature regime TMF on surfaces damages within the solder region after 500 cycles. Nano-composite (SA2iB and SAC2iB) solder joints show significant damages within the solder region as compared to Sn-based solder (SA and SAC305) joints.

Such observations suggest that anisotropic strains due to TMF are accommodated by the solder region through plastic deformation in nano-composite solder joints (Figures 4.3.7(c)-(d)), while Cu_6Sn_5 layer / solder interfacial decohesion is responsible for such accommodation in control specimens (Figures 4.3.7(a)-(b)). Furthermore, such accommodations in nano-composite joint can only occur if there is a strong bonding between Cu_6Sn_5 and surrounding solder matrix. In other words, POSS improves Cu_6Sn_5 / Sn interfacial bonding in addition to reinforcing the solder matrix. Further evidence of improved Cu_6Sn_5 / Sn interfacial bonding due to POSS additions have been presented in Figures 4.3.8. These high magnification SEM images show the influence of low temperature regime TMF on Cu_6Sn_5 particle (within solder region) / Sn interface in SA (Figure 4.3.8(a)) and nano-composite SA2iB solder joints (Figure 4.3.8(b)) after 500 cycles. Interfacial decohesion between Cu_6Sn_5 and solder matrix is apparent in SA. However in case of SA2iB, shear bands along with cracks are observed within the solder region, even though there seems to be few cracks present at the Cu_6Sn_5 particle – solder interface. Shear bands in SA2iB suggests that the neighboring solder region undergoes considerable plastic deformation due to the imposed anisotropic strains. Similar shear banding has also been observed within the solder region of SAC2iB near the Cu_6Sn_5 / Sn interface (Figure 4.3.9). It may also be noted that such

improved Cu_6Sn_5 – Sn interfacial bonding also alludes to the presence of POSS nano-particles at those interfaces. Nonetheless, enhanced bonding between Cu_6Sn_5 layer and solder matrix will contribute to the higher residual strength demonstrated by POSS reinforced solder joints (Figures 4.3.1).

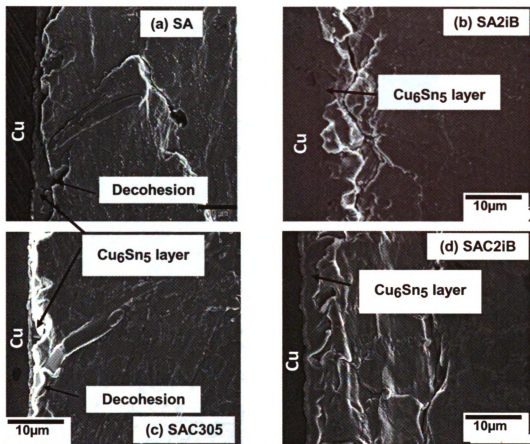


Figure 4.3.7 High magnification SEM images comparing the effects of low temperature regime TMF on the Cu_6Sn_5 layer – solder interfacial regions in Sn-based and nano-composite solder joints. Cu_6Sn_5 layer – solder decohesion is evident in both SA and SAC305, while damage is primarily located within the solder region in SA2iB and SAC2iB. Scale bar indicates $10\mu\text{m}$.

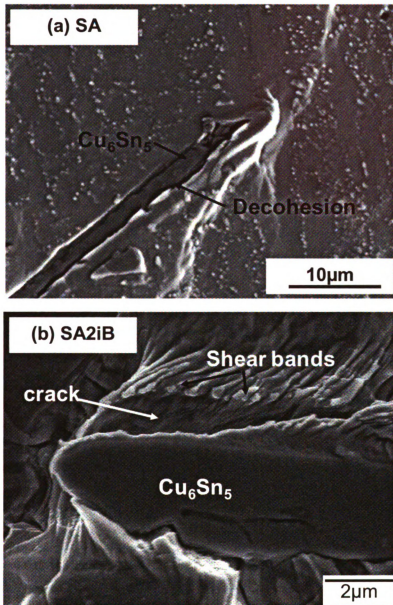


Figure 4.3.8 High magnification SEM images comparing Cu_6Sn_5 particle – solder interfaces in SA and nano-composite SA2iB after 500 cycles of low temperature regime TMF. Interfacial decohesion is evident in SA while shear bands within the solder matrix near the Cu_6Sn_5 – solder interface is observed in SA2iB.

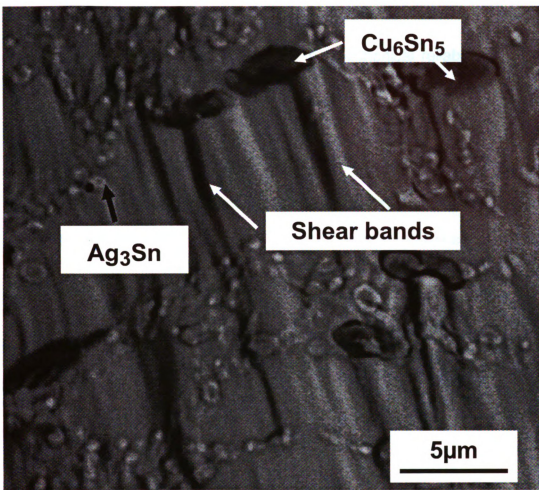


Figure 4.3.9 BE image of SAC2iB showing shear bands within the solder region near the Cu_6Sn_5 – solder interface.

4.4. Conclusions

Trisilanol POSS reinforcements improve the mechanical reliability of Sn-based solder joints experiencing low temperature regime TMF. Such improvements result due to:

1. Dispersion of damage within the solder region over a larger volume and thereby facilitating the solder joints to effectively accommodate anisotropic strains generated during TMF. Such damage dispersion causes plastic deformation of the solder matrix.
2. Improvement of Cu_6Sn_5 layer / solder interfacial bonding. This further suggests the presence of POSS particles at such interfaces.

Chapter 5

Influence of polyhedral oligomeric silsesquioxane additions on Sn-Ag-Cu bulk specimens

Rationale and objectives

Polyhedral oligomeric silsesquioxanes (POSS) improves mechanical reliability of Sn-based solder joints by pinning Sn-Sn grain boundaries, and improving Cu₆Sn₅ layer – Sn interfacial bonding. This suggests that POSS additions may influence the microstructure of Sn-based solders. However, due to the small volume of the solder region (in a joint configuration), additional effects of POSS additions on the microstructure may not be detected. Furthermore, additional input of Cu within the solder region, due the utilization of Cu substrates, may further hinder in any assessment of such effects. Consequently, effect of POSS on bulk solder is investigated. This study was carried out through the microstructural observation and thermal analysis.

5.1. Background

Reinforcing Sn-based solder with nanostructured polyhedral oligomeric silsesquioxanes (POSS) with surface active silanol (Si-OH) groups has been shown to retard Sn grain boundary events [55]. Furthermore, results presented in chapter 4 indicate improved intermetallic compound (IMC) Cu_6Sn_5 layer / solder interfacial bonding upon reinforcing with POSS trisilanols. Additionally, such reinforcements also increased the load bearing capacity of the solder matrix by accommodating stresses generated during thermomechanical fatigue (TMF) (chapter 4). These studies suggest that POSS (with Si-OH groups) are present within the solder matrix and also at the Sn-Sn and Cu_6Sn_5 / Sn interfaces. This further suggests that POSS may have segregated at those interfaces during solidification. Such a behavior has been classically observed during minor elements additions to alloy systems [1, 32]. However, in majority of the systems, minor elements form secondary / tertiary phases, which are then found at the grain boundaries and within the matrix. For example, adding minor concentrations of Ni to Sn-Ag-Cu results in the formation of $(\text{Cu Ni})_6\text{Sn}_5$ IMC, which pins not only Sn-grain boundaries but also are found within the solder matrix [1, 32]. The difference between such minor element additions and nanostructured POSS trisilanols is that the former results in an easily observable secondary / tertiary phase within the microstructure, while the later does not. Average diameter of POSS with Si-OH is 1.5nm, and after bonding with the matrix, does not coarsen during service [55]. Consequently, it is rather difficult to

observe POSS within the solder microstructure. This necessitates other methods for indirectly confirming the presence of POSS within the solder. Furthermore, such methods should avoid the geometric constraints posed by the substrates used in a solder joint.

Studies, thus far, were carried out on POSS reinforced Sn-based solder joints were prepared with Cu substrates. Dimensions of those joints were approximately 1mm x 1mm x 0.1mm (chapter 2) [1, 20, 21, 25, 32, 42, 55]. Microstructure of a typical joint consists of approximately 3-5 μm thick (12-20 vol%) interfacial Cu_6Sn_5 layer. Further, chapter 4 showed that POSS may prefer to be present at the Cu_6Sn_5 layer / Sn interface, which has a total interfacial area of $\sim 2 \text{ mm}^2$ (considering both sides of the joint). So it is expected that significant fraction of POSS additions may be present at those interfaces. This means additional effects resulting from the interaction of that fraction of POSS with the Sn-based solder may not be detected. As a result it is necessary to study the influence of POSS additions on bulk specimens.

Additionally, Cu substrates, used in joint fabrication, also increase the Cu concentration within the solder region of the joint by 0.5-0.8 wt% [8, 63]. This is evident from the presence of Cu_6Sn_5 particles within the solder region of the Sn-3.5wt%Ag joints (Figures 3.3.1). Any addition of POSS will definitely result in its segregation at the Cu_6Sn_5 particles / Sn interface. This could be a very likely situation for Sn-Ag-Cu solders, which has gained significant popularity in recent

years [7, 8, 10, 12, 15, 48, 50, 64]. Hence studies on observing the additional effects of POSS should incorporate this fact for a more realistic assessment.

In view of the above mentioned considerations bulk Sn-3.0wt%Ag-0.5wt%Cu (SAC305) have been chosen for this study. Influence of POSS additions to SAC305 has been investigated through analysis of microstructure and differential scanning calorimeter (DSC) thermograms.

5.2. Experimental details

POSS added solder pastes were prepared by mechanically mixing 2wt% nano-structured POSS chemicals to commercially available Sn-3.0wt%Ag-0.5%Cu (SAC305) solder paste. Two varieties of POSS were used in this study (i) Iso-Butyl trisilanol POSS and, (ii) Iso-Butyl Octa POSS. Compositions of the POSS containing specimens were SAC305 + 2wt% Iso-Butyl trisilanol POSS, and SAC305 + 2wt% Iso-Butyl Octa POSS. It is to be noted that trisilanol POSS is an open cage structure consisting of three surface active silanol (Si-OH) groups (Figure 5.2.1 (a)), whereas Octa POSS is a closed caged structure with no Si-OH groups attached (Figure 5.2.1 (b)). Procedural details of POSS addition to solder paste have been provided in chapter 2.

Bulk solder specimens were prepared by first heating solder pastes (placed in aluminum cups) at 280 °C to evaporate the flux in the paste. The resulting melt was then solidified by placing the aluminum cups on surfaces maintained at two different temperatures for obtaining different cooling rates. Faster cooling rate of 53 °C/min was achieved by placing the melt on a

perforated brass block maintained at room temperature, while cooling at a slower rate, i.e $16^{\circ}\text{C}/\text{min}$, was carried out solidifying the melt on hot plate maintained at 100°C . Figures 5.2.2 shows the measured temperature profiles for cooling at room temperature and at 100°C . These measurements were carried out by inserting a K-type thermocouple (with resolution $\pm 2.2^{\circ}\text{C}$) inside the molten solder. Mass of "button shaped" specimens obtained after solidification was ~ 6 grams (Figures 5.2.3).

Microstructural characterization was carried out using secondary electron and optical microscopes. Optical microscope observations are based on two types of views which have been described in Figures 5.2.2. The planar view is the flat face which was closest to the cooling surface, while the cross-sectional view is obtained by cutting the button shaped specimen perpendicular to the planar view. Polishing techniques used for microstructural observation have been described in chapter 2. For quantitative analysis of the optical micrographs, ImageJ© software was used.

Thermal analysis was performed using Mettler Toledo DSC-1® with mechanical inter-cooler in sealed crucible. For this purpose bulk specimens were rolled into thin sheets and small strips (weighing $15\text{ mg} \pm 0.1$) were cut from such sheets. The small strips were then encapsulated in aluminum pans and were placed inside DSC-1 for thermal analyses.

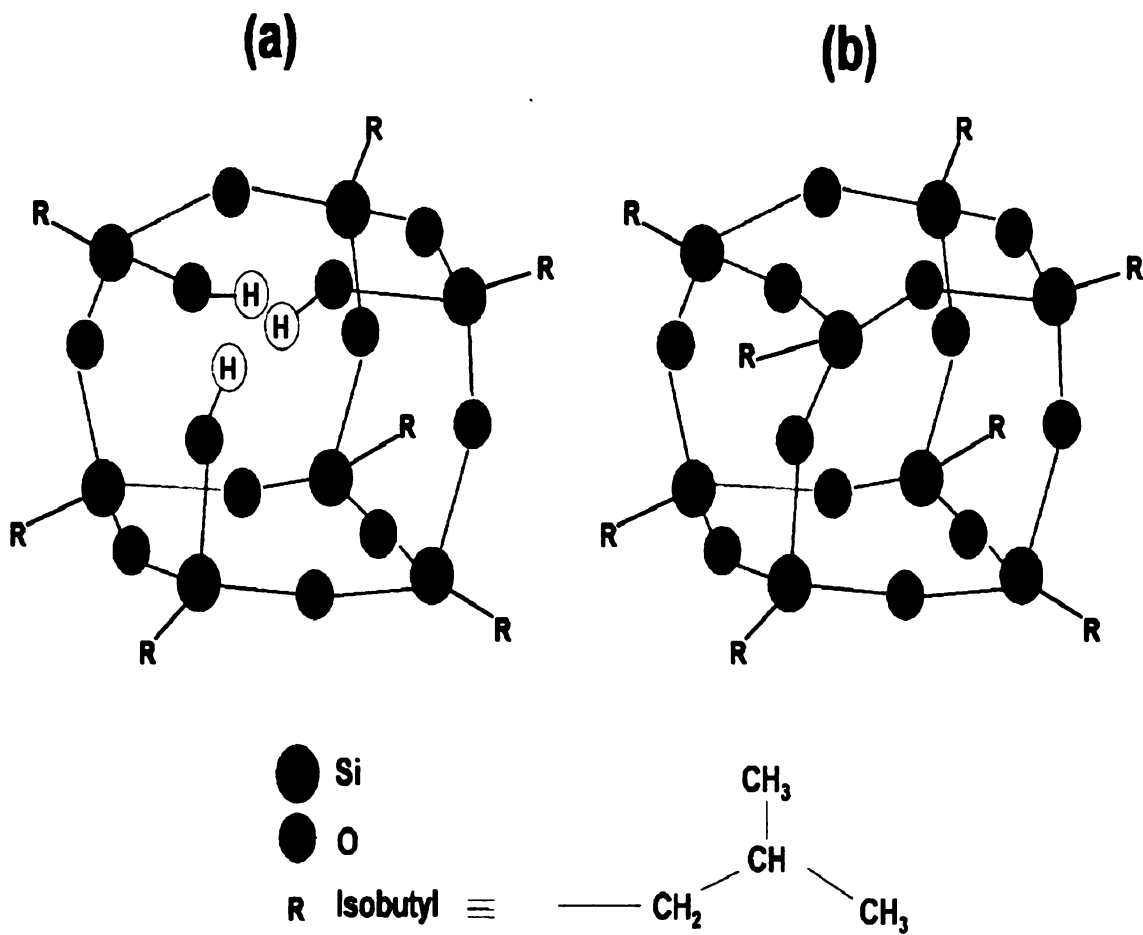


Figure 5.2.1 Schematic showing two different types POSS anatomies (a) Iso-Butyl Trisilanol POSS with three Si-OH groups, (b) Iso-Butyl Octa POSS without any Si-OH groups. Chemical formula for organic Iso-Butyl(R) group has also been shown.

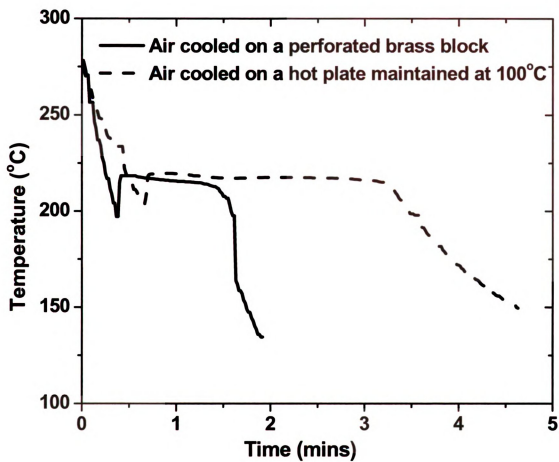


Figure 5.2.2 Comparison of cooling rates utilized for solidifying molten bulk solder specimens. Solid line indicates the faster cooling rate at $53^{\circ}\text{C}/\text{min}$, while the dashed line indicates slower cooling at a rate of $16^{\circ}\text{C}/\text{min}$.

3D view of as-cast bulk specimen

Planar (polished) view : surface in contact with hot plate

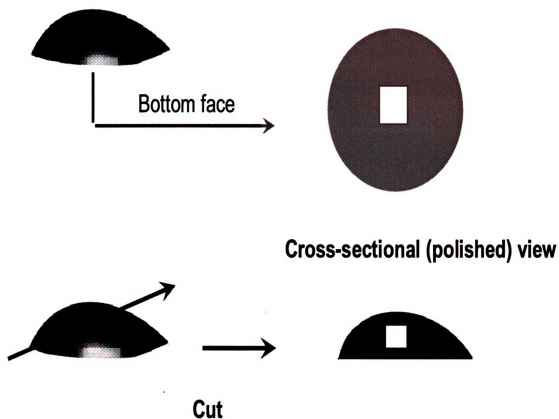


Figure 5.2.3 Left hand side showing the 3D views of the "button" shaped as-solidified bulk specimens. The right hand side shows the regions observed for microstructural characterization. The square boxes at the center of each view i.e. planar and cross-sectional, are the locations from where images for analysis were acquired.

5.3. Results and discussions

This section presents results from microstructural observations and thermal analysis. On the basis of those results, effects of POSS additions on bulk SAC305 specimens have been discussed.

5.3.2 Influence of POSS additions on the microstructure of Sn-3.0wt%Ag-0.5wt%Cu

Optical micrographs (planar view) comparing the effects of 2wt% trisilanol and Octa POSS additions on the bulk microstructure of SAC305 have been presented in Figures 5.3.1. Specimens shown in these micrographs were cooled at 53° C/min during solidification. It is observed that Iso-Butyl trisilanol POSS addition refines the as-solidified microstructure, whereas the Iso-Butyl Octa POSS addition does not produce any observable changes. The differences in the microstructure suggest that silanol (Si-OH) groups attached to the POSS cage interacts with the solder.

Further, trisilanol POSS addition results in a smaller sized dendritic arms (Figure 5.3.1 (b)), whereas, large dendritic arms are observed in the control (SAC305) and Octa POSS added specimens (Figures 5.3.1 (a), 5.3.1 (c)). Quantitative microstructural analysis carried out by measuring the secondary dendrite arm spacing (SDAS) further substantiates the microstructural refinement brought about by trisilanol POSS addition (Figure 5.3.2). SDAS measurement is directly related to the number of dendritic arms shooting out of a primary dendrite during solidification. If there are more secondary and tertiary arms present, then

SDAS will decrease, since more number of dendritic arms has to be accommodated within a given space/volume.

Further evidence of microstructural refinement in trisilanol POSS added specimens have been presented in optical micrographs of cross-sectional views in Figures 5.3.3. These images show the microstructures of SAC305, and SAC305 + 2wt% Iso-Butyl trisilanol POSS specimens solidified at two different cooling rates. Figures 5.3.5(a), and 5.3.3 (b) show the optical micrographs at a slow cooling rate ($16^{\circ}\text{C} / \text{min}$), while Figures 5.3.3 (c), and 5.3.3 (d) shows the optical micrographs at a faster cooling rate ($53^{\circ}\text{C} / \text{min}$). Large primary Sn dendritic arms are present in SAC305 specimens solidified at both fast and slow cooling rates (Figures 5.3.3 (a) and 5.3.3 (c)). However, primary Sn dendritic arms are barely noticeable in the microstructure of specimens containing Iso-Butyl trisilanol POSS (Figures 5.3.3 (b) and 5.3.3 (d)). These observations suggest the presence of highly branched dendritic structures within the microstructure. Schematic shown in Figures 5.3.4 elucidate the difference between a dendrite with fewer arms (extended dendrite) and a highly branched dendrite (equiaxed “condensed” dendrite). This study indicates that such equiaxed dendritic structure is present within the microstructure of specimens containing trisilanol POSS (Figures 5.3.3 (b), and 5.3.3 (d)). Similar dendritic structure has also been reported by Rappaz et.al in their study of Al-Si alloys inoculated with Ti [65]. Their observation was attributed to the presence of Ti, which promoted heterogeneous nucleation of primary Al. Such equiaxed

dendrites form when primary phase (Sn, in this study) dendrite has sufficient time to grow and form secondary and tertiary branches before the final solidification stage. Such an event can only occur when there is a reduction in undercooling required for solidifying the liquid melt [66]. A lower undercooling is indicative of the ease with which a primary phase nucleates from the melt. Consequently, following nucleation, Sn has more time to grow dendritic arms within the melt. Figures 5.3.5 compare the measured cooling curves of specimens containing different types of 2wt% POSS. Specimens containing iso-Butyl trisilanol POSS have lower undercooling as compared to the control (SAC305). In comparison, Octa POSS, as expected, did not alter the undercooling required to solidify SAC305. Furthermore, results presented thus far indicate that POSS with Si-OH groups (Iso-Butyl trisilanol POSS) are responsible for the heterogeneous nucleation of Sn during the solidification of SAC305 from liquid state.

Trisilanol POSS additions are also found to influence the morphology and size of IMC phases (Ag_3Sn and Cu_6Sn_5) present in microstructure of SAC305. Figure 5.3.6 (a) shows the backscattered electron image (BEI) ternary eutectic region in the as-solidified microstructure of SAC305, while Figure 5.3.6 (b) present the BEI of the ternary eutectic regions in SAC305 + Iso-Butyl trisilanol POSS. Specimens used for microstructural evaluation have been cooled at $53^\circ\text{C} / \text{min}$. In SAC305, large ($\sim 30\mu\text{m}$) rod and needle shaped Cu_6Sn_5 and Ag_3Sn IMCs are observed in the ternary eutectic region, while specimens containing trisilanol POSS show a refined ternary eutectic microstructure with

relatively spheroidal morphology. In general addition of trisilanol POSS results in a more uniform microstructure. This suggests that such addition influences the growth of IMCs within the liquid phase during solidification. According to Kingery, growth of secondary phases (IMCs) in a liquid phase involves two steps [67]. The first step involves movement of atoms through the melt to the IMC / liquid interface, while the next step required reaction between atoms at the interface [67]. In other words, growth of IMCs in liquid melt depends on the diffusivity of atoms through the liquid melt and IMC / liquid interfacial energy. Addition of POSS may affect both the parameters. Empirically, Trivedi et.al. showed that diffusivity (D) of the liquid melt is related to the SDAS (λ) through the following relationship [68, 69],

$$\lambda = K (D/v) \quad (1),$$

where, K , and v are constants and solidification velocity respectively [68]. According to Reed-Hill, v is related to undercooling (ΔT) as follows,

$$v = B \Delta T \quad (2),$$

where B is a constant of the order of 10^{-6} (m/s °C) [66]. Substituting for v in equation (1), and rearranging we have,

$$\lambda \Delta T = (K/B) D \quad (3).$$

Equation (3) suggests that D is directly proportional to the product $\lambda \Delta T$. Table 5.3.1 displays values of the product, $\lambda \Delta T$, for all the specimens studied.

Table 5.3.1 $\lambda \Delta T$ values for all specimens

Specimen	$\lambda \Delta T$
SAC305	233.1
SAC305 + 2wt% Iso-Butyl trisilanol POSS	17.7
SAC305 + 2wt% Iso-Butyl Octa POSS	337.5

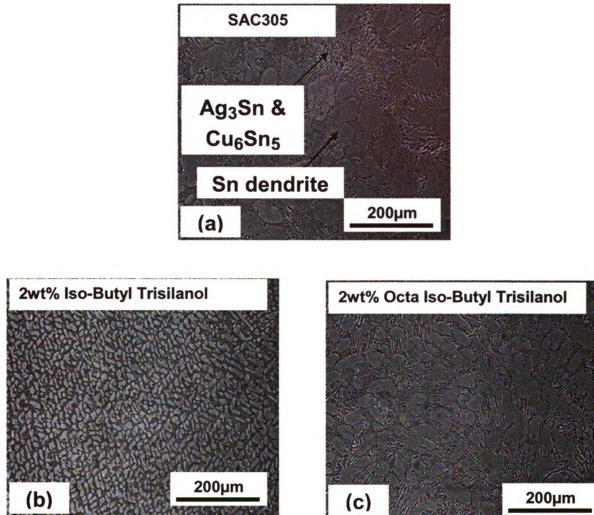


Figure 5.3.1 Optical micrographs showing the effects of 2wt% trisilanol POSS and Octa POSS additions on the as-solidified microstructures of SAC305. All the specimens have been cooled at 53 ° C /sec.

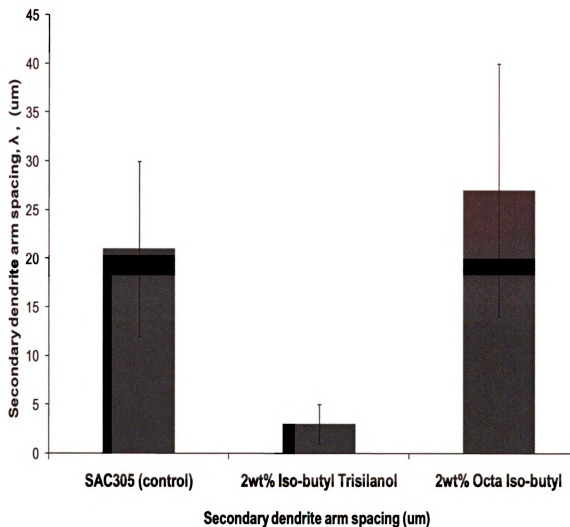
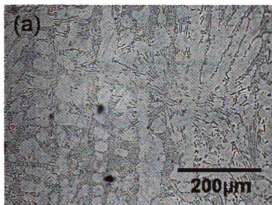
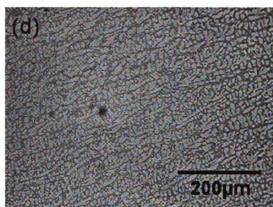
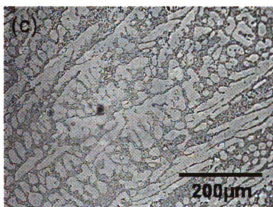
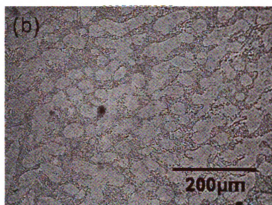


Figure 5.3.2 Plot showing the quantitative microstructural analysis of the secondary dendrite arm spacing.

Sn-3.0Ag-0.5Cu (SAC305)



SAC305 + 2wt% Iso-Butyl
Trisilanol



Figures 5.3.3 Optical micrographs of showing the effects of 2wt% Trisilanol POSS additions to SAC305 specimens cooled at (a)-(b) 16 °C/sec (slower cooling rate), and (c)-(d) 53 °C/sec (faster cooling rate).

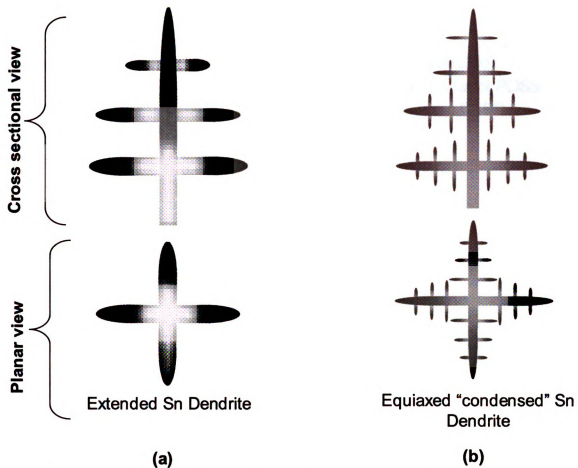


Figure 5.3.4 Schematic showing the dendritic morphologies of (a) SAC, and (b) after trisilanol POSS additions.

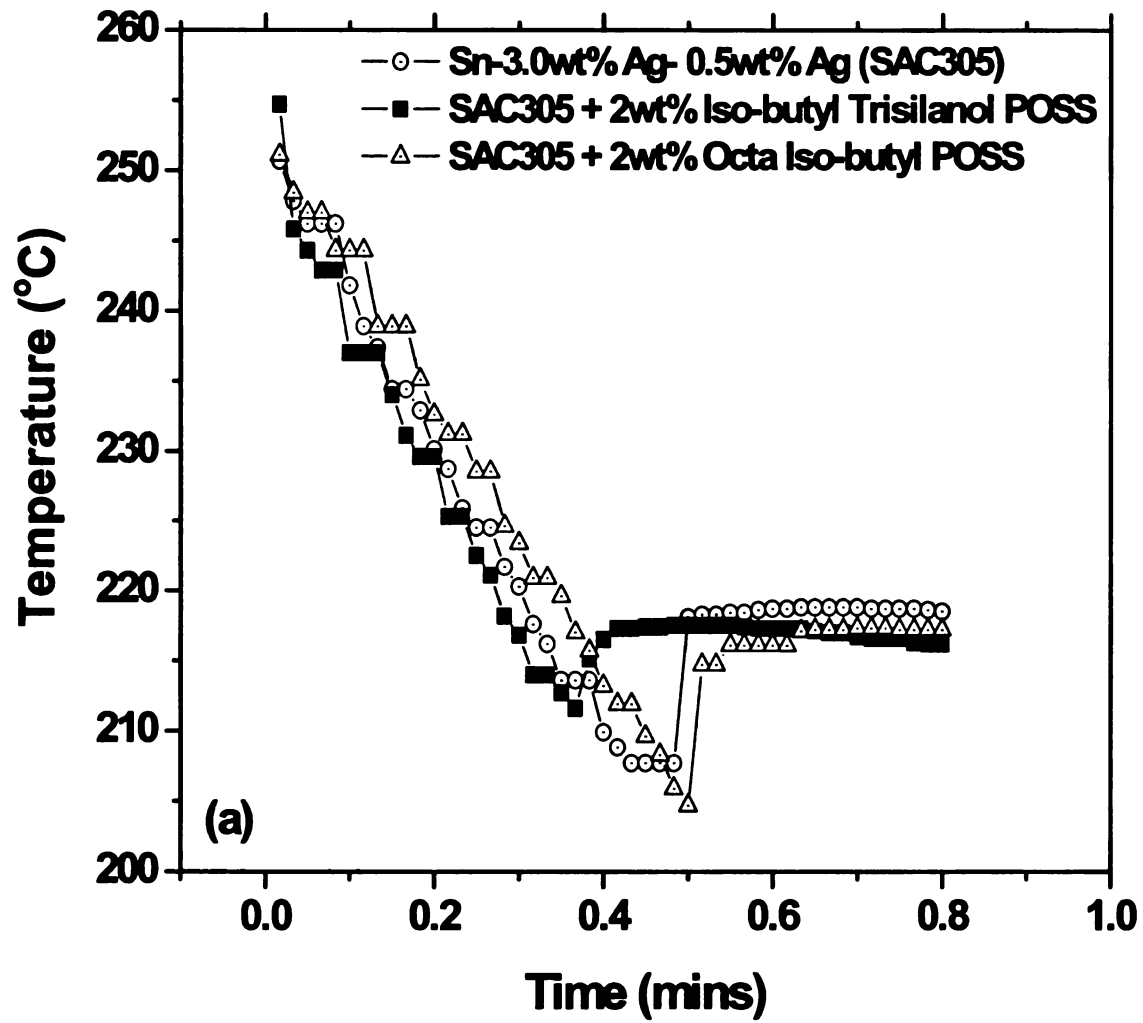


Figure 5.3.5 (a) Plots showing measured cooling curves of SAC305, SAC305 + 2wt% Iso-Butyl trisilanol POSS, and SAC305 + 2wt% Iso-Butyl Octa POSS.

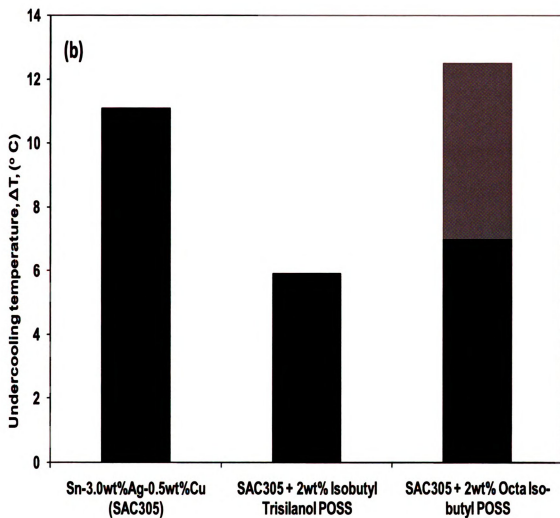


Figure 5.3.5 (a) Plots showing effects of trisilanol POSS and Octa POSS additions on undercooling. All the specimens were cooled at $53^{\circ}\text{C}/\text{sec}$.

Addition of trisilanol POSS reduces SDAS (Figure 5.3.2), and undercooling (Figure 5.3.5 (b)). Consequently, the listed values (table 5.3.1) show that $\lambda \Delta T$ in trisilanol POSS added SAC305 specimen is smaller by at least one order of magnitude than other specimens. In other words D decreases by at least one order of magnitude upon trisilanol POSS additions. This suggests that trisilanol POSS addition restricts diffusivity of atoms through the liquid melt.

Furthermore, prior studies on the TMF behavior of Sn-based solder joints have suggested that POSS may be present at the IMC/ solder interfaces. Consequently it is possible that such nano-particles may segregate themselves at $\text{Ag}_3\text{Sn} / \text{Sn}$ and $\text{Cu}_6\text{Sn}_5 / \text{Sn}$ interfaces during solidification. To validate this hypothesis SAC+2wt% Iso-Butyl trisilanol POSS specimen was isothermally aged at 100°C for 5 months in a parallel experiment. Optical micrographs showing the effects of such aging conditions are presented in Figures 5.3.7. Evidently, there is barely any noticeable change within the microstructure. Isothermal aging causes changes in size and morphology of secondary phases [70]. Driving force required for producing such changes is the necessity to decrease the interfacial energy of the system [70]. Consequently, the observed microstructural stability of trisilanol POSS added specimen strongly suggests their presence at $\text{Ag}_3\text{Sn} / \text{Sn}$ and $\text{Cu}_6\text{Sn}_5 / \text{Sn}$ interfaces and thereby decreasing the interfacial energy.

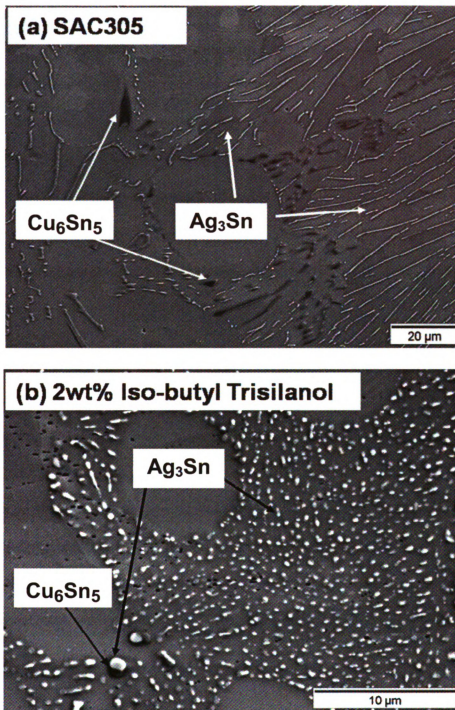


Figure 5.3.6 High magnification BEI showing sizes and morphology of Cu_6Sn_5 and Ag_3Sn IMCs in the ternary eutectic regions in (a) SAC305, and (b) SAC305 + 2wt% Iso-Butyl trisilanol POSS.

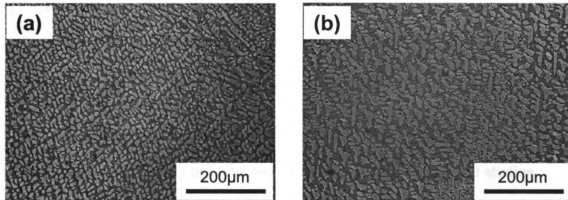


Figure 5.3.7 (a) Initial as-solidified microstructure of SAC305 + 2wt% Iso-Butyl trisilanol bulk specimen, (b) microstructure of the same specimen after isothermally aging at 100°C for 5 months.

In essence, these microstructural studies reveal that trisilanol POSS promotes heterogeneous nucleation of Sn and are present at the Sn / IMC (Ag_3Sn , and Cu_6Sn_5) interfaces. These observations further tend to suggest the presence of Si-O-metal bonds. However, presence of trisilanol POSS at the Sn grain boundaries could not be detected through these microstructural studies.

6.3.3 Thermal analysis

Thus far influences of POSS with Si-OH groups on the microstructure of SAC305 have been discussed. However, such influences on the microstructure occur due to Si-O-metal bonds, which are most likely to form in the molten liquid prior to solidification. Results investigating the interaction of Si-OH groups with SAC305 during melting are presented in this section. These studies are carried out with a DSC and employ two methods.

In the first method, effects of trisilanol POSS additions on the heat of fusion of bulk specimens are investigated. Two heating (melting) / cooling (solidification) cycles were performed at $10^\circ \text{C}/\text{min}$ and the second (last) heating cycle was considered for analysis. Specimens for this study were SAC305, and SAC305 + 2wt% Iso-Butyl trisilanol POSS. Typical DSC thermogram of the second (last) heating cycle are shown in Figure 5.3.8. Analysis of the thermograms was carried out by integrating the area within the peak. This area is the measure of heat of fusion (ΔH) required for melting. Table 5.3.2 lists ΔH for the two specimens. It is found that addition of trisilanol POSS increases the

ΔH , i.e. more energy is required for melting a give mass of SAC305 containing trisilanol POSS.

Several studies have indicated that melting initiates at the grain boundaries [71-73]. Hseih et.al. conclusively showed through *in-situ* transmission electron microscope studies of Al that melting initiates at the grain boundaries and triple junctions [73]. High ΔH of trisilanol POSS containing specimen suggests that melting does not occur easily as compared to control SAC305 specimens. This observation suggests that trisilanol POSS particles may be present at the Sn grain boundaries though the formation of Si-O-Sn bonds.

Table 5.3.2 Effects of trisilanol POSS additions on the heat of fusion of SAC305

Composition	$\Delta H(J/g)$
SAC305	62.7 \pm 0.16
SAC305 + 2wt% Iso-Butyl trisilanol POSS	66.3 \pm 0.17

To further confirm the presence of trisilanol POSS at the Sn grain boundaries, Kissinger's method of thermal analysis is utilized [74]. The main objective of Kissinger's analysis is to determine the activation energy of a first order transformation (such as melting). Activation energy is determined by measuring the variation of peak temperature (T_p) in DSC thermograms with heating rates (R) while maintaining the same cooling rate. Further, this analysis assumes that T_p corresponds to the maximum rate of transformation. Solid to

liquid transition in metals, during melting, is a first order transformation [74]. Such a transition results in peak / minima in a DSC thermogram (Figure 5.3.8). Consequently methodology described Kissinger can be utilized for studying the effect of trisilanol POSS on the melting behavior of SAC305.

The second set of thermal analysis is carried out by observing the peak melting temperature (minima of the peak shown in Figure 5.3.8) positions as a function of four different heating rates i.e. $10^{\circ}\text{C}/\text{min}$, $20^{\circ}\text{C}/\text{min}$, $30^{\circ}\text{C}/\text{min}$, and $40^{\circ}\text{C}/\text{min}$. A typical DSC thermogram showing the variation of peak melting temperature with heating rate has been presented in Figure 5.3.9. The plot of peak melting temperature (T_p) v.s. heating rate (R) is shown in Figures 5.3.10 for both SAC305 + 2wt% Iso-butyl trisilanol POSS and SAC305. These plots indicate that trisilanol POSS addition decreases the slope. Slope of the curves in Figure 5.3.10 may be related to the grain size. For a given weight, a specimen with smaller grains will have more number of Sn grain boundaries than the specimen with larger grains. Consequently there are more sites for melting to initiate and the melting process would be able to accommodate the heat supplied more efficiently. T_p of trisilanol POSS added SAC305 specimens show a lesser sensitivity to increase in R or smaller slope as compared to control SAC305. This suggests the presence of smaller Sn grains in trisilanol POSS containing specimen. BEI supporting the presence of smaller Sn grains have been in SAC305 + 2wt% Iso-Butyl trisilanol POSS have been shown in Figures 5.3.11.

Insensitivity of T_p vs. R slope for SAC305 + 2wt% Iso-Butyl trisilanol POSS further indicates that Si-OH in trisilanol POSS promotes heterogeneous nucleation of Sn. Further, activation energy (Q) of the melting process is determined from the equation [74]:

$$\ln (R / T_p^2) = - (Q / 8.314 T_p) + C \quad (1)$$

where C is a constant. Figure 5.3.10 (b) shows the plot of $\ln (R / T_p^2)$ v.s. $1/T_p$ for the all the specimens. Linear least square fit have been overlaid on the plot in Figure 5.3.10 (b). Table 5.3.3 shows the R^2 for the linear fit and activation energy for the melting process. Evidently specimens with trisilanol POSS have a higher Q than the control SAC305. These values further suggest that trisilanol POSS additions retard the initiation of melting at the Sn grain boundaries by being present at those boundaries.

Table 5.3.3 R^2 from linear least square fit and activation energy of melting resulting from Kissinger's analysis (Figure 5.3.10 (b))

Composition	R^2	Q (KJ/mol)
SAC305	0.971	628.7
SAC305 + 2wt% Iso-Butyl trisilanol POSS	0.983	1051.7

5.4. Summary

Addition of POSS with surface active Si-OH group causes microstructural refinement in Sn-3.0wt%-0.5wt%Ag. Factors contributing to such an effect are:

1. Promotion of heterogeneous nucleation of Sn by surface active Si-OH groups attached to trisilanol POSS cage, and thereby resulting in smaller Sn grains.
2. Presence of trisilanol POSS at Sn-Sn grain boundaries and IMC/Sn interfaces.

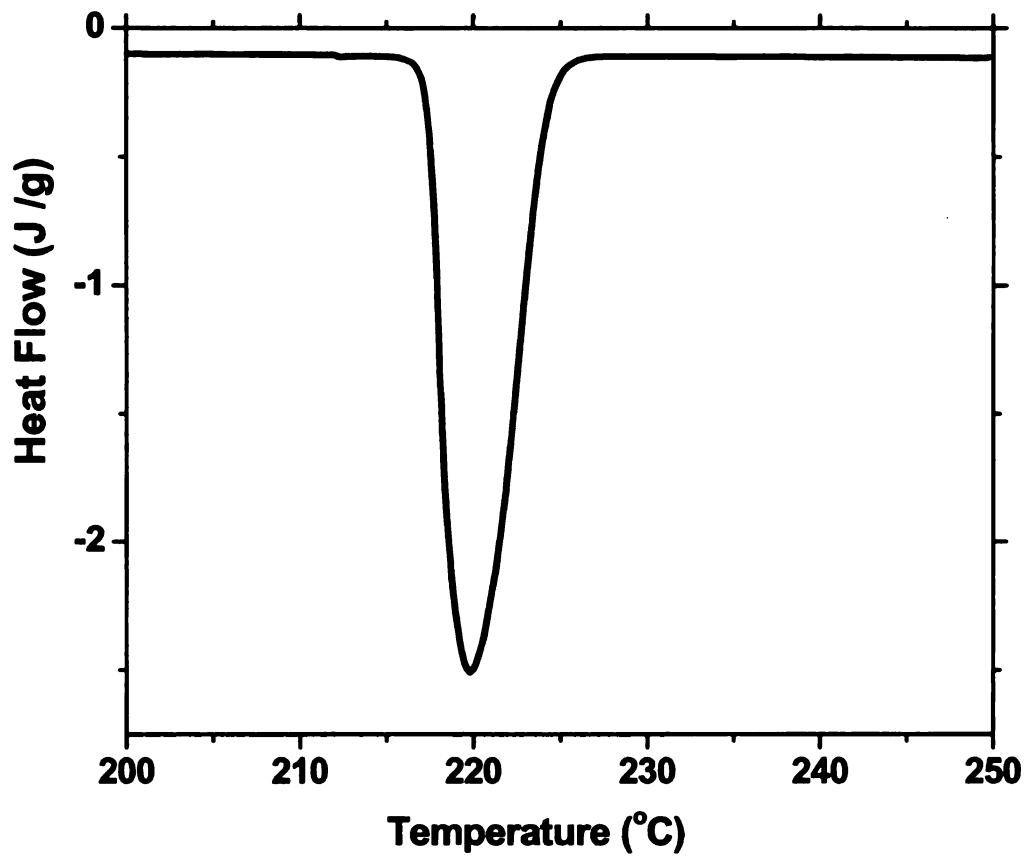


Figure 5.3.8 Typical DSC thermogram observed during melting. Area within the peak (minima) provides the heat of fusion. The negative y-axis represents endothermic heat input.

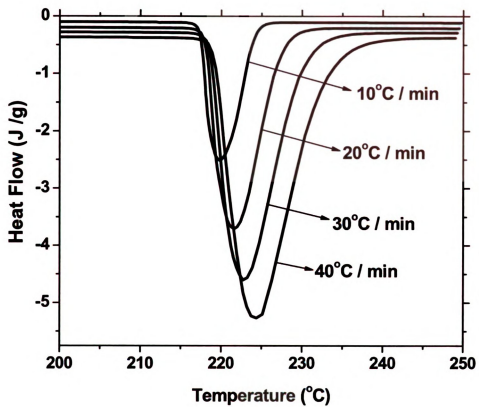


Figure 5.3.9 Typical DSC thermograms showing the increase in peak temperature T_p with increase in heating rate during melting. The negative y-axis represents endothermic heat input.

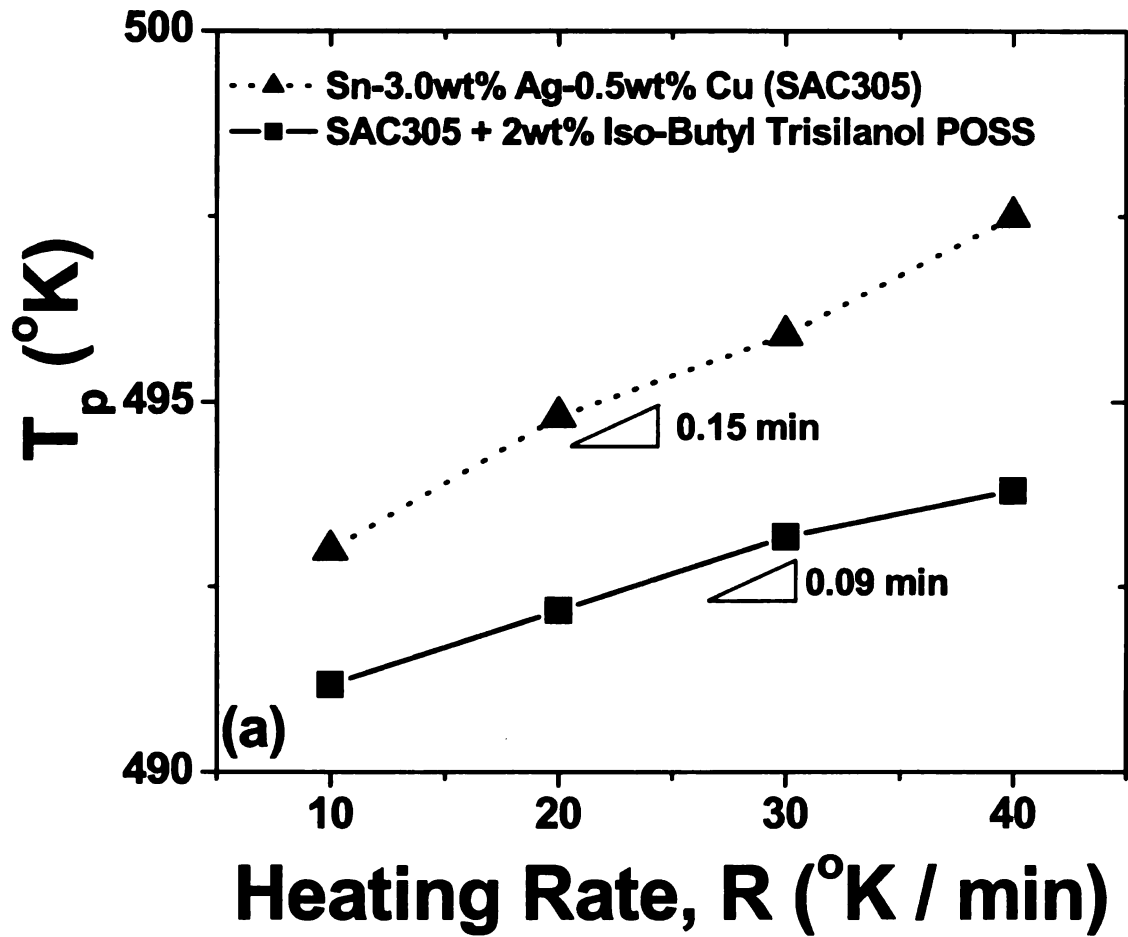


Figure 5.3.10 (a) Plots showing the effects of 2wt% trisilanol POSS additions on peak temperature vs. heating rate. Slopes in (a) were obtained by fitting a straight line.

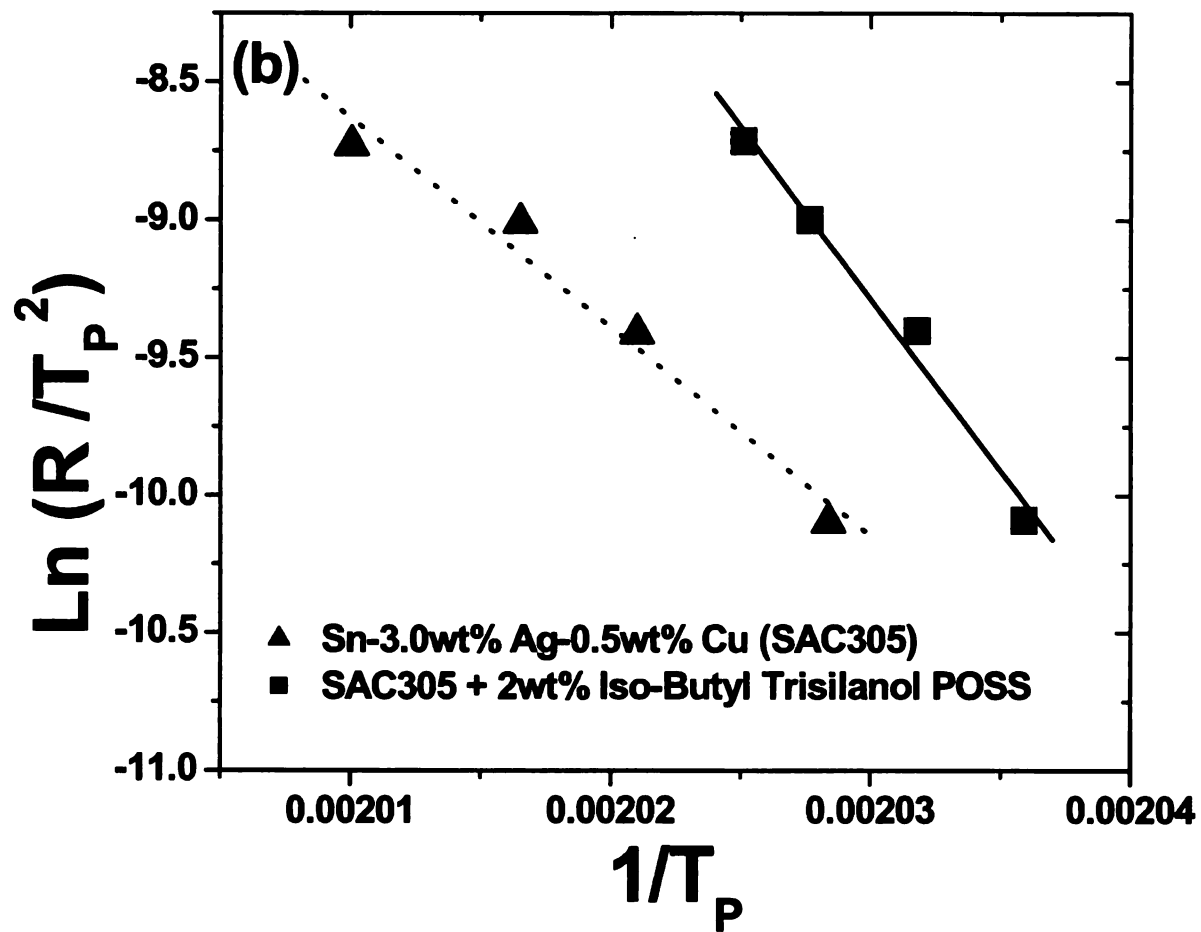


Figure 5.3.10 (b) Plots showing the effects of 2wt% trisilanol POSS additions on Arrhenius plot for melting. .

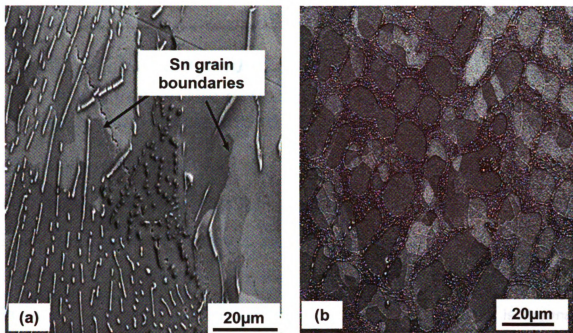


Figure 5.3.11 BEI comparing microstructures of (a) SAC305 and (b) SAC305 + 2wt% iso-Buty trisilanol POSS. POSS containing specimen show considerably more Sn grain boundaries than SAC305. Furthermore, size of Sn grains in (b) is less than 20µm.

Chapter 6

Influence of polyhedral oligomeric silsesquioxane additives on the coarsening kinetics of Ag_3Sn intermetallic compound in Sn-Ag-Cu solder joints

Rationale and objectives

Prior studies have shown that nanostructured trisilanol polyhedral oligomeric silsesquioxanes (POSS) with surface active Si-OH groups are present at the intermetallic compound (IMC) / Sn interfaces. Presence of trisilanol POSS at those interfaces resulted in minimal microstructural changes during isothermal aging. This suggests that trisilanol POSS nanostructures may enhance microstructural stability of solder joints by retarding coarsening of IMC particles in solder joints. As a result isothermal aging studies on solder joints have been carried out to investigate the influence of POSS additives on the coarsening kinetics of Ag_3Sn IMC phase. Although Sn-Ag-Cu contains both Ag_3Sn and Cu_6Sn_5 IMC phases, Ag_3Sn is chosen for this study because it coarsens considerably slower than Cu_6Sn_5 . This means monitoring gradual change in Ag_3Sn size can be easily carried out. Consequently, studying evolution of Ag_3Sn during isothermal aging provides a convenient method for investigating the effect of POSS with Si-OH on microstructural coarsening.

6.1. Background

Microstructural stability of intermetallic compounds (IMC) in Sn-based solder joints is an important service requirement. The main purpose of IMCs is to strengthen the solder matrix [32, 33]. Consequently service conditions leading to their coarsening will deteriorate their mechanical reliability. In automobile under-the-hood and power cycling applications service temperatures are in the neighborhood of 150 °C [1]. As a result, isothermal aging like conditions will exist for solder joints encountering high temperatures for long durations in service. Under such conditions IMCs will tend to coarsen. This has been shown to be true for Cu_6Sn_5 and Ag_3Sn IMCs in Sn-Ag-Cu solder joints experiencing thermal excursions [21, 34-36]. So to improve the service life of joints coarsening of IMCs must be retarded.

Results presented in chapter 5 showed that nanostructured polyhedral oligomeric silsesquioxanes (POSS) with surface active silanol (Si-OH) groups are present at the IMC / Sn interfaces. The presence of POSS at those interfaces was further shown to retard microstructural changes during isothermal aging. This means POSS with Si-OH (e.g. trisilanol POSS) have the capacity to retard coarsening of IMCs. Since coarsening involves movement of atomic species through different diffusion pathways (dislocation pipe diffusion, grain boundary diffusion etc.). POSS additions may influence the diffusion mechanism predominant during coarsening. In other words addition of POSS with Si-OH may affect the growth kinetics of IMC particles.

This chapter investigates such an influence of POSS. For this purpose coarsening behavior of Ag_3Sn is studied at different temperatures. Selection of Ag_3Sn is motivated by the fact that during isothermal aging Ag_3Sn grows considerable slower than Cu_6Sn_5 , consequently temporal changes in Ag_3Sn sizes would be easier to track [37, 38, 75]. Coarsening of Cu_6Sn_5 and Ag_3Sn in Sn based solders occurs by diffusion of Cu and Ag through Sn respectively [74]. Dyson showed that Cu diffuses significantly faster than Ag along “a” and “c” axes of Sn [37, 38]. This has been demonstrated through the listing of activation energy values in table 6.1 for both Cu and Ag. Furthermore, aging temperatures chosen for this study are between 80-180°C. This range considers the maximum temperature extremes that may be experienced by Sn-based solder joints during service.

Table 6.1 list of activation energies of diffusion of Ag and Cu along “a” and “c” axes of Sn

Diffusing species	Axes of Sn	Activation energy (KJ/mol)	Reference
Ag	a	77	[38]
	c	55	
Cu	a	33	[37]
	c	~16	

6.2. Experimental details

Materials used in this study were commercially available Sn-3.0wt%Ag-0.5wt%Cu (SAC305) solder paste, and Iso-Butyl POSS trisilanol POSS nano-structured chemical obtained from Hybrid Plastics®. 2wt% (10 vol%) of Iso-Butyl trisilanol POSS was then mechanically mixed with SAC305 solder paste to prepare additional pastes of composition SAC305 +2wt% Iso-Butyl Trisilanol (SAC2iB). Further, the two solder pastes, i.e. SAC305, and SAC2iB were used for preparing single shear lap solder joints (chapter 2). Details of specimen preparation have been provided in chapter 2. For microstructural observation, one side of the joint was metallurgically polished. First step of polishing involved, using SiC papers with grit sizes ranging from 800 to 2400. The final step consisted of polishing with 0.3 μ m alumina solution and 0.05 μ m colloidal silica solution. Isothermal aging was carried out in air circulated ovens which were maintained at 80°C, 90°C, 107°C, 120°C, 150°C, and 180°C. Temperature variation of these ovens was within $\pm 3^\circ\text{C}$. To observe the temporal evolution of microstructure, solder joints were taken out of their respective ovens after 0, 7, 14, 28, 42, and 56 days. Microstructural observation was carried out using JEOL 6400 scanning electron microscope (SEM) which has a resolution of 50nm. Prior to each observation, the polished side of every solder joint was re-polished following the final step of polishing outlined earlier. This procedure provided clarity to the SEM images required for determining sizes and distribution of Ag₃Sn particles. For evaluating the average Ag₃Sn particle diameter, images were taken randomly along the solder region of the joint, and over 150

measurements were made. Ag_3Sn particles are assumed to be spherical for measurement purposes. Software used for measuring particle size and statistical analysis were ImageJ[®] and Origin[®] respectively.

6.3 Results and discussion

6.3.1 Coarsening theories

Secondary phases in alloys grow in their dimensions during isothermal aging, during which larger particles grow at the expense of smaller particles. The driving force behind this process is the temporal reduction in interfacial area of the system, as it proceeds towards thermodynamic equilibrium [70]. Such a phenomenon is commonly known as coarsening or Ostwald ripening. As a consequence of reduction in interfacial area, mass transfer occurs from region of higher chemical potential to that of lower chemical potential. Mathematically, the flux of the species is given by Fick's 1st law in 3D,

$$\vec{J} = -M \vec{\nabla} \mu \quad (1)$$

where, J is the flux of the diffusing species, μ is chemical potential, and M is the phenomenological constant related to the diffusion coefficient. Further, chemical potential, μ , is given by ,

$$\mu = 2\Omega\gamma H \quad (2)$$

where, Ω is molar atomic volume, γ interfacial energy between the secondary phase and the surrounding matrix and H being the curvature of a particle. Evidently, diffusional flux of atoms occurs from regions of higher curvature (smaller particles with large interfacial area) to that of lower curvatures (larger

particles with smaller interfacial area). Consequently, the microstructure evolution results due to the growth of secondary phase particles with time.

In general growth kinetics of such particles is given by the equation,

$$\langle D \rangle^n - \langle D_0 \rangle^n = K t \quad (3)$$

where, $K = K_1 \exp(-Q/RT)$, $\langle D \rangle$ is the average diameter of the particle at a given time, t , $\langle D_0 \rangle$ initial average sizes, R is the gas constant, T is the temperature, Q is the activation energy of diffusion, and n is a phase size constant which is related to rate controlling mechanism responsible for coarsening of secondary phases.

Traditionally, theories of coarsening are based on lattice diffusion as the rate controlling mechanism, where the phase size constant n equals 3 [70, 76-78]. Following Senkov et.al, time variation of particle size is given by the equation,

$$\langle D \rangle^3 - \langle D_0 \rangle^3 = K_2 [(\gamma \Omega C_0 D_L) / RT] t$$

(4) where, K_2 is a constant, C_0 is the equilibrium solute concentration within the lattice, and D_L is coefficient of diffusion of solutes through the matrix. These theories assume that the particles are spherical and have small volume fractions within the matrix. In spite of these assumptions, several alloy systems have been known to follow equation 4 [70, 75, 79]. Typically lattice diffusion occurs at higher homologous temperatures (T/T_m) since the activation energy required for diffusion is higher. However, at lower temperatures diffusion of atoms occur

through different mechanisms which are also known as high diffusivity paths [80]. These paths are through grains boundaries, dislocation cores (pipe diffusion), and triple junction boundaries [77, 78, 80].

Several theoretical and experimental studies have been carried out to determine the growth kinetics of particles dominated by grain boundary diffusion. Phase size constant (n) for grain boundary diffusion equals 4. The general formulation for time variation of average particle size is as follows,

$$\langle D \rangle^4 - \langle D_0 \rangle^4 = K_3 [(w\gamma\Omega C_0^{gb} D_{gb})/RT]t \quad (5)$$

where, K_3 is a constant, w is the grain boundary width, C_0^{gb} is the equilibrium grain boundary concentration, and D_{gb} coefficient of diffusion along grain boundaries [78]. Equation 5 provides the temporal behavior of particle size due to diffusion along high angle grain boundaries [77]. Small angle grain boundaries have also been considered by Ardell as a possible path for diffusion [77]. In that theoretical treatment, low angle grain boundaries were composed of dislocations networks and secondary phase particles were embedded within such networks [77]. It was found that phases size exponent (n), under such conditions, equaled 5. Similar value of n was obtained by Senkov et.al. , however, in that study diffusion along grain boundary triple junctions were considered. Nonetheless, the general mathematical form is given as,

$$\langle D \rangle^5 - \langle D_0 \rangle^5 = K_4 [(q\gamma C_0^d D_d)/aRT] \quad (6)$$

where, K_4 is a constant, q is the cross-sectional area of an individual dislocation,

C_0^d is the equilibrium concentration of solutes within dislocation cores or at triple junction, D_d is the coefficient of diffusion along a dislocation, cores or triple junctions and 'a' the average diameter where $\langle D \rangle \gg a$.

Coarsening is also known to be controlled by the transfer of solutes across the particle-matrix interface [78]. Here the temporal behavior of particle growth is given by,

$$\langle D \rangle^2 - \langle D_0 \rangle^2 = K_5 [(\gamma \Omega C_0) / RT] \quad (7).$$

Symbol used in equation (7) have already been defined in equation (4). It may also be noted that coefficient of diffusion is absent in Eq. (7) suggesting that growth of particles are not diffusion controlled. Finally, Table 6.2 summarizes the different mechanisms known to control coarsening of secondary phase particles.

Table 6.2 Summary of mechanisms controlling coarsening of secondary phase particles and the respective phase size exponents

Phase size exponent, n	Rate controlling mechanism
2	Transfer of solutes across the particle / matrix interface
3	Lattice diffusion
4	Diffusion along grain boundaries
5	Triple junction diffusion , dislocation diffusion

6.3.2 Influence of POSS addition on Ag₃Sn particle size evolution

Typical BEI of the initial microstructure (prior to isothermal aging) in SAC305 and SAC2iB solder joints are shown in Figures 6.3.1(a) and 6.3.1(b) respectively. These micrographs show different phases present within the initial microstructure. The brighter phase is that of Ag₃Sn. High magnification SEM images presented in Figures 6.3.2(c) and 6.3.2(d) shows the initial size and morphology of Ag₃Sn IMC particles in SAC305 and SAC2iB respectively. Figure 6.3.2 shows the distribution of initial average diameters ($\langle D_0 \rangle$) of Ag₃Sn particle for both types of solder joints. t-test shows that there is no statistical significant difference (two-tail p values equals 0.54) between the Ag₃Sn particle diameters in the SAC305, and SAC2iB solder joints

BEI in Figures 6.3.3 shows the influence of isothermal aging at 107°C, 150°C, and 180°C for 42 days (1008 hrs) on the microstructure of SAC305 and SAC2iB. In both types of specimens, Ag₃Sn particle sizes increase with temperature. However, Ag₃Sn particles appears to be smaller in SAC2iB at 150°C (Figures 6.3.3(b), and 5.3.3(e)), and 180°C (Figures 6.3.3(c), and 5.3.2(f)). This suggests that addition of POSS retards the growth of Ag₃Sn particles during isothermal aging. However, such visual distinction could not be

made for lower temperature i.e. 107°C (Figures 6.3.3(a), and 5.3.3(d)). Consequently, micrographs for lower temperatures have not been shown. Instead plots showing the variation of Ag_3Sn average particle diameter ($\langle D \rangle$) with time (t) in SAC305, and SAC2iB solder joints at different temperatures have been presented in Figures 6.3.4(a) – 5.3.4(f). Error bars represent 95% confidence intervals. It is evident from plots in Figures 6.3.4 that addition of trisilanol POSS retards the coarsening of Ag_3Sn particles. Studies on isothermally aged Sn-based solders have shown that the growth of Ag_3Sn occurs through diffusion of only Ag atoms [75, 81]. Results presented in this section further suggest that addition of trisilanol POSS influences the movement of Ag atoms within the solder matrix.

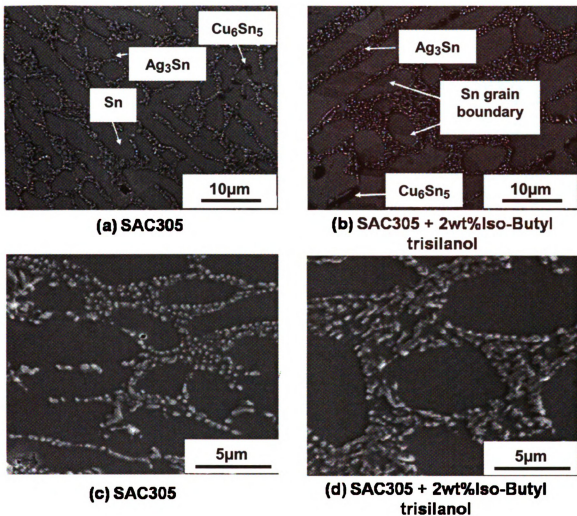


Figure 6.3.1 Backscattered electron images (BEI) showing the initial microstructures of (a) Sn-3.0wt%Ag-0.5%Cu (SAC305), and (b) SAC305 + 2wt% Iso-Butyl trisilanol POSS (SAC2iB). Different microconstituents within the microstructure have been indicated. High magnification SEM images showing the size and morphology of Ag_3Sn IMC particles in (c) SAC305, and (d) SAC2iB.

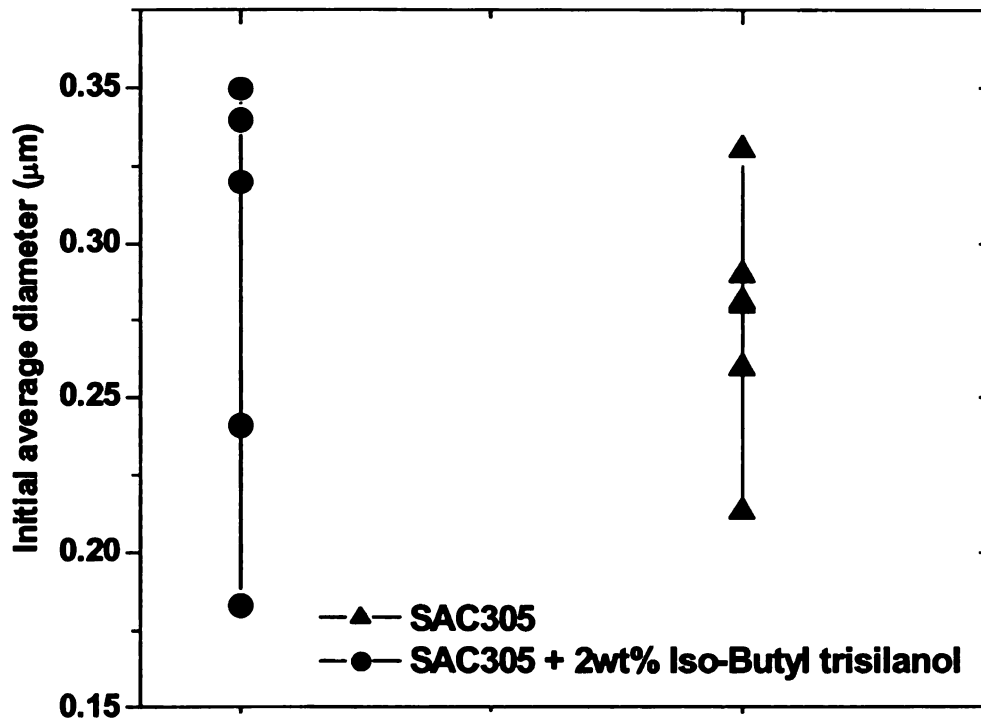


Figure 6.3.2 Distribution of Ag_3Sn particle sizes in SAC305 and SAC2iB

specimens. Two-tailed p value equals 0.54, suggesting that there is no statistical difference between the Ag_3Sn particle diameters in SAC305 and SAC2iB specimens. This analysis was carried out using six specimens for each type of solder joint.

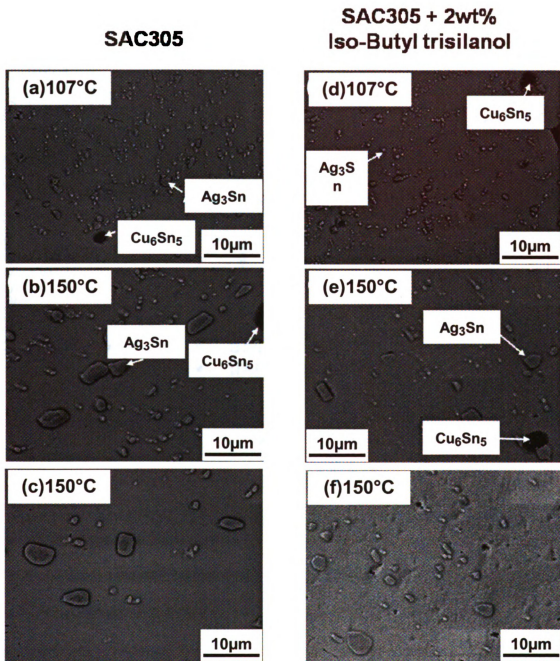


Figure 6.3.3 BEI showing the influence of isothermal aging at 107°C, 150°C, and 180°C on (a)-(c) SAC305 and (d)-(f) SAC2iB specimens.

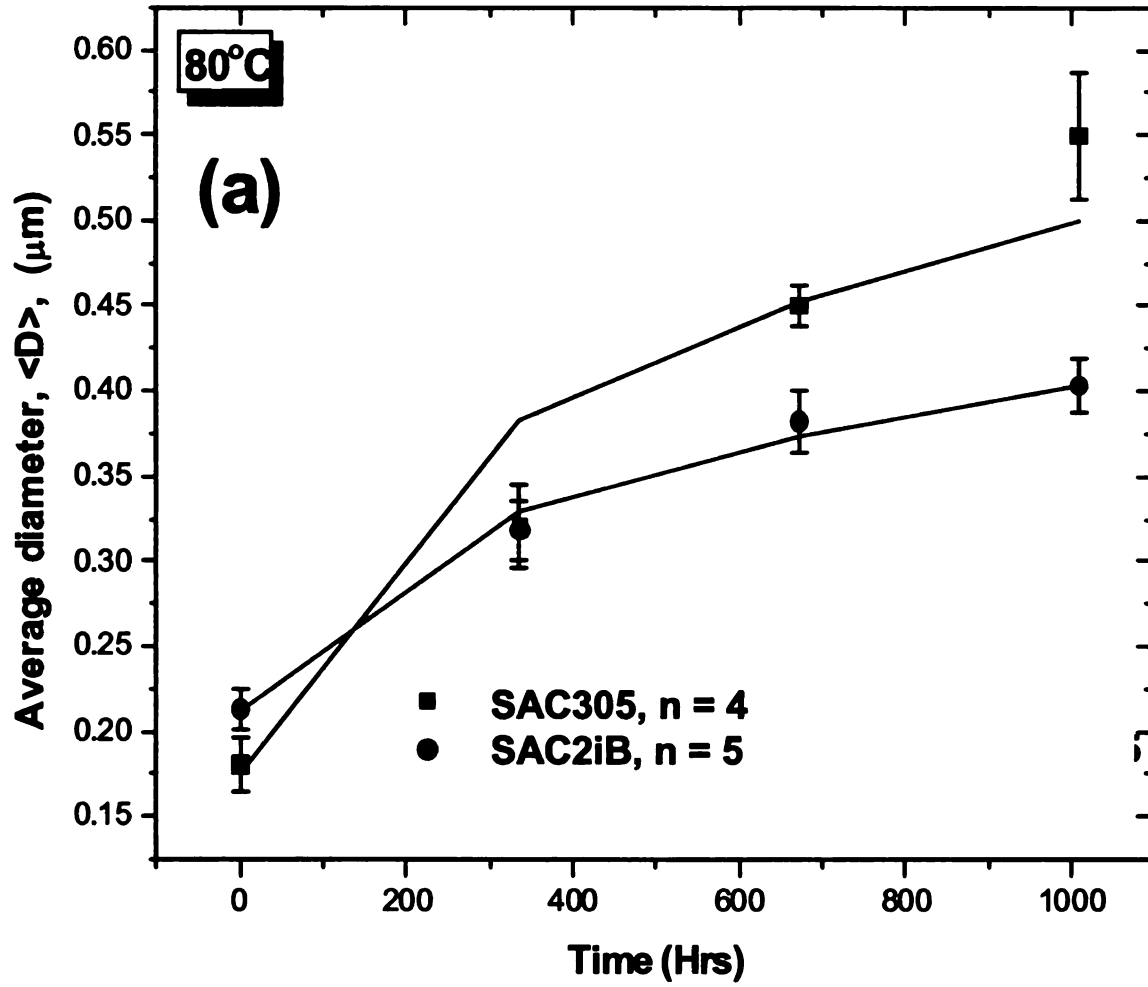


Figure 6.3.4 (a) $\langle D \rangle$ v.s. t plots comparing Ag_3Sn particle sizes in SAC305 and

SAC2iB specimens isothermally aged at 80°C.

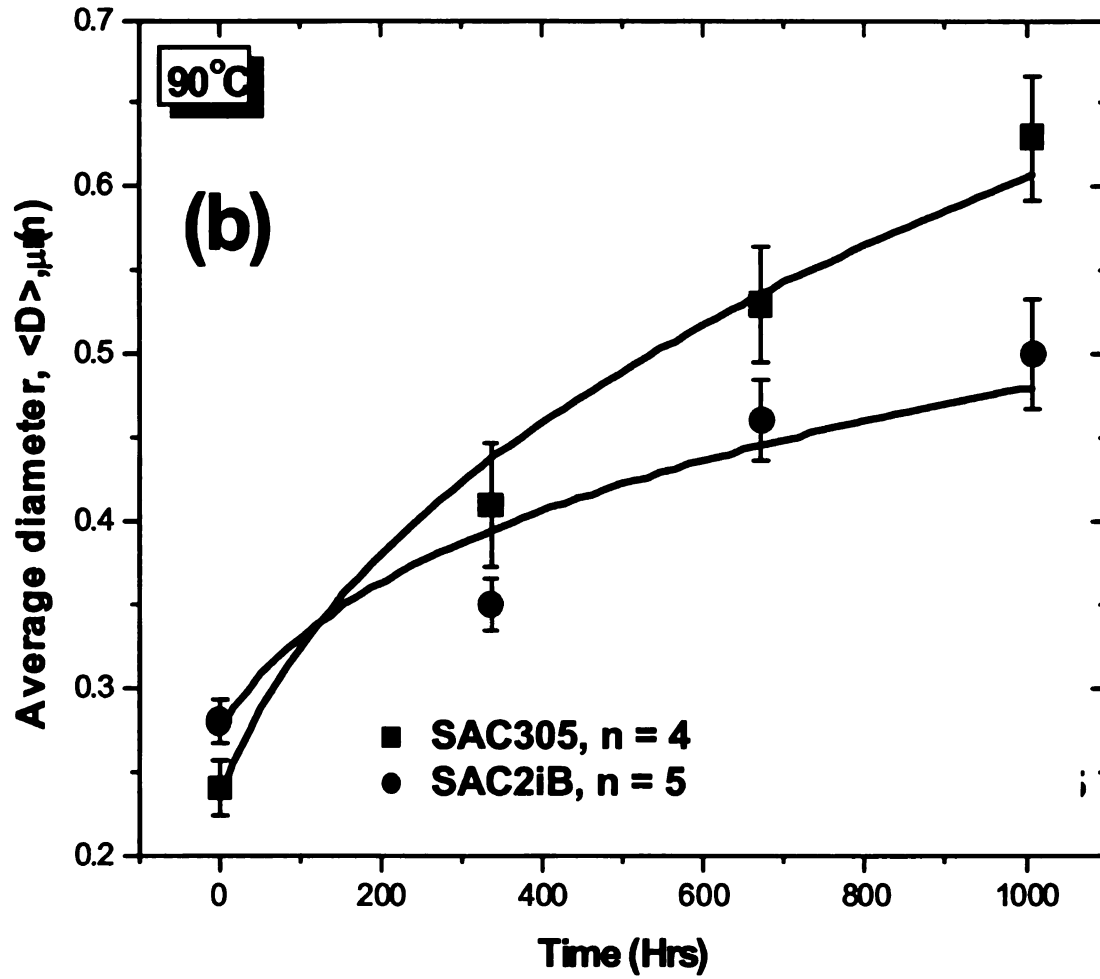


Figure 6.3.4 (b) $\langle D \rangle$ v.s. t plots comparing Ag_3Sn particle sizes in SAC305 and SAC2iB specimens isothermally aged at 90°C .

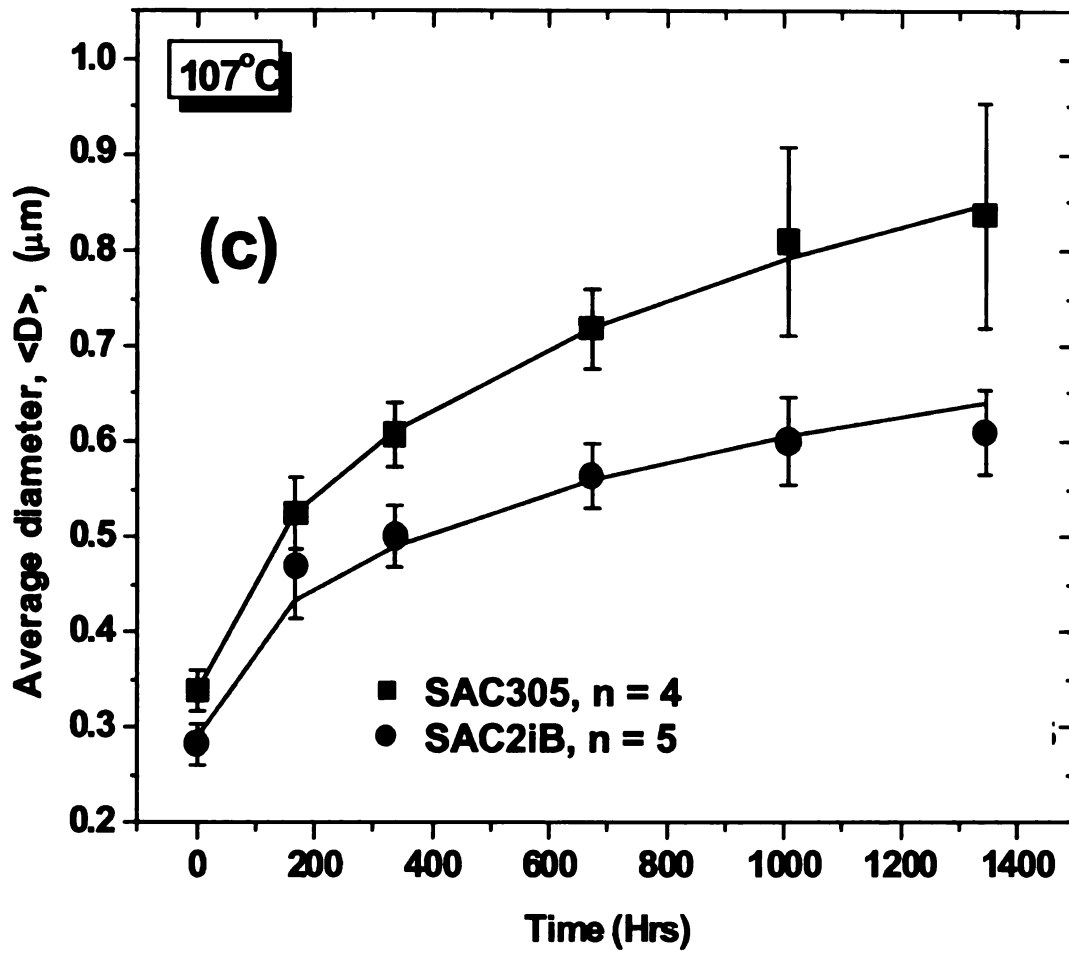


Figure 6.3.4 (c) $\langle D \rangle$ v.s. t plots comparing Ag_3Sn particle sizes in SAC305 and SAC2iB specimens isothermally aged at 107°C .

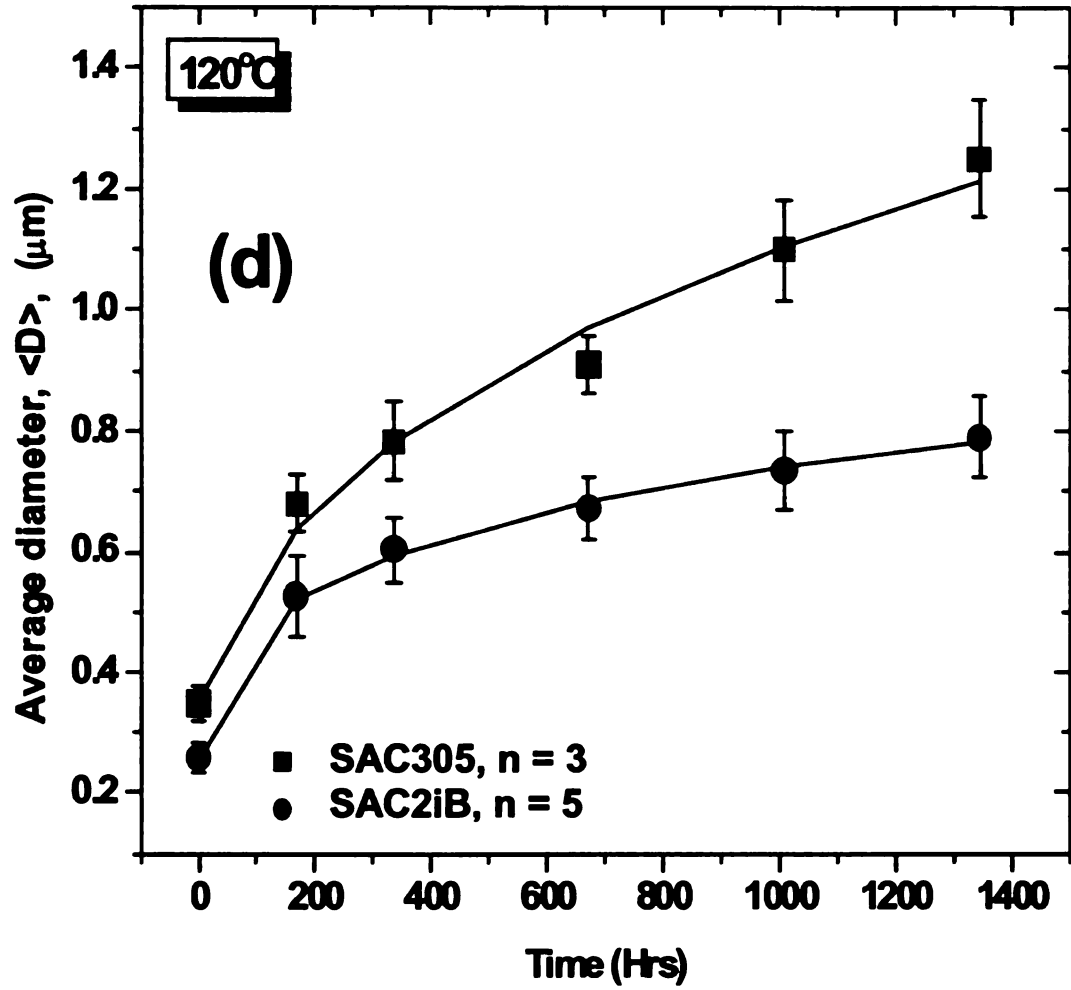


Figure 6.3.4 (d) $\langle D \rangle$ v.s. t plots comparing Ag₃Sn particle sizes in SAC305 and SAC2iB specimens isothermally aged at 120°C.

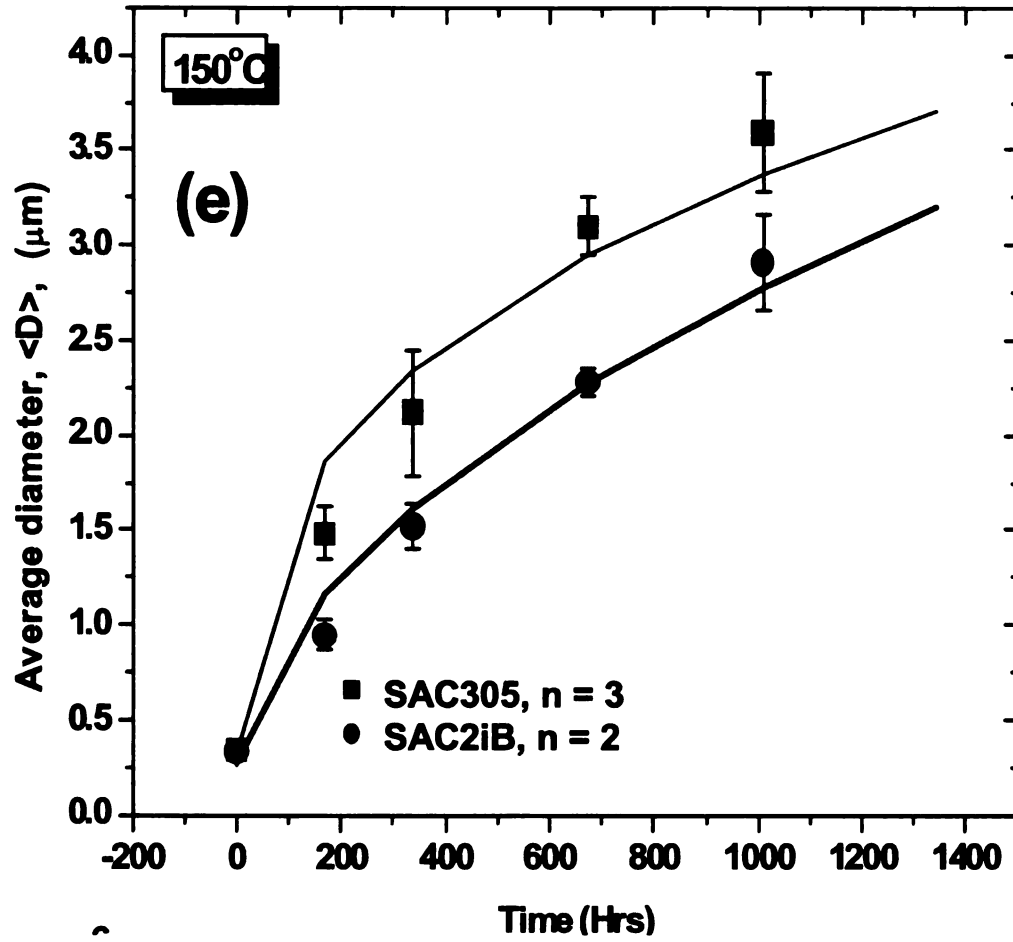


Figure 6.3.4 (e) $\langle D \rangle$ v.s. t plots comparing Ag_3Sn particle sizes in SAC305 and

SAC2iB specimens isothermally aged at 150°C .

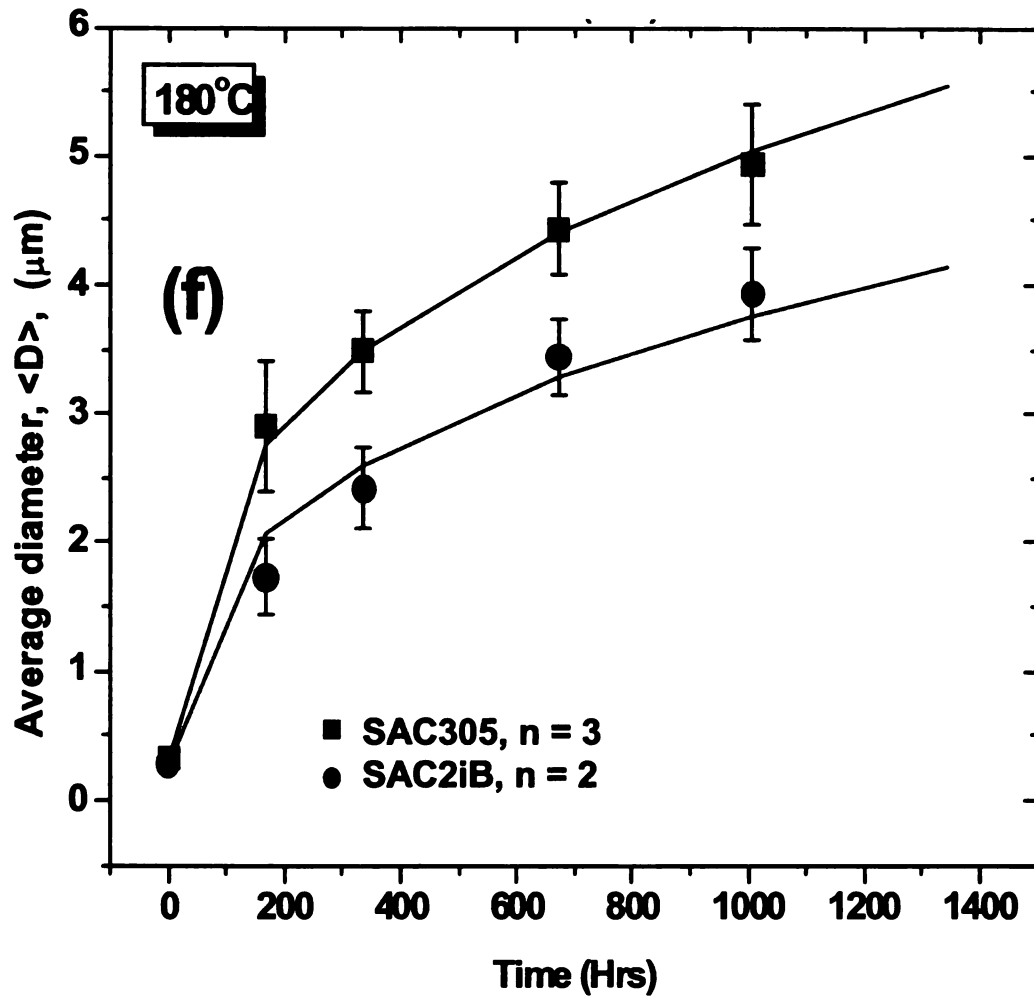


Figure 6.3.4 (f) $\langle D \rangle$ v.s. t plots comparing Ag_3Sn particle sizes in SAC305 and

SAC2iB specimens isothermally aged at 180°C .

6.3.3 Growth kinetics

As outlined in section 6.1, coarsening of secondary phases occur through diffusion of solutes through different mechanisms. Analysis of growth kinetics of such secondary phases reveals related mechanisms. Consideration of such mechanisms may further explain why trisilanol POSS additions retard coarsening of Ag_3Sn .

Growth kinetics are evaluated by finding out phase size constant "n" and temperature dependent constant "K" (equation (3)). To determine "n", non-linear regression was used, where different values of "n" (presented in Table 6.2) were substituted in equation (3) and the best-fit curve for a given "n" was obtained. Such curves have been plotted overlaying the data points in Figures 6.3.4 (e)-6.3.4(f). For all the fits, R^2 is greater than 0.9 (Table 6.3). After determining "n", $\langle D \rangle^n - \langle D_0 \rangle^n$ v.s. t is plotted (Figures 6.3.5) to obtain "K". Table 6.4 summarizes "K" values and R^2 for linear regression analyses. Further, activation energies of diffusion were obtained by plotting K v.s. $1/T$ on a logarithmic scale (Figures 6.3.6). Values of activation energies of diffusion for SAC305, and SAC2iB solder joints have been tabulated in Table 6.5. This table also integrates the results obtained from the analysis of growth kinetics by including rate controlling mechanisms at different temperatures of aging. Table 6.4 clearly shows that trisilanol POSS additions to SAC305 indeed change the rate controlling mechanisms contributing to coarsening of Ag_3Sn . Furthermore, It is

also apparent from Table 6.5 that, regardless of trisilanol POSS additions, there is dichotomy in rate controlling mechanisms depending on temperature regimes of isothermal aging.

At lower temperatures, grain boundary diffusion ($n=4$) dominates the growth of Ag_3Sn in SAC305 between 80°C - 107°C . However, in SAC2iB a very different rate controlling mechanism is operative in a similar temperature regime, since n equals 5 in this case. Such a value of n suggests that diffusion of Ag atoms occurs either through the grain boundary triple junctions or the dislocation cores. Furthermore, the change in diffusion mechanism ($n=4$ to $n=5$) may be explained by considering the effects of trisilanol POSS (with surface active Si-OH) on SAC305 microstructure. In chapter 5 it was shown that trisilanol POSS particulates are present at Sn-Sn grain boundaries. This means that movement of Ag atoms may be impeded by the presence of trisilanol POSS at the grain boundaries. Additionally, such an impediment may also exist even at the triple junction boundaries, since trisilanol POSS prefers to be present at the interfacial regions (chapter 5). Consequently, if interfacial diffusion is retarded by trisilanol POSS, then Ag atoms can diffuse only through the dislocation cores. Activation energy of such a process was experimentally determined by Herziq et.al. to be 76.02 KJ/mol [82]. This value is very close to 80.3 KJ/mol, determined in this study for SAC2iB. Additionally, activation energy of SAC2iB, at lower temperatures, is higher than that of SAC305 (60.3 KJ/mol), further indicating the retarding effect of trisilanol POSS addition on Ag_3Sn coarsening.

A similar comparison of activation energies could not be made for higher temperatures due to lack of data on SAC2iB (Table 6.5). However, trisilanol POSS addition results in the change of rate controlling mechanism also at higher temperatures (Table 6.5). Ag_3Sn coarsening in SC305 occurs by lattice diffusion ($n=3$) of Ag atoms through Sn, while growth of Ag_3Sn in SAC2iB is controlled by the transfer of Ag atoms across the $\text{Ag}_3\text{Sn} / \text{Sn}$ interface ($n=2$). It may be noted that there are two mechanisms operating in series during coarsening. At higher temperatures Ag atoms have to first diffuse through the lattice before crossing over the $\text{Ag}_3\text{Sn} / \text{Sn}$ interface. So the slowest step in the series will control the growth rate. It has been shown that trisilanol POSS is present at the IMC / Sn interfaces. Consequently, trisilanol POSS will hinder transfer of Ag across $\text{Ag}_3\text{Sn} / \text{Sn}$ interface making it the slowest step, and thereby retarding coarsening of Ag_3Sn even at temperatures as high as 180°C .

6.4 Conclusions

Addition of trisilanol POSS improves the microstructural stability of Sn-3.0wt%Ag-0.5%Cu solder joints. Such improvements are brought about by:

1. Retarding coarsening of Ag_3Sn particles within the solder matrix

2. The presence of trisilanol POSS at different interfaces ($\text{Ag}_3\text{Sn} / \text{Sn}$, and Sn / Sn grain boundaries). Their presence at those interfaces results in altering the rate controlling mechanisms responsible for Ag_3Sn coarsening.

Table 6.3 Statistical analysis for determining phase size constant “n” in $\langle D \rangle^n$ -

$$\langle D_0 \rangle^n = Kt \text{ through non-linear regression.}$$

Temperature (°C)	SAC305		SAC2iB	
	n	R ²	n	R ²
80	4	0.91634	5	0.9912
90	4	0.9578	5	0.9143
107	4	0.9974	5	0.9668
120	3	0.9869	5	0.998
150	3	0.9611	2	0.982
180	3	0.9979	2	0.9878

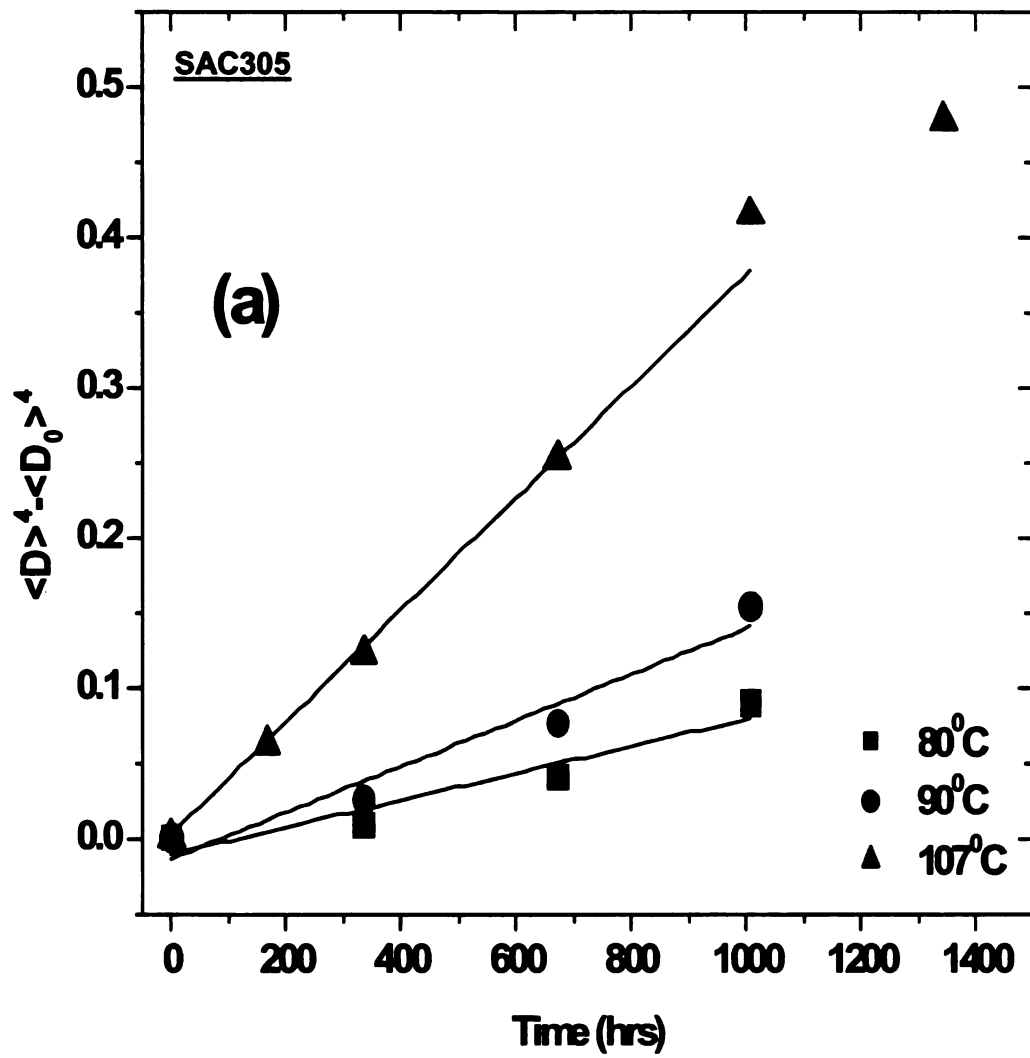


Figure 6.3.5 (a) Plot of $\langle D \rangle^4 - \langle D_0 \rangle^4$ v.s t for determining the "K" for SAC305

specimens isothermally aged at 80°C, 90°C, and 107°C.

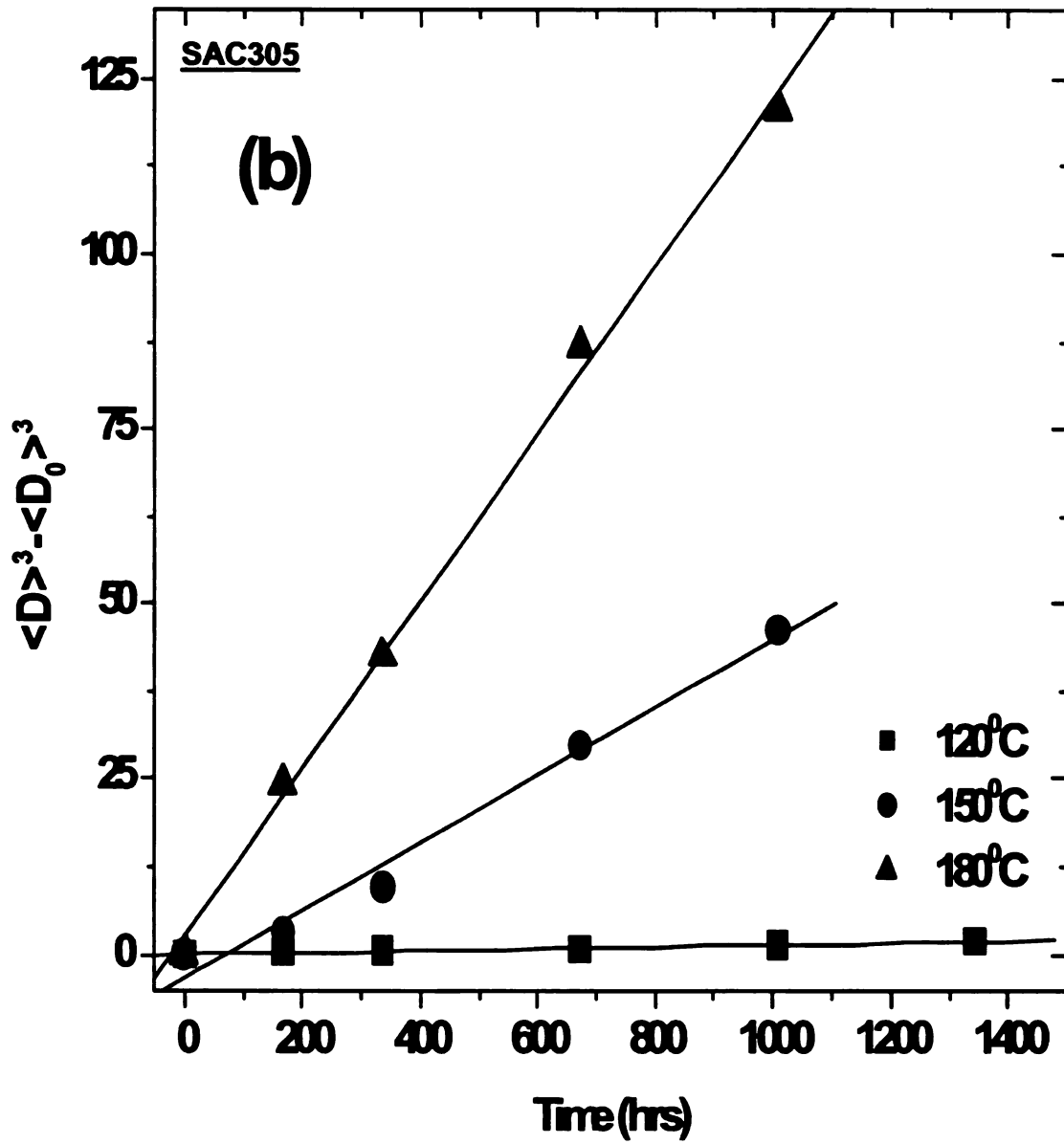


Figure 6.3.5 (b) Plot of $\langle D \rangle^3 - \langle D_0 \rangle^3$ v.s t for determining the "K" for SAC305

specimens isothermally aged at 120°C, 150°C, and 180°C.

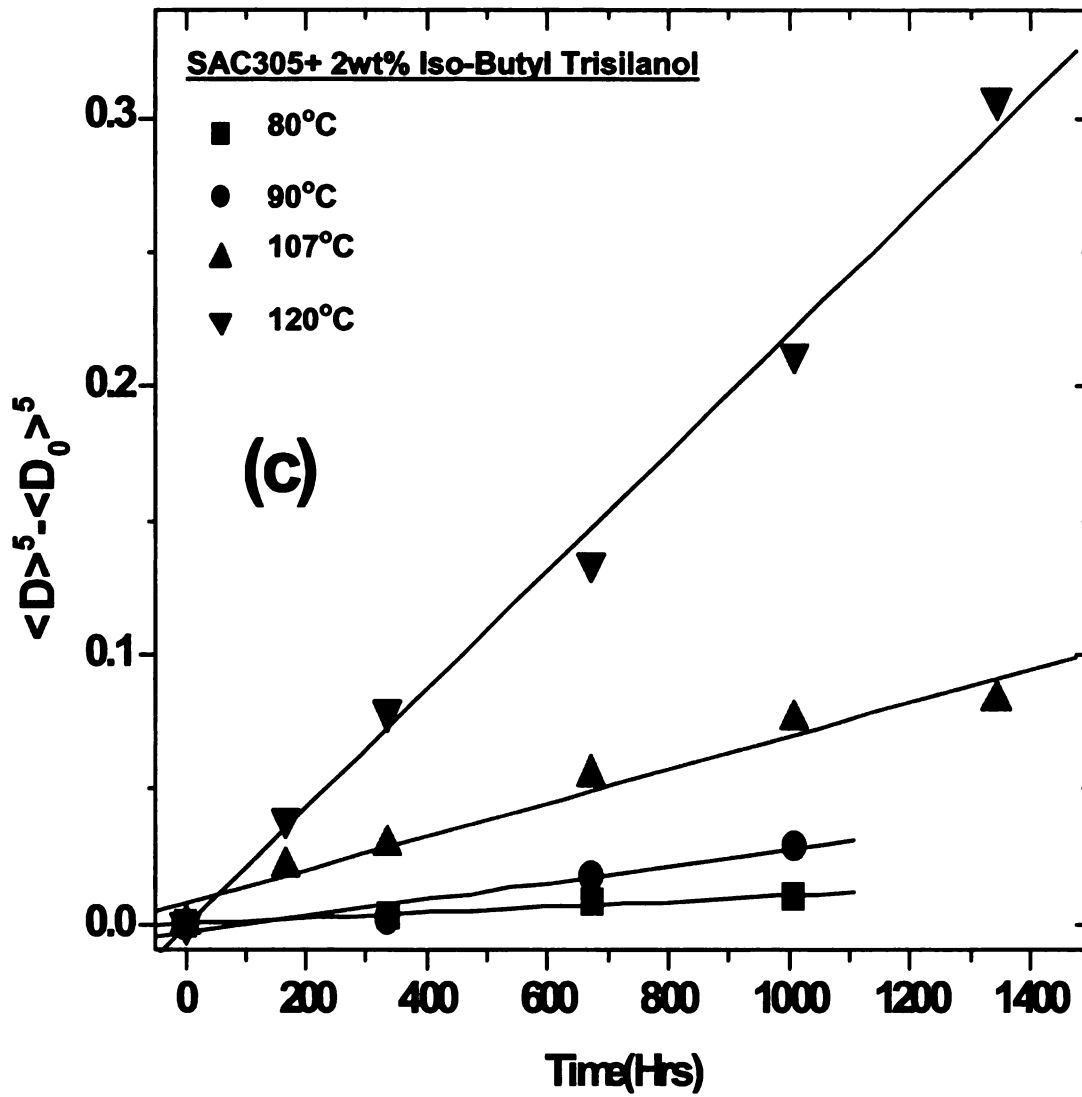


Figure 6.3.5 (c) Plot of $\langle D \rangle^5 - \langle D_0 \rangle^5$ v.s t. for determining the "K" for SAC2iB

specimens isothermally aged at 80°C, 90°C, 107°C, and 120°C.

Table 6.4 Linear regression analysis to determine "K" in $\langle D \rangle^n - \langle D_0 \rangle^n = Kt$ for the data presented in Figures 7

Temperature (°C)	SAC305		SAC2iB	
	K	R ²	K	R ²
80	9.00E-05	0.9481	1.00E-05	0.9841
90	2.00E-04	0.9149	3.00E-05	0.9349
107	4.00E-04	0.9795	6.00E-05	0.961
120	1.40E-03	0.989	2.00E-04	0.9933
150	4.82E-02	0.983	8.50E-03	0.9923
180	1.20E-01	0.9965	1.55E-02	0.9898

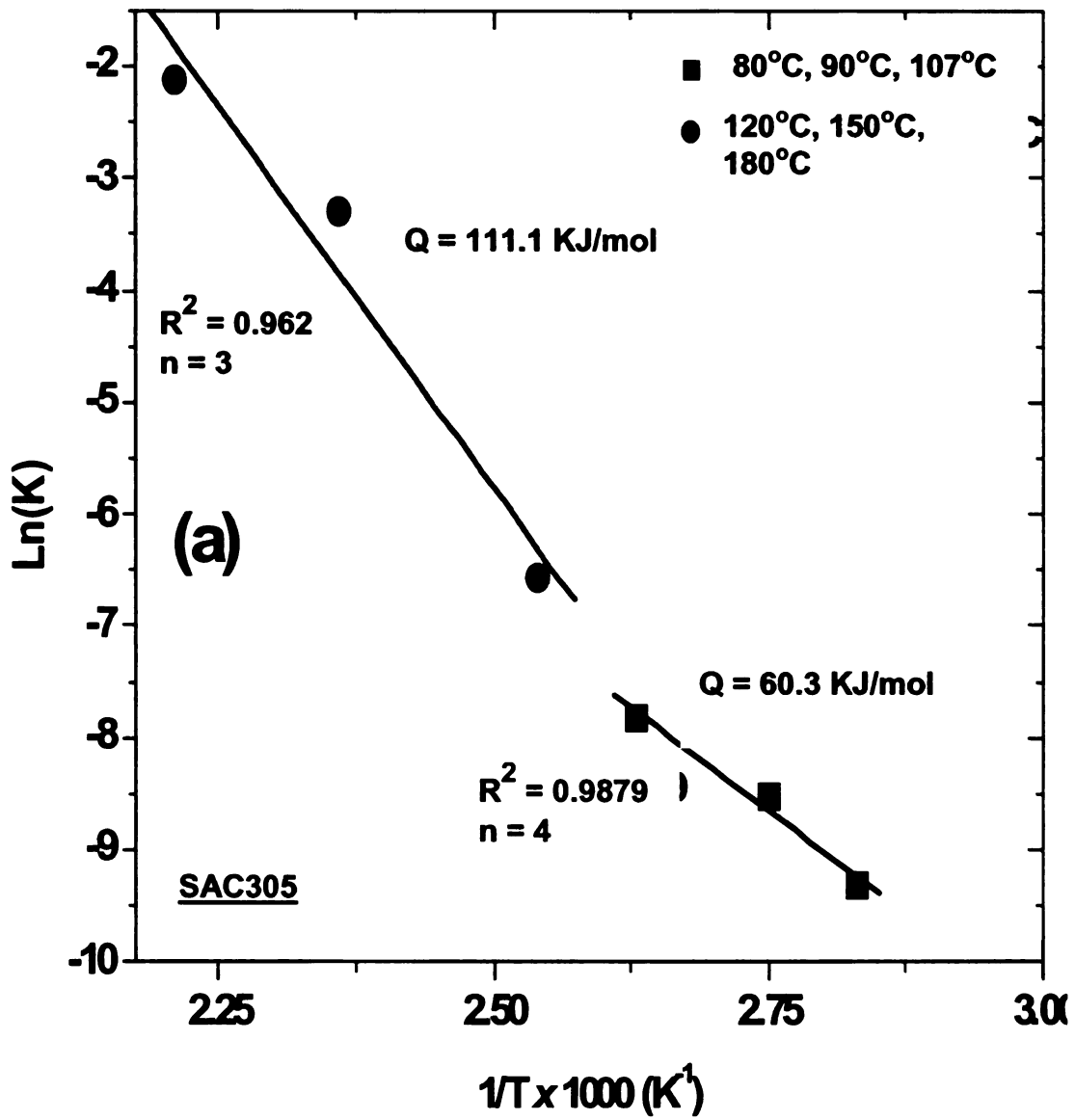


Figure 6.3.6 (a) Arrhenius plots for calculating activation energies for SAC305,

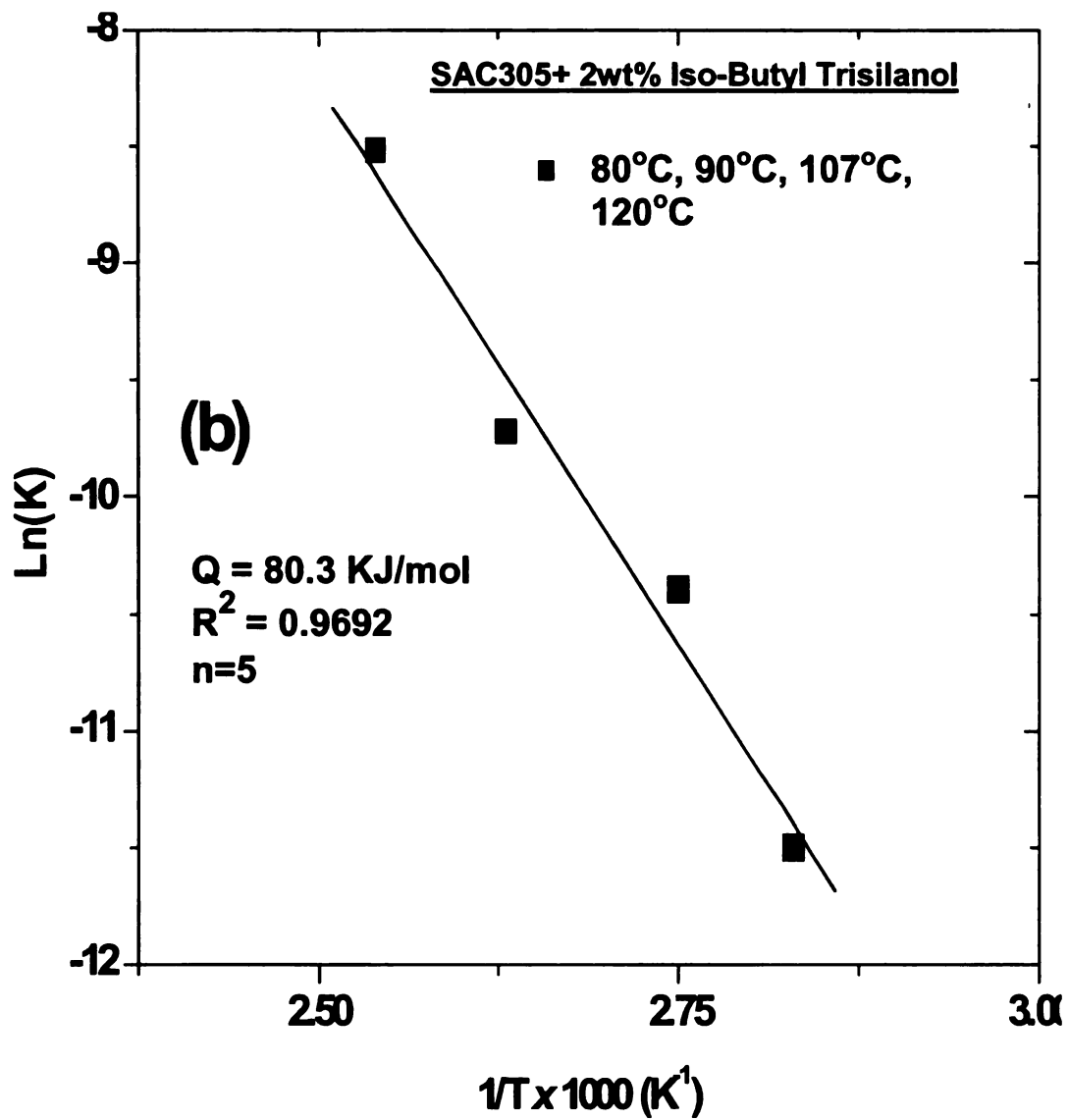


Figure 6.3.6 (b) Arrhenius plots for calculating activation energies for SAC2iB.

Table 6.5 Influence of POSS trisilanols on the activation energies of diffusion

Solder joint type	Temperature regime (°C)	n, rate controlling[75] mechanism	Calculated activation energy (KJ/mol)
SAC305	80 – 107	4, Grain boundary diffusion	60.3
	120 – 180	3, Lattice diffusion	111.1
SAC2iB	80 – 120	2, Diffusion through dislocation cores or through triple junctions	80.27
	150 – 180	5, Transfer of solutes across particle / matrix interface i.e. Ag ₃ Sn / solder interface	–

Chapter 7

Summary and recommendations

7.1 Summary

Comparison between solder joints subjected to low temperature regime (-55°C and 125°C) and high temperature regime (-15°C and 150°C) thermomechanical fatigue (TMF) indicates that the former is significantly detrimental to mechanical reliability of Pb-free Sn-based solder joints (chapter 3). Microstructural damages features suggested that, at lower temperature regime, limited ability Sn matrix to dissipate anisotropic strains due to TMF through plastic deformation. Consequently, during lower temperature regime TMF, cracks formed within solder during the early stages of TMF continue to propagate with progression of thermal excursions. In comparison, at higher temperature regimes the solder matrix is considerable compliant so as to undergo plastic deformation upon experiencing TMF. As a result cracks are not able to propagate during thermal excursions.

Another important finding resulted from the comparison between low and high temperature regime TMF of Pb-free Sn-based solder joints is that the interfacial damages play a significant role in both the cases. Interfacial IMC / Sn decohesion occurred during low temperature regime TMF whereas Sn / Sn grain boundary damages resulted at higher temperature regimes. These observations indicated that interfaces (between Sn grain boundaries and inter-phase interfaces) in Pb-free Sn-based solders are vulnerable during TMF.

TMF studies carried out on solder joints with iso-Butyl trisilanol POSS show considerably improved mechanical reliability (chapter 4). Microstructural observations suggested that iso-Butyl trisilanol POSS additions improved the ductility of the solder matrix, due to which the matrix was able to plastically deform and dissipate anisotropic stresses generated during TMF. As a result, cracks formed at the initial stages of TMF are not able to propagate in the later stages. Furthermore, plastic deformation of the solder matrix during TMF also suggests that it also experiences strain hardening, which would contribute to solder joint strength. Additionally, it was observed that the iso-Butyl trisilanol POSS additions improved the IMC / Sn bonding. This suggested the presence of trisilanol POSS at different interfaces eg. Sn / Sn grain boundaries and IMC / Sn.

Thermal analysis of bulk specimens (e.g. Kissinger's analysis) indicated the presence of iso-Butyl trisilanol POSS at the Sn / Sn grain boundaries (chapter 5). While observation of coarsened microstructure (chapter 5) and determination of coarsening kinetics of IMCs (chapter 6) confirmed the presence of such nanostructured chemical at the IMC / S interfaces.

As a consequence presence of iso-Butyl trisilanol POSS at different interfaces in conjunction with enhanced plasticity of the solder matrix improves the TMF reliability of trisilanol POSS added Pb-free Sn-based solder joints.

7.2 Recommendations

- 1) Thus far trisilanol POSS has eluded visual detection within the solder matrix due to its small size (1.5nm). This issue may be resolved through utilization of high resolution TEM observations. Such a method would also

be helpful in locating them at the IMC / Sn interfaces and determine if trisilanol POSS additions result in an orientation relationship between the IMCs and Sn.

- 2) This study has shown that isobutyl trisilanol POSS are present at different interfaces in solid state. However, the interaction of trisilanol POSS in the liquid (molten) solder is yet to be ascertained. *In-situ* studies based on synchrotron X-ray diffraction may be helpful towards that end. Alternatively, molecular dynamics simulations may also provide clues. This knowledge may prove useful in understanding the final solidified microstructure and possibly provide means of engineering the final microstructure.
- 3) It must also be pointed out that the present study only leverages the silanol (Si-OH) groups present in trisilanol POSS for bonding with the metallic matrix (Si-O-metal). There exists a possibility of utilizing the organic (e.g. isoButyl) groups attached to the $\text{SiO}_{1.5}$ framework. If, through appropriate chemistry, the size of POSS (with silanol groups) anatomy is increased, and organic groups are made considerably larger (microns) and thermally stable, then the organic groups might also be able to act as cushions for accommodating strains generated within the solder during TMF.
- 4) Finally, pertaining to the TMF behavior of Pb-free Sn-based solders, continuum mechanics based models may be used to predict their life time reliability. At present there are many such models; however there are very

few that incorporate damage cause due to TMF. Continuum damage mechanics (CDM) provides the means of doing so. CDM incorporates the effects of submicron sized cracks and the plasticity of materials to determine their mechanical response. Consequently, CDM framework may be adopted for our purposes, although it has to be modified for the inherent anisotropy of Sn since most continuum based models deals with isotropy.

Appendix A

Influence of polyhedral oligomeric silsesquioxanes trisilanol chemistry on the low temperature regime thermomechanical fatigue behavior of nanocomposite Sn-based solder joints

Rationale and objectives

The solder pastes used in this study are essentially a fine dispersion of solder alloy (of known composition) particulates in an organic flux. However, the composition of that flux is difficult to ascertain, since its chemistry is protected through patent laws. Consequently, during processing it problematic to evaluate the interaction between the flux and the organic ("R") group attached to the polyhedral oligomeric silsesquioxanes POSS cage.

Preparation of nanocomposite solder joints involves mechanically mixing a particular variety of POSS trisilanol nanostructured chemical with the commercial available solder paste. Upon solidification, depending on the interaction with the flux, the "R" group may influence the microstructure, and possibly the thermomechanical fatigue (TMF) behavior of Sn-based solder joints. Thus far only one variety of nanostructured chemical was utilized, namely Iso-Butyl trisilanol POSS. It was shown that such reinforcements improved the low temperature regime TMF reliability of Sn-based solder joints. For POSS trisilanols to be a viable reinforcement, it is necessary to obtain a consistently improved TMF behavior irrespective of the type of "R" group attached to the POSS trisilanol reinforcements. Consequently, this chapter investigates the influence of phenyl trisilanol POSS reinforcements on the low temperature

regime TMF behavior of Sn-based solder joints. Phenyl trisilanol POSS was chosen, since it has a lower thermal stability than Iso-Butyl trisilanol POSS [59, 60, 83]. Consequently, the results presented in this section will also depict effects two possible extremes of POSS trisilanol reinforcement selection (based on thermal stability) on the low temperature regime TMF behavior of Sn-based solder joints.

A1 Experimental details

Experimental procedures followed in this study have been described in detail in chapters 2, 3, and 4. This section provides a summary those procedures.

Eutectic Sn-3.5wt%Ag (SA) and Sn-3.0wt%Ag-0.5wt%Cu (SAC305) solder pastes were obtained from the same vendor. Brand of the solders pastes are similar to that of prior studies i.e. R520A. Nanostructured chemical phenyl trisilanol POSS was procured from Hybrid Plastics®. Following the processing procedure described section 2.1, phenyl trisilanol POSS was mechanically mixed with SA and SAC305 to prepare solder pastes of compositions SA + 2wt% phenyl trisilanol POSS (SA2phe) and SAC305 + 2wt% phenyl trisilanol POSS (SAC2phe). The resulting pastes were then utilized for preparing nanocomposite solder joints according to section 2.2.

To conduct TMF studies, SA2phe and SAC2phe nanocomposite solder joint were subjected to thermal cycling between -55°C and 125°C in an environmental chamber. Details of the temperature profile utilized have been provided in section 2.4. Mechanical and microstructural techniques necessary for investigating the influence of TMF have been discussed in section 2.6.

A2 Results and discussion

This section establishes microstructure –mechanical property relationship of phenyl trisilanol POSS reinforced nanocomposite solder joints subjected to TMF. Anatomy of phenyl trisilanol POSS (pheTriPOSS) has been shown in figure A1.

In the schematic the organic "R" group consists of phenyl (-C₆H₅) group, while in the previous studies (chapter 4, 5, and 6) the "R" group was Iso-Butyl (-C₄H₉).

A2.1 Effect of phenyl trisilanol POSS on the residual mechanical behavior of Sn-based solder joints

Figures A2 plots the residual shear strength as a function of number of TMF cycles. Figure A2 (a) compares the residual mechanical behavior of SA and SA2phe solder joints, while Figure A (b) compares the residual mechanical behavior of SAC305 and SAC2phe solder joints.

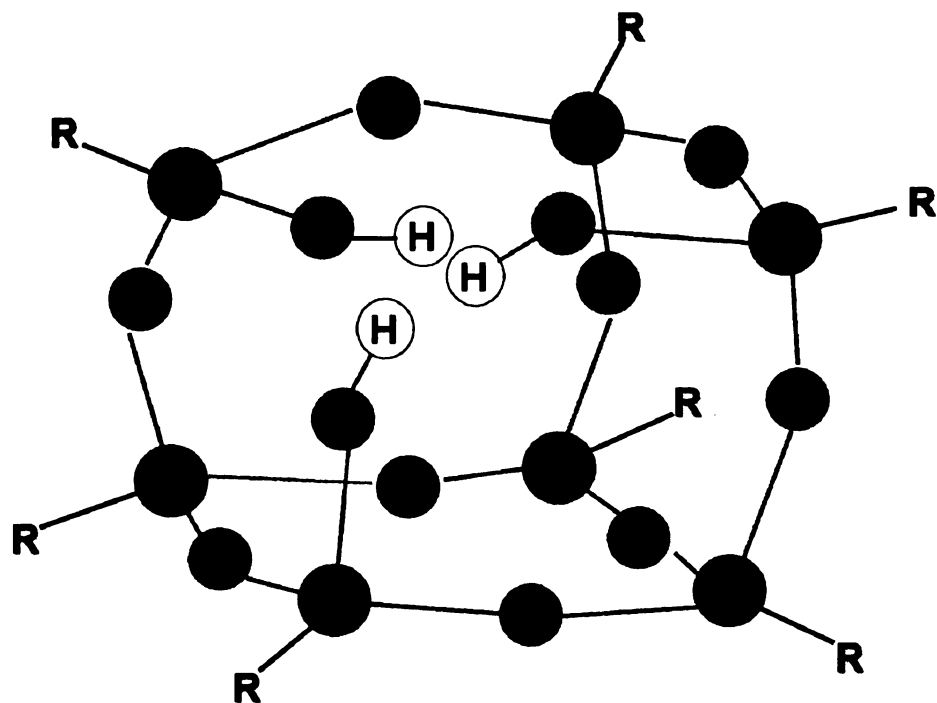
These plots suggest that addition of 2wt% pheTriPOSS stabilized the residual strength of nanocomposite (SA2phe, and SAC2phe) solder joints after 100 cycles. Further confirmation was obtained through t-test (Tables AI), which compares the residual strength data after 100 cycles with that of 400, 500, and 1000(SAC2phe). Single tail p-values for all such comparisons are less than 0.05, indicating that the compared data sets are statistically different. Figures A2 also indicates that residual strength of SA2phe and SAC2phe solder joints stabilized at a higher value than the control specimens (SA and SAC205). Similar results were obtained upon addition of 2wt% Iso-Butyl trisilanol POSS (ibutTriPOSS) reinforcements to Sn-based solder joints (chapter 4).

However pheTriPOSS reinforced nanocomposite solder joints exhibited differences in residual mechanical behavior, as compared to ibutTriPOSS reinforced joints. IbutTriPOSS reinforcements did not change the initial strength of both SA and SAC305 (Figures 4.3.1), whereas pheTriPOSS reinforcements

increased the initial strength of SA joints but decreased that of SAC305 joints. Progressive TMF cycles caused a drop in the residual strength of SA2phe and ibutTriPOSS reinforced joints, except for SAC2phe solder joints. In fact successive thermal excursions do not seem to affect the residual strength of SAC2phe joints. This observation is further corroborated by single tail p-values, which were obtained after comparing residual strength data for 1 cycle with other chosen number of TMF cycles (Table AI).

Based on this analysis one can infer that pheTriPOSS reinforcements have different influences on the SA and SAC305 solder joints subjected to TMF. Moreover, these results also indicate that pheTriPOSS reinforced Sn-based solder joints do not exhibit consistent residual mechanical behavior as observed in ibutTriPOSS reinforced solder joints. This further suggests that processing with different organic "R" group (phenyl or Iso-Butyl) may elicit different TMF response from the reinforced solder joints.

Nonetheless, it is evident that irrespective of the "R" group, addition of POSS with silanol (Si-OH) bonds improves the mechanical reliability of Sn-based solder joints. To correlate the improved residual mechanical behavior (of SA2phe and SAC2phe solder joints) with resulting microstructural damage due to TMF, microstructural characterization was carried out. Results of that characterization have been presented in the following section.



● Si

● O

R phenyl

≡

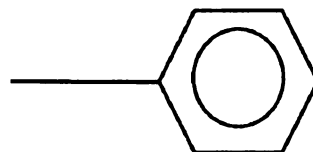


Figure A1 Schematic showing the anatomy of POSS trisilanol. Chemical formula of the organic phenyl (R) group is also shown.

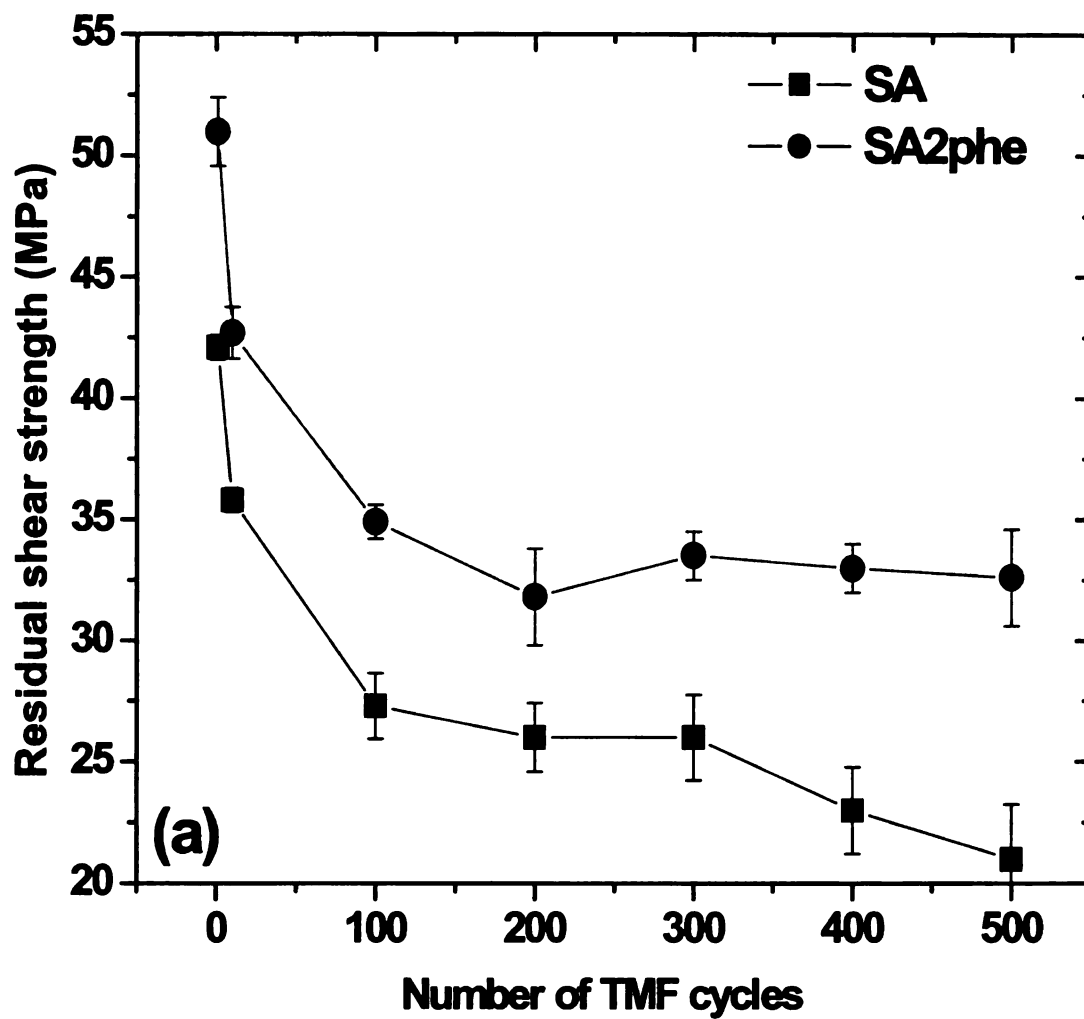


Figure A2 (a) Plots comparing influence of pheTriPOSS on the residual mechanical behavior of SA.

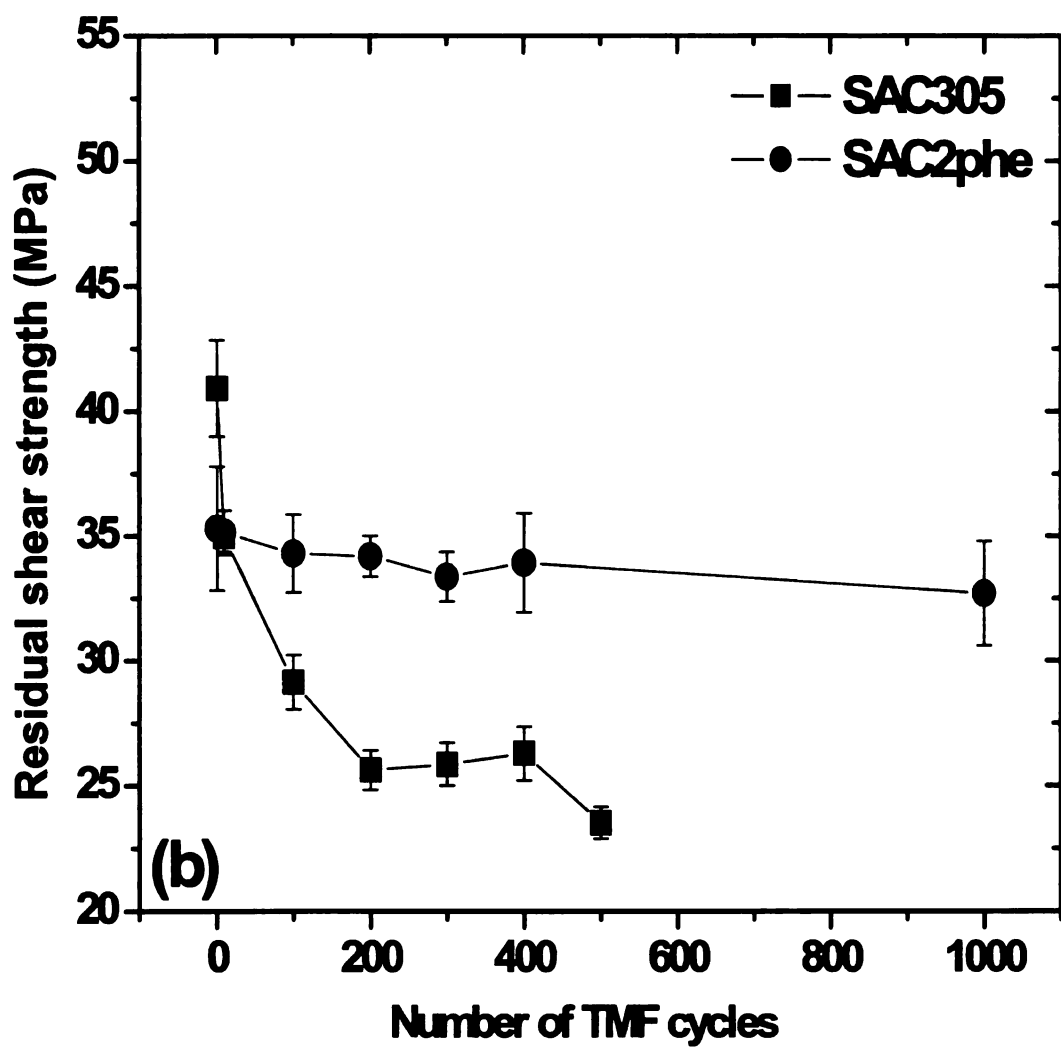


Figure A2 (b) Plots comparing influence of pheTriPOSS on the residual mechanical behavior of SAC305.

Table A1 Comparison of single tail p-values obtained from t-test. Here residual strength data after 1 and 100 cycles are compared with 100, 400, and 500 cycles for SA2phe and 100, 400, and 1000 cycles for SAC2phe. P-values <0.05 would indicate that the compared data sets are statistically different.

Material	SA2phe		SAC2phe	
Number of TMF cycles	1 cycle	100 cycles	1 cycle	100 cycles
100 cycles	< 0.001	0.5	0.19	0.5
400 cycles		0.06	0.352	0.41
500 cycles		0.102	-	-
1000 cycles		-	0.227	0.244

A2.2. Influence of phenyl trisilanol POSS reinforcements on microstructural damages

Microstructural evolution of SA2phe and SAC2phe solder joints has been depicted in Figures A3 and A4 respectively after 0, 100, and 500 cycles of TMF. It is evident from the scanning electron microscope (SEM) images that SA2phe accumulates significant more surface damage within the solder region as compared to SAC2phe. High magnification SEM images further comparing the intensity of surface damage within the solder region after 500 cycles of TMF have been shown in Figure A5. It is observed that SAC2phe (Figure A5 (a)) experiences minimal surface damage as compared to SA2phe (Figure A5 (b)).

These SEM images imply that anisotropic strains (due to thermal excursions) are accommodated through plastic deformation of the solder region in SA2phe solder joint. However in case of SAC2phe, lack of plastic deformation of the solder matrix suggests that anisotropic strains are accommodated elsewhere within the joint. In chapter 3 and 4 it was shown that Cu_6Sn_5 / Sn interfaces (in Sb-based solder joints) are vulnerable during low temperature regime TMF between -55°C and 125°C . Consequently, Figures A6 compares the microstructural damage adjacent to the interfacial Cu_6Sn_5 layer / solder region after 500 cycles for both SA2phe (Figure A6 (a)) and SAC2phe (Figure A6 (b)) specimens. The interfacial region in SA2phe shows extensive damage within the solder matrix as compared to SAC2phe. Furthermore, Cu_6Sn_5 layer /

Sn decohesion is barely noticeable in SA2phe, whereas such a damage is clearly visible in SAC2phe specimen.

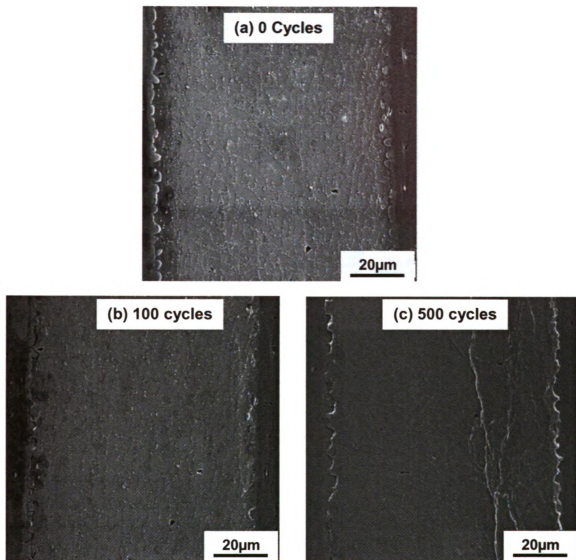


Figure A3 SEM images showing microstructural evolution in SA2phe solder joints after (a) 0, (b) 100, and (c) 500 cycles

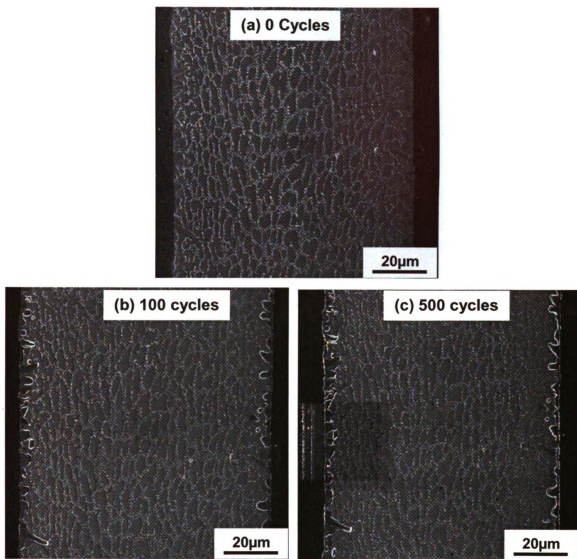


Figure A3 SEM images showing microstructural evolution in SAC2pHe solder joints after (a) 0, (b) 100, and (c) 500 cycles

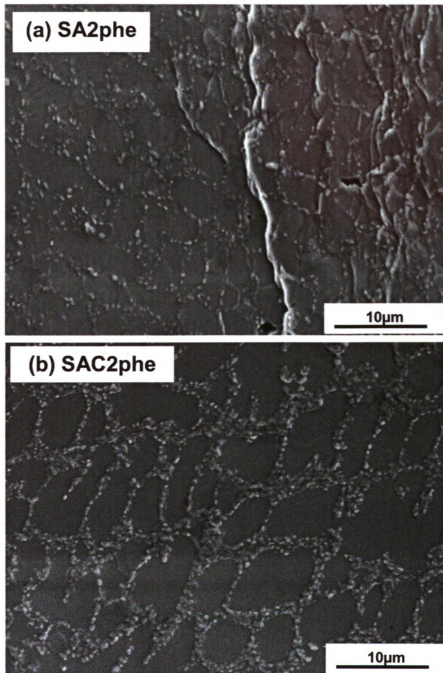


Figure A5 High magnification SEM images comparing surface damage within solder region after 500 cycles of TMF in (a) SA2phe and (b) SAC2phe specimens.

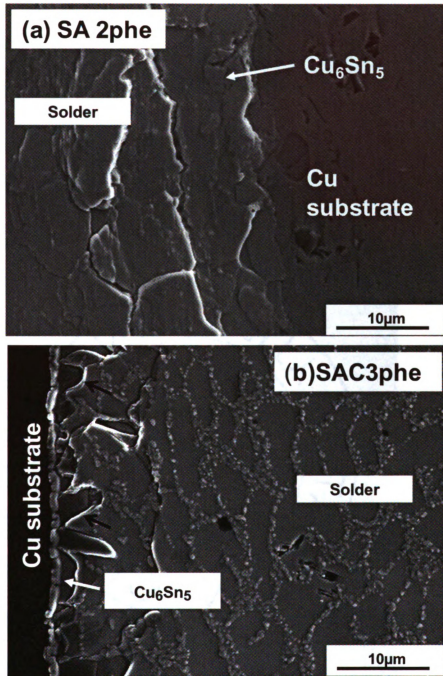


Figure A6 SEM images comparing the interfacial damage after 500 cycles in (a) SA2phe and (b) SAC2phe. Cu_6Sn_5 / Sn decohesion in SAC2phe have been indicated by black arrows.

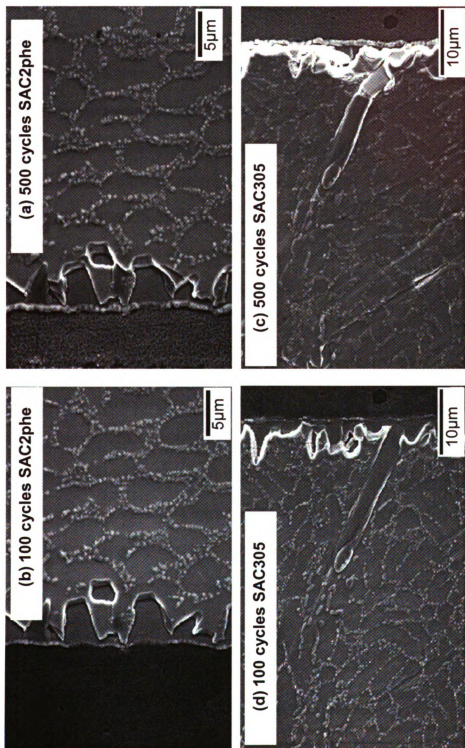


Figure A7 Compares microstructural evolution of the Cu₃Sn₅ layer / solder interfacial region for (a)-(b) SA2phe and (c)-(d) SAC2phe after 100 and 500 cycles. These images show phenyl trisilanol reduces the intensity of interfacial damage.

However, SEM images comparing interfacial damage evolution between SAC2phe (Figures A7 (a)-(b)) and SAC305 (Figures A7 (c)-(d)) suggests that the intensity of damage and its evolution (due to low temperature regime TMF) in SAC2phe is relatively less than the control SAC305 specimen.

In essence these observations tend to suggest that pheTriPOSS reinforcements improve Cu_6Sn_5 layer / Sn bonding in SA, whereas such effects are not so prominent for SAC305. It may be noted that irrespective of alloy composition, ibutTriPOSS reinforcements resulted in considerable plastic deformation within the solder region (Figures 4.3.6) and minimized Cu_6Sn_5 / Sn decohesion (Figures 4.3.7 and Figures 4.3.8).

A3. Conclusions

Based on residual mechanical strength and microstructural evaluations, the following may be inferred about the effects of pheTriPOSS reinforcements on the low temperature regime TMF behavior of Sn-based solder joints:

1. PheTriPOSS reinforcements improve the mechanical reliability of SA and SAC305 solder joints by stabilizing the residual mechanical behavior to a higher strength. Similar improvements have been observed in ibutTriPOSS reinforced solder joints. This suggests that Si-OH bonds in POSS trisilanols are more important for improving the mechanical reliability of Sn-based solder joints than the organic "R" group (Iso-Butyl or phenyl).

2. Microstructural and residual mechanical results show that improvement in mechanical reliability is brought about in different ways depending on the composition of solder alloy.
3. In case of SA2phe, during the early stages of TMF, initial drop in residual strength may be attributed to accumulation of surface damage due to plastic deformation of the solder matrix. In the later stages of TMF, residual mechanical behavior stabilizes at a higher strength (as compared to SA) due to accommodation of anisotropic strains (due to TMF) through plastic deformation of the solder matrix and improvement in Cu₆Sn₅ layer / Sn interfacial bonding.
4. On the other hand, low temperature regime TMF does not seem to affect the residual mechanical behavior of SAC2phe solder joints. Lack of plastic deformation of the solder matrix with progressive TMF cycles may be major contributing factor.
5. Results presented further show that chemistry of POSS trisilanol also plays a role. Different "R" groups (attached to POSS trisilanol) may react with the solder paste in a very different way during processing. Thus resulting in an as-solidified microstructure, which accommodates anisotropic strain due to TMF in a different manner.

Appendix B

Strain assisted allotropic transformation of β -Sn

Rationale and objectives

Tin-pest, which involves allotropic transformation of β -Sn to α -Sn at temperatures below 13.2°C , has been recognized as a potential reliability concern for Sn-based lead-free electronic solder joints. Effect of imposed pre-strain on $\beta \rightarrow \alpha$ Sn transformation was investigated by bending rectangular specimens of 99.99% pure bulk β -Sn to known outer fiber strain levels, followed by aging at -15°C . α -Sn was observed on the narrow side surface of the specimens bent to non-uniform and uniform curvatures after 2.1 and 3.5 months, respectively. Microstructural characterization was carried out to understand the influences of (1) imposed strain on the α -Sn region, and (2) the advancing β/α Sn phase boundary on the adjoining β -Sn. Growth rate studies revealed that α -Sn grew significantly faster under the influence of tensile pre-strain as compared to compressive pre-strain.

B1. Introduction

At temperatures of 13.2°C and below, pure Sn can transform from β -Sn (body-centered-tetragonal) to α -Sn (diamond-cubic). This allotropic transformation involves a change of density from 7.265 gm/cm^3 to 5.769 gm/cm^3 [61], a volumetric change of almost 26 %. This transformation is also known to be an autocatalytic event, where the transformation will speed up once it starts. Therefore, to reduce this incubation time, a large bulk β -Sn specimen is often inoculated with a small piece of α -Sn [40]. The region surrounding this small inoculated α -Sn will quickly undergoes the $\beta \rightarrow \alpha$ Sn transformation. In addition, the reverse transformation, $\alpha \rightarrow \beta$ Sn, will take place when the temperature is raised to above 13.2°C . However upon cooling back to below 13.2°C , the previously infected region will quickly convert back to α -Sn with little or no incubation requirement. For these reasons, α -Sn is referred as tin-pest or tin-disease. The corresponding volumetric increases upon transition and the brittle nature of α -Sn will result in a complete disintegration of specimens made of Sn and alloys with high Sn content [84, 85]. Therefore, the occurrence of tin-pest has been identified as a serious potential reliability concern for microelectronics industry where Sn-based lead-free alloys are expected to be used extensively in electrical interconnects [40, 41].

Solder joints are expected to experience various levels and gradients of stress and/or strain by virtue of their geometry and the imposed service

environments [86, 87]. Consequently factors such as temperature, mechanical loading, strain imposed due to the mismatch of thermal expansion coefficients between substrate and solder, and concentration of certain impurity elements can effect the tin-pest formation at sub-zero environment. One of the earlier studies on the effects of mechanical deformation on $\beta \rightarrow \alpha$ Sn transformation was carried out by Roger et.al. [88]. However, neither the magnitude of the imposed strain nor the kinetics of α -Sn growth on the strained specimen was reported. A more quantitative assessment of the influence of mechanical deformation on tin-pest formation was conducted by Joo et. al.[89]. They observed α -Sn regions on cold-rolled Sn-0.8%Cu specimens within few days during isothermal aging at -30°C [89]. It was suggested that the rate of transformation was directly proportional to the imposed reduction ratio. Plumbridge's group had also reported α -Sn formation on the machined surfaces of Sn-0.5%Cu specimens, when stored at -18°C for more than a year. They attributed the transformation to the residual stresses resulting from the machining operation [40, 85]. In any case, both cold-rolling and machining produce complicated strain states on the surface of the specimen. Hence, it is more difficult to assess the effect of individual components of strain tensor on the transformation. In addition, there have been very few studies that address the microstructural aspects of this transformation[40, 84, 85, 90]. The objective of this work is to understand the fundamental issues related to the influence of strain on the tin-pest formation and the relative kinetics by the level of imposing strain. As describe below, well-

characterized deformation were imposed on 99.99% pure bulk β -Sn specimens, store at a constant sub-zero temperature and periodically removed to room temperature for observation of any $\beta \rightarrow \alpha$ transformation. In addition, for specimens underwent tin pest formation, we report the kinetics as well as the mechanical property near the transformed region.

B2. Experimental details

B2.1 Mechanical Pre-Straining

Commercially available 99.99% pure bulk β -Sn specimens of rectangular geometry were subjected to three types of mechanical pre-straining followed by aging at -15°C . In the first set, five metallurgically polished β -Sn specimens (35 mm x 8 mm x 2.3 mm) were pressed around semi-circular channels to achieve 4.8%, 5.8%, 7.7%, 11.5%, and 23.0% outer fiber strains. In the second set, a specimen (20 mm x 12 mm x 1.2 mm) was bent to non-uniform curvatures with outer fiber strains ranging from 3.6% to 6%.

B2.2 Characterization and measurements

X-ray diffraction was used to verify the transformed region is that of α -Sn phase. SEM and stereo-optical microscopy were utilized for microstructural characterization of transformed regions. Mechanical characterization was carried out with Vickers hardness testing with a load of 1 Kg applied for 10 seconds. Kinetics of $\beta \rightarrow \alpha$ transformation was studied by measuring the temporal evolution of the transformed areas by periodically recording images of transformed regions with a calibrated stereo-optical microscope. The transformed area was then measured directly from the digital image with a resolution of 5 μm per pixel.

B3. Results and discussion

B3.1 Effect of mechanical pre-straining on the allotropic transformation of β -Sn

α -Sn formation was noted on the narrow side surfaces in regions very close to the broad outer surface of the non-uniformly and the uniformly bent specimens after 2.1 and 3.5 months of storage at -15°C , respectively. On the non-uniformly bent specimen, α -Sn was located in the region with 6% tensile outer fiber pre-strain. This observation is consistent with the results published by Roger et.al, where α -Sn was reported to have formed on the tensile side of bent specimens [88]. However, $\beta \rightarrow \alpha$ Sn transformation was also noted on the narrow side surface in the compressive region of the uniformly bent specimen with 7.7% outer fiber pre-strain. Stereo-optical images showing the location of α -Sn on the transformed specimens are presented in Figure B1. Wart-like α -Sn can be observed on the non-uniformly bent specimen as shown in Figure B1 (a), and two transformed regions on the uniformly bent specimen are indicated as regions 1 and 2 in Figure B1 (b). Unlike the specimen with 7.7% outer fiber pre-strain, other uniformly bent specimens with outer fiber pre-strains of 4.6%, 5.8% and 11.5% and 23.0% did not exhibit any transformation even after 6.5 months of aging at -15°C . Similarly, in the non-uniformly bent specimen, tin pest was observed only in the region with an outer fiber tensile strain around 6%. X-ray diffraction (XRD) was performed using pieces detached from the transformed region on the non-uniformly bent specimen. A plot of diffraction intensity versus

diffraction angle was presented in Figure B2, which confirms the presence of α -Sn.

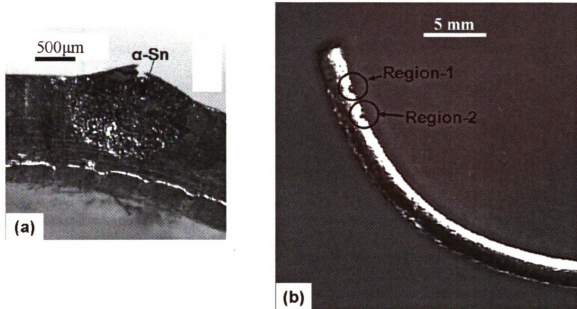


Figure B1 Stereo-optical images showing the location of α -Sn on the (a) tensile side of the non-uniformly bent specimen with 6% outer fiber strain, (b) compressive side of the uniformly bent specimen with 7.7% outer fiber strain (shown as Region-1 and Region-2).

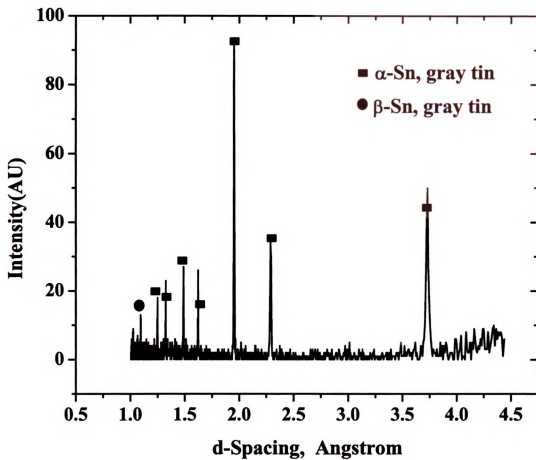


Figure B2 XRD of the α -Sn detached from the non-uniformly bent specimen.

Diffraction peaks associated with β -Sn were also observed in this Figure, which was expected since some β -Sn that was attached to α -Sn particles used for the XRD observation. Due to the slow rate of transformation in the compressive region of uniformly bent specimen, it was not possible to obtain enough α -Sn particles for XRD analysis.

These observations clearly indicate that the state (tensile or compressive) of strain has no effect on the ability of β -Sn to undergo the transformation to α -Sn, since we observed formation of α -Sn on the tensile and compressive regions of the non-uniformly and uniformly bent specimens, respectively. Furthermore, there appears to be a critical range of outer fiber strains which will facilitates the transformation, since α -Sn forms in regions which have relatively close values of outer fiber strain, i.e. 6% and 7.7%. These observations suggest that there exist a critical strain energy of deformation needed to provide the necessary driving force for the transformation and such energy is independent of the state of strain. Moreover, since initiation of tin pest was observed only on the narrow side of the bent specimens, this suggests that a strain gradient may be important for the $\beta \rightarrow \alpha$ Sn transformation. The necessity of strain gradient for the nucleation of α -Sn is further substantiated by lack of tin pest formation in uniaxially deformed specimens after 11 months of storage at -15°C employed in a parallel study, and lack of nucleation of α -Sn on the broad side of the bent specimens which have relatively uniform strains. The observed α -Sn on broad surfaces of bent specimens resulted only by its growth from the nucleation site present on the narrow side at locations close to the broad surface.

B3.2 Microstructural and mechanical characterization

Microstructural evolution of α -Sn regions on the non-uniformly bent and uniformly bent specimens are presented in Figures B3 and B4 respectively. After 2.1 months of aging, cracks within the α -Sn region were observed to be parallel to the edge of the non-uniformly bent specimen (Figure B3 (a)). However, after additional 15 days of aging cracks in same region appeared to spread out radially (Figure B3 (b)). Such an observation indicates that as α -Sn region grows and newer cracks are formed while the existing ones becomes larger. Comparison between Figures B3 (b), B4 (b), and B4 (d) show extensive crack formation, after additional 15 days of aging, on the region experiencing tensile pre-strains in non-uniformly bent specimen, while fewer cracks are visible in regions under compressive pre-strains in the uniformly bent specimen. Furthermore, cracks present with in α -Sn are both inter-granular and trans-granular in nature (Figures B5). As transformation progresses these cracks combine to form larger cracks (shown in Figures B3 (b) and B4 (b)) and lead to the spalling of α -Sn (Figure B3 (b)).

Growth of α -Sn also affects the adjoining β -Sn region due to the increase in volume that needs to be accommodated. Micrographs showing surface relief features within the β -Sn region adjacent to α -Sn region are provided in Figures B6 (a) and B6 (b). These observations suggest that compressive stresses generated during the transformation result in surface relief features within the β -Sn region.

Influence of volumetric expansion warranted by the transformation on the β -Sn region was further investigated by conducting Vickers indentation tests on the broadside of the non-uniformly deformed specimen.

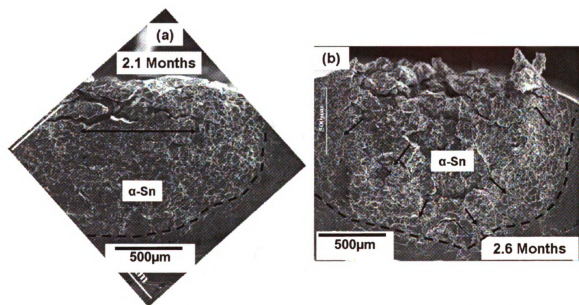


Figure B3 SEM images showing the microstructural evolution of α -Sn on the non-uniformly bent specimen aged at -15°C (a) as observed after 2.1 months, (b) after 2.6 months. Scale bar indicates $500\mu\text{m}$.

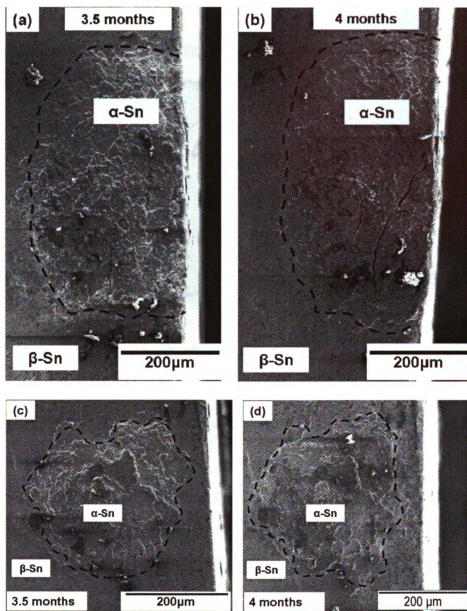


Figure B4 SEM images showing the microstructural evolution of α -Sn on the uniformly bent specimen aged at -15°C (a) after 3.5 months in Region-1 (b) after 4 months in Region-1, (c) after 3.5 months in Region-2 (d) after 4 months in Region-2.

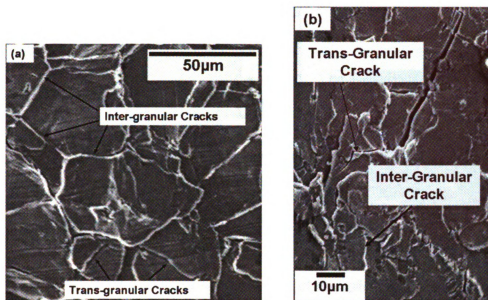


Figure B5 SEM micrographs showing the inter-granular and trans-granular cracks within α -Sn region on (a) non-uniformly bent, and (b) uniformly bent specimens.

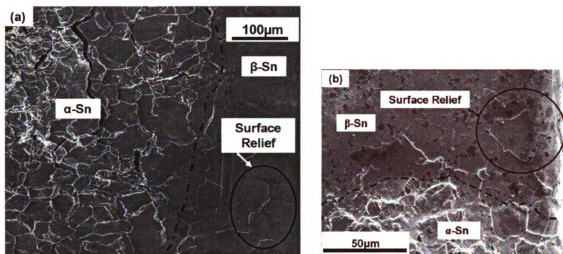


Figure B6 SEM micrographs showing surface relief features with in β -Sn region adjacent to α -Sn (a) non-uniformly bent, and (b) uniformly bent specimens.

Schematic presented in Figure B7 (a) shows the location on the specimen where the indents were made. Figure B7 (b) presents the SEM micrograph of locations of individual indents within the β -Sn region near the β/α interface. Indent sizes became smaller at locations closer to the α/β interface, indicating that β -Sn is harder near the α/β interface. The measured values of hardness are presented in Table B1. The apparent increase in hardness in the adjoining β -Sn region is due to the compressive stresses exerted by the advancing α/β Sn phase boundary.

Table B1 Hardness values of β -Sn at different locations and distances from the β/α Sn interface

Location of the Indent	Distance of each indent from the β/α interface (μm)	Vickers hardness (VPH)
A	100	46
B	400	515

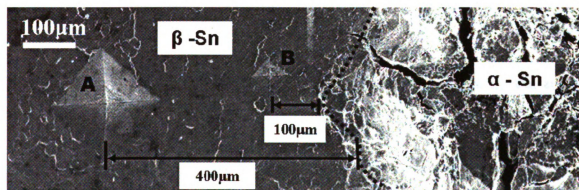
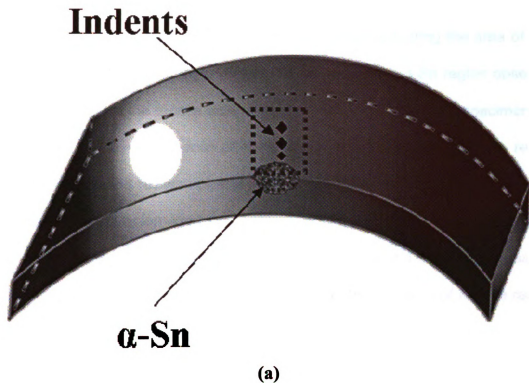


Figure B7 (a) Schematic showing the location of the indents on the broad side of the non-uniformly bent specimen (b) SEM image showing the location and size of the indents. A load of 1 Kg was applied to the broad side of the specimen for 10 seconds.

B3.3 Effect of stress on the growth kinetics of α -Sn

Growth kinetics of the transformation was studied by measuring the area of a α -Sn region as a function of days. Figure B8 (a) shows the α -Sn region observed after 5.1 months on the tensile side of the non-uniformly deformed specimen. In Figure B8 (b), the square root of the measured surface area for the region showed in Figure B8 (a) was plotted versus time. Measurements were stopped after the chosen region impinged with a neighboring α -Sn region. Similar measurements were also made on a α -Sn region in region-1 on the compressive side of the uniformly bent specimen. Plot showing the variation of square root of the surface area of region-1 with number of days is shown in Figure B9. Linear least square fitting on the data shown in Figure B8 (b) and Figure B9 were employ using the form of:

$$A^{1/2} = at + b \quad (1)$$

Where, A is the measured area in mm^2 , t is time in days, where a , and b are fitting constants with units mm/day and mm , respectively.

Similar relationship, as presented in equation (1), has been previously reported by Rogers et.al [88]. The values of constants a and b appearing in equation (1), and calculated average areal growth rates, obtained from the present study are listed in Table BII. Evidently in the presence of tensile pre-strain, the areal growth rate of α -Sn region is two orders of magnitude faster as compared to that noted in regions with compressive pre-strain. This observation suggests that kinetics of the $\beta \rightarrow \alpha$ Sn transformation is influenced by the state of strain.

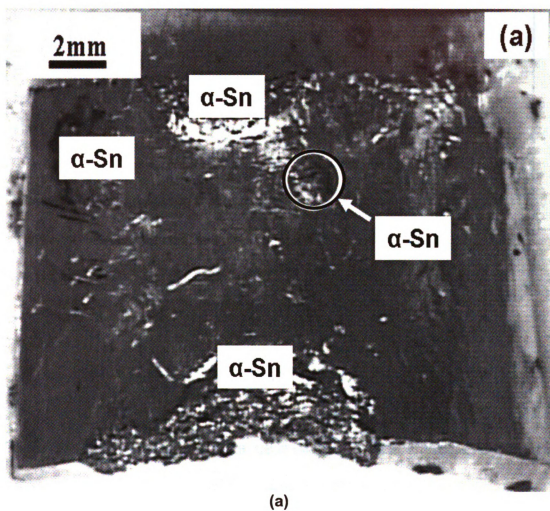
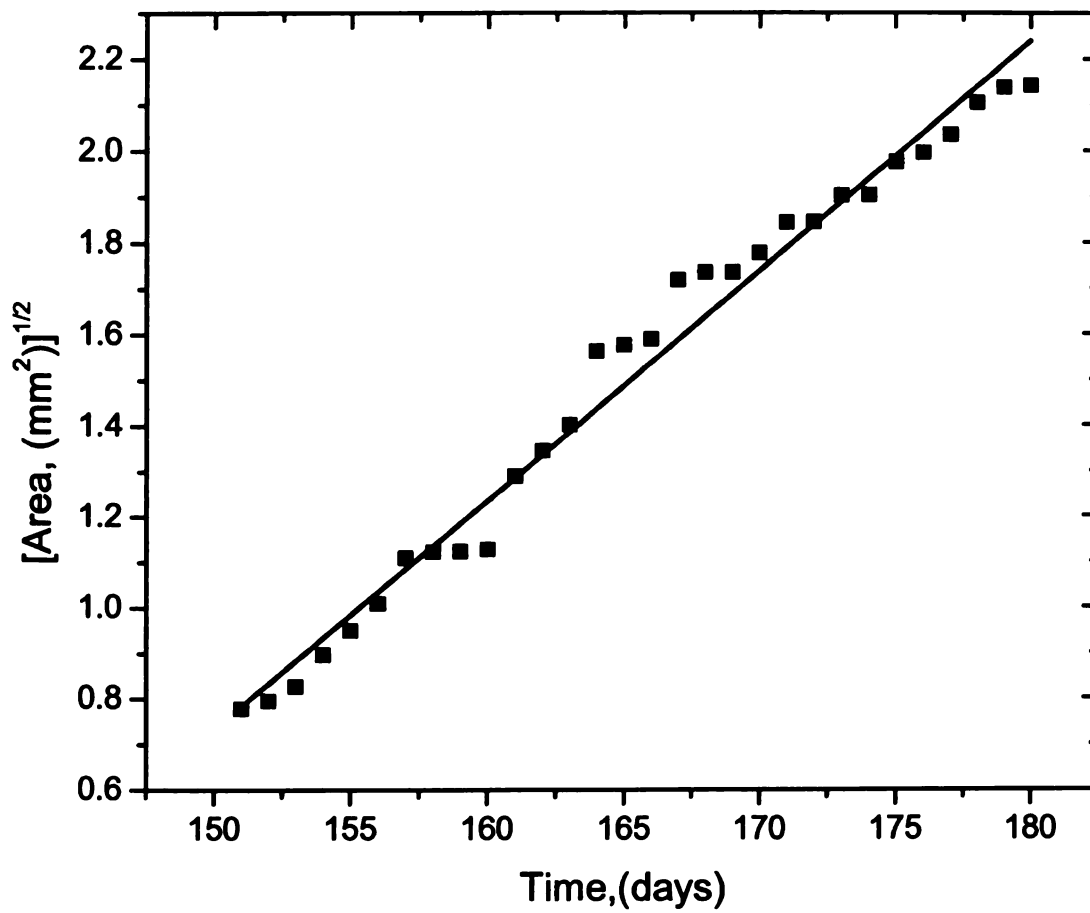


Figure B8 (a) Stereo-optical image showing the location of the α -Sn wart (inside the white circle) on the tensile side of the non-uniformly bent specimen used for measuring growth kinetics



(b)

Figure B8 (b) plot showing the change in measured area of the same α -Sn wart with number of days.

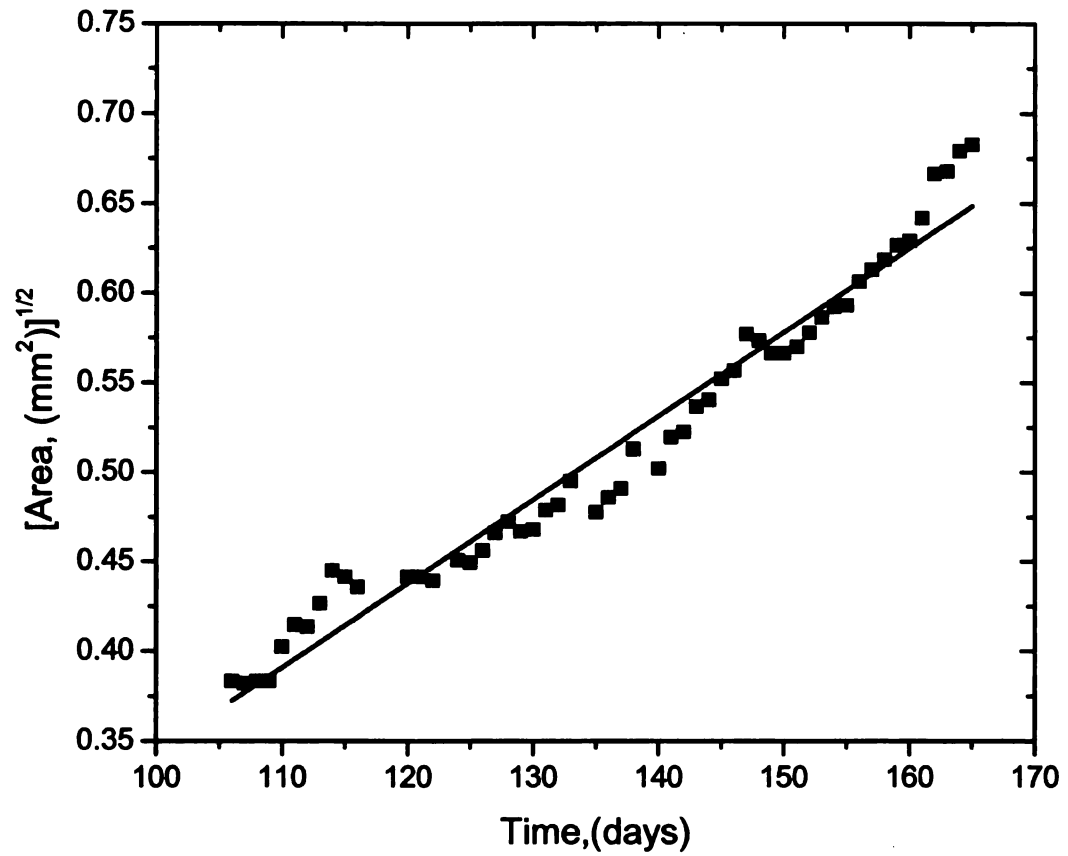


Figure B9 Plot showing the change in the measured area of Region-1 as a function of days. Region-1 was located on the compressive side of the uniformly bent specimen.

Table BII Values showing the growth rate for a given strain state of the specimens and the corresponding correlation coefficients for linear least square fits

State of imposed strain	Average aerial growth rate (mm² / day)	a (mm/day)	b (mm)	R²	Figures
Region with tensile pre-strain	0.143	0.0502	-6.024	0.982	C8(b)
Region with compressive pre-strain	0.005	0.0047	- 0.1241	0.963	C9

During the transformation α -Sn region relieves the stresses generated due to 27% volume increase by forming cracks. While tensile stresses facilitate this process of crack formation, compressive stress retards it. Figures B3 (b) and B4 (b) show such an effect of tensile and compressive stresses on crack formation. As a result, α -Sn region is able to grow quickly under the influence of tensile stresses by effectively relieving the transformational stresses through crack formation. Such a rationale suggests that Sn-based solder joints which are under the influence of compressive stresses will have higher reliability even if α -Sn formation has already taken place.

B4. Summary

Allotropic transformation of β -Sn to α -Sn in mechanically deformed specimens stored at a constant sub-zero temperature was studied. In these studies using pre-strained specimens incubation time was still needed to initiate the transformation, although, it is not yet clear how the length of incubation time is related to the mode and the magnitude of mechanical deformations. However, based on the current study some significant inferences can be made:

1. Presence of a strain gradient may enhance nucleation of tin pest.
2. A critical strain range, irrespective of being tensile or compressive, appears to facilitate $\beta \rightarrow \alpha$ Sn transformation. Such an observation suggests that critical strain energy may aid the transformation.
3. Growth rate of α -Sn is much faster in regions with tensile strain as compared to that in regions with compressive strain.

References

- [1] J. G. Lee, PhD Thesis (2005).
- [2] F. Guo, *Journal of Materials Science-Materials in Electronics* 18 (2007) 129-145.
- [3] F. Guo, J. Lee, K. N. Subramanian, *Soldering & Surface Mount Technology* 15 (2003) 39-42.
- [4] J. Sigelko, S. Choi, K. N. Subramanian, J. P. Lucas, T. R. Bieler, *Journal of Electronic Materials* 28 (1999) 1184-1188.
- [5] M. McCormack, S. Jin, G. W. Kammlott, H. S. Chen, *Applied Physics Letters* 63 (1993) 15-17.
- [6] H. Rhee, K. N. Subramanian, A. Lee, J. G. Lee, *Soldering & Surface Mount Technology* 15 (2003) 21-26.
- [7] C. Kanchanomai, Y. Miyashita, Y. Mutoh, *Journal of Electronic Materials* 31 (2002) 456-465.
- [8] I. E. Anderson, *Journal of Materials Science-Materials in Electronics* 18 (2007) 55-76.
- [9] Y. Kariya, M. Otsuka, *Journal of Electronic Materials* 27 (1998) 866-870.
- [10] Y. Kariya, M. Otsuka, *Journal of Electronic Materials* 27 (1998) 1229-1235.
- [11] I. E. Anderson, B. A. Cook, J. Haringa, R. L. Terpstra, J. C. Foley, O. Unal, *Materials Transactions* 43 (2002) 1827-1832.
- [12] I. E. Anderson, J. C. Foley, B. A. Cook, J. Haringa, R. L. Terpstra, O. Unal, *Journal of Electronic Materials* 30 (2001) 1050-1059.
- [13] I. E. Anderson, J. Walleiser, J. L. Haringa, *Journal of Minerals Metals and Materials* 59 (2007) 38-43.
- [14] D. W. Henderson, J. J. Woods, T. A. Gosselin, J. Bartelo, D. E. King, T. M. Korhonen, M. A. Korhonen, L. P. Lehman, S. K. Kang, P. Lauro, D. Y. Shih, C. Goldsmith, K. J. Puttlitz, *Journal of Materials Research* 19 (2004) 1608-1612.
- [15] C. M. Miller, I. E. Anderson, J. F. Smith, *Journal of Electronic Materials* 23 (1994) 595-601.
- [16] N. Barry, I. P. Jones, T. Hirst, I. M. Fox, J. Robins, *Soldering & Surface Mount Technology* 19 (2007) 29-38.

- [17] J. K. Shang, Q. L. Zeng, L. Zhang, Q. S. Zhu, *Journal of Materials Science-Materials In Electronics* 18 (2007) 211-227.
- [18] K. N. Subramanian, *Journal of Materials Science-Materials in Electronics* 18 (2007) 237-246.
- [19] S. Choi, J. G. Lee, K. N. Subramanian, J. P. Lucas, T. R. Bieler, *Journal of Electronic Materials* 31 (2002) 292-297.
- [20] J. G. Lee, F. Guo, S. Choi, K. N. Subramanian, T. R. Bieler, J. P. Lucas, *Journal of Electronic Materials* 31 (2002) 946-952.
- [21] J. G. Lee, K. N. Subramanian, *Journal of Electronic Materials* 32 (2003) 523-530.
- [22] K. N. Subramanian, *Journal of Electronic Materials* 34 (2005) 1313-1317.
- [23] K. N. Subramanian, *Fatigue & Fracture of Engineering Materials & Structures* 30 (2007) 420-431.
- [24] K. N. Subramanian, J. G. Lee, *Materials Science And Engineering A-Structural Materials Properties Microstructure & Processing* 421 (2006) 46-56.
- [25] J. G. Lee, L. Telang, K. N. Subramanian, T. R. Bieler, *Journal of Electronic Materials* 31 (2002) 1152-1159.
- [26] K. N. Subramanian, J. G. Lee, *Journal of Materials Science-Materials In Electronics* 15 (2004) 235-240.
- [27] T. Chen, I. Dutta, *Journal of Electronic Materials* 37 (2008) 347-354.
- [28] S. G. Jadhav, T. R. Bieler, K. N. Subramanian, J. P. Lucas, *Journal of Electronic Materials* 30 (2001) 1197-1205.
- [29] H. Rhee, K. N. Subramanian, *Soldering & Surface Mount Technology* 18 (2006) 19-28.
- [30] H. Rhee, K. Subramanian, A. Lee, *Journal of Materials Science-Materials in Electronics* 16 (2005) 169-176.
- [31] D. Swenson, *Journal of Materials Science-Materials in Electronics* 18 (2007) 39-54.
- [32] J. G. Lee, K. N. Subramanian, *Soldering & Surface Mount Technology* 17 (2005) 33-39.
- [33] M. Kerr, N. Chawla, *Acta Materialia* 52 (2004) 4527-4535.

- [34] C. Andersson, P. E. Tegehall, D. R. Andersson, G. Wetter, J. Liu, IEEE Transactions on Components & Packaging Technologies 31 (2008) 331-344.
- [35] I. Dutta, D. Pan, R. A. Marks, S. G. Jadhav, Materials Science and Engineering A-Structural Materials Properties Microstructure and Processing 410 (2005) 48-52.
- [36] A. R. Fix, W. Nuchter, J. Wilde, Soldering & Surface Mount Technology 20 (2008) 13-21.
- [37] B. F. Dyson, Journal of Applied Physics 37 (1966) 2375-&.
- [38] B. F. Dyson, T. R. Anthony, D. Turnbull, Journal of Applied Physics 38 (1967) 3408-&.
- [39] G. Deiter, Mechanical Metallurgy, 2ed, Prentice Hall (1998).
- [40] W. J. Plumbridge, Journal of Materials Science-Materials in Electronics 18 (2007) 307-318.
- [41] W. J. Plumbridge, Soldering & Surface Mount Technology 16 (2004) 13-20.
- [42] J. G. Lee, K. N. Subramanian, Microelectronics Reliability 47 (2007) 118-131.
- [43] J. McDougall, S. Choi, T. R. Bieler, K. N. Subramanian, J. P. Lucas, Materials Science and Engineering A-Structural Materials Properties Microstructure and Processing 285 (2000) 25-34.
- [44] D. S. Liu, C. Y. Kuo, C. L. Hsu, G. S. Shen, Y. R. Chen, K. C. Lo, Materials Science and Engineering A-Structural Materials Properties Microstructure and Processing 494 (2008) 196-202.
- [45] Y. T. Chin, P. K. Lam, H. K. Yow, T. Y. Tou, Microelectronics Reliability 48 (2008) 1079-1086.
- [46] N. Zhang, Y. W. Shi, Z. D. Xia, Y. P. Lei, F. Guo, X. Y. Li, Journal of Electronic Materials 37 (2008) 1631-1639.
- [47] D. Y. R. Chong, F. X. Che, J. H. L. Pang, K. Ng, J. Y. N. Tan, P. T. H. Low, Microelectronics Reliability 46 (2006) 1160-1171.
- [48] I. E. Anderson, B. A. Cook, J. Harringa, R. L. Terpstra, Journal of Electronic Materials 31 (2002) 1166-1174.
- [49] K. Jonnalagadda, F. J. Qi, J. Liu, IEEE Transactions on Components and Packaging Technologies 28 (2005) 430-434.

- [50] K. S. Kim, S. H. Huh, K. Sugauma, *Materials Science and Engineering A-Structural Materials Properties Microstructure and Processing* 333 (2002) 106-114.
- [51] J. C. Suhling, H. S. Gale, R. W. Johnson, M. N. Islam, T. Shete, P. Lall, M. J. Bozack, J. L. Evans, P. Seto, T. Gupta, J. R. Thompson, *Soldering & Surface Mount Technology* 16 (2004) 77-87.
- [52] S. Choi, T. R. Bieler, J. P. Lucas, K. N. Subramanian, *Journal of Electronic Materials* 28 (1999) 1209-1215.
- [53] C. M. L. Wu, Y. W. Wong, *Journal of Materials Science-Materials in Electronics* 18 (2007) 77-91.
- [54] M. Pei, J. M. Qu, *Journal of Electronic Materials* 37 (2008) 331-338.
- [55] A. Lee, K. N. Subramanian, *Journal of Electronic Materials* 34 (2005) 1399-1407.
- [56] S. H. Phillips, T. S. Haddad, S. J. Tomczak, *Current Opinion in Solid State & Materials Science* 8 (2004) 21-29.
- [57] R. M. Laine, *Journal of Materials Chemistry* 15 (2005) 3725-3744.
- [58] R. Murugavel, A. Voigt, M. G. Walawalkar, H. W. Roesky, *Chemical Reviews* 96 (1996) 2205-2236.
- [59] J. K. Kim, K. H. Yoon, D. S. Bang, Y. B. Park, H. U. Kim, Y. H. Bang, *Journal of Applied Polymer Science* 107 (2008) 272-279.
- [60] L. Song, Q. L. He, Y. Hu, H. Chen, L. Liu, *Polymer Degradation and Stability* 93 (2008) 627-639.
- [61] L. e. D.R., (2003).
- [62] X. W. Liu, W. J. Plumbridge, *Journal of Electronic Materials* 36 (2007) 1111-1120.
- [63] S. Chada, R. A. Fournelle, W. Laub, D. Shangguan, *Journal of Electronic Materials* 29 (2000) 1214-1221.
- [64] K. W. Moon, W. J. Boettinger, U. R. Kattner, F. S. Biancaniello, C. A. Handwerker, *Journal of Electronic Materials* 29 (2000) 1122-1136.
- [65] M. Rappaz, P. Thevoz, *Acta Metallurgica* 35 (1987) 1487-1497.
- [66] R. A. Robert E Reed-Hill, *Physical Metallurgy*, Prentice Hall (1991).
- [67] B. H. K. Kingery W.D., Uhlmann D.R., *Introduction to Ceramics* (1976).

- [68] R. Trivedi, W. Kurz, *International Materials Reviews* 39 (1994) 49-74.
- [69] R. Trivedi, W. Kurz, *Acta Metallurgica Et Materialia* 42 (1994) 15-23.
- [70] P. W. Voorhees, *Annual Review of Materials Science* 22 (1992) 197-215.
- [71] S. E. Babcock, R. W. Balluffi, *Acta Metallurgica* 37 (1989) 2357-2365.
- [72] S. E. Babcock, R. W. Balluffi, *Acta Metallurgica* 37 (1989) 2367-2376.
- [73] T. E. Hsieh, R. W. Balluffi, *Acta Metallurgica* 37 (1989) 1637-1644.
- [74] H. E. Kissinger, *Journal of Research of the National Bureau of Standards* 57 (1956) 217-221.
- [75] S. L. Allen, M. R. Notis, R. R. Chromik, R. P. Vinci, *Journal of Materials Research* 19 (2004) 1417-1424.
- [76] I. M. Lifshitz, V. V. Slyozov, *Journal of Physics and Chemistry of Solids* 19 (1961) 35-50.
- [77] A. J. Ardell, *Acta Metallurgica* 20 (1972) 601-&.
- [78] O. N. Senkov, M. M. Myshlyayev, *Acta Metallurgica* 34 (1986) 97-106.
- [79] A. R. Fix, G. A. Lopez, I. Brauer, W. Nuchter, E. J. Mittemeijer, *Journal of Electronic Materials* 34 (2005) 137-142.
- [80] P. G. Shewmon, *Diffusion in Solids*, McGraw Hill (1989).
- [81] A.W. Gibson, K.N. Subramanian, T.R Beiler, *Design Reliability of Solder and Solder Interconnections*, TMS Annual meeting, vol 1997, p.^pp.
- [82] J. Sommer, C. Herzig, *Journal of Applied Physics* 72 (1992) 2758-2766.
- [83] Y. Q. Zhao, D. A. Schiraldi, *Polymer* 46 (2005) 11640-11647.
- [84] Y. Kariya, N. Williams, C. Gagg, W. Plumbridge, *JOM-Journal of The Minerals Metals & Materials Society* 53 (2001) 39-41.
- [85] Y. Kariya, C. Gagg, W. J. Plumbridge, *Soldering & Surface Mount Technology* 13 (2001) 39-40.
- [86] J. Cugnoni, J. Botsis, V. Sivasubramaniam, J. Janczak-Rusch, *Fatigue & Fracture of Engineering Materials & Structures* 30 (2007) 387-399.
- [87] L. H. Xu, J. H. L. Pang, K. N. Tu, *Applied Physics Letters* 89 (2006).

[88] R. R. Rogers, J. F. Fydell, *Journal of The Electrochemical Society* 100 (1953) 383-387.

[89] Y. J. Joo, T. Takemoto, *Materials Letters* 56 (2002) 793-796.

[90] R. C. Farrow, M. T. Asom, K. A. Jackson, L. C. Kimerling, *Institute of Physics Conference Series* (1989) 259-264.

MICHIGAN STATE UNIVERSITY LIBRARIES



3 1293 03063 2552